Cryogenic Pellet Ablation Modelling in a Hot, Magnetised Plasma

Frederick Kyle Martin MSci

Submitted in fulfilment of the requirements for the
Degree of Doctor of Philosophy

School of Engineering
College of Science and Engineering
University of Glasgow

April 2021

Abstract

This thesis explores the possibility of using a simple "toy" model approach to characterising the ablation rate of a pellet once injected into a magnetised plasma. A model for the ablation rate and structure of the cloud in terms of its size and density is produced by assuming the ablation process is in kind to that of the evaporation of sessile pellets. An empirical law known as the "D^2" law is revised and applied to determine these key quantities which are then used in a Bethe-type calculation assuming continuous slowing down of electrons within the neutral cloud. Any stopped charge then contributes to an electric potential field which further slows particles as they enter the cloud and a feedback system is established. Additionally, a floating sheath is generated whose potential field further mitigates the electron energy as they traverse the cloud and the creation of ions by ionisation within the cloud are permitted to diffuse and ions sufficiently close will be accelerated by the sheath field and allowed to impact the pellet. The energy arriving at the surface of the pellet releases neutral particles which then change the structure of the cloud and the system evolves self-consistently. The ablation rate and projected lifetime of the pellet in each of these scenarios are measured against experimental results to assess the efficacy of the model. Finally, the Hα emission is modelled and compared to emission profiles from experiment.

The modified evaporative model applied in this thesis agrees moderately well with existing measurements from tokamak devices. Order of magnitude agreement is found but more thorough agreement is hard to achieve given the temporal variation of the system the model predicts and the struggle to determine what point in the pellet's lifetime an experimental measurement was taken. A similar conclusion on the results is found for the neutral density of the cloud. The influence that these results have over the self-consistent field models is evidenced in ablation rate results for the four models developed in the thesis. The Fully Neutral model is the only model that predicts the ablation rate to even order of magnitude with the potential fields generated inhibiting any significant ablation. The neglect of charge deposition and the self-field is fundamentally incorrect and more complex models that boost the ablation with additional mechanisms or mitigate charge density in the cloud are needed in further bodies of work.

Contents

List of Tables

List of Figures

Acknowledgements

The journey this thesis has taken me has introduced me to so many people that I could not possibly thank them all. Between supervisors and mentors, colleagues and friends, and the various acquantainces I've met through summer schools and conferences there are simply too many to thank every one of you. That is not to say that I will not name at least a few people who I feel have had more influential roles.

Without question, I could not have made it past the first day without Declan Diver. All those years ago, back in A1 lectures I didn't think that Declan would ever play such a formative role in my education and I could not be happier that he has. Between his support, his humour, his kindness, his patience, his experience, his mastery of the craft and everything that makes him Declan, I could not have achieved this without any one of them. Thank you Declan.

I also need to thank Lyndsay Fletcher for all the help particularly during the end-of-year progression review. While mostly seen as a box-ticking exercise you made it all the more interesting by offering insights and prompting intelligent discussion which helped in the coming year of research. In saying that, the untold hours of conversation during coffee breaks were far more interesting and I only wish I could have enjoyed more of them! Thank you Lyndsay.

As far as go-to post-docs go, Alasdair really is up there with the best of them. I'm pretty sure there isn't a single topic in the Universe ("on the planet" is far too restrictive) that Alasdair can't offer some kind of commentary on. Any time I needed some support on a problem and I didn't feel like confessing my ineptitude to Declan, Alasdair was always there to walk me through it no matter how trivial it seemed. Having been locked in the house for what is over a year now I really do miss the evenings in the pub and God knows you're owed a pint. Thank you Al.

I'm also not sure I would have lasted as long as I had were it not for Meg. Your support and meaningful conversation over the years has been a pillar of strength when it was needed most. I'm also more than glad most of those conversations had almost nothing to do with plasmas and plenty to do with careers and life in general. Thank you Meg.

Then there's 604 with its cast of inimitable characters. To all of you, thank you. For either putting up with me, supporting me, outright helping or just suffering my seemingly endless

complaints about things that didn't deserve the emotional energy I expended on not liking them. For that I can only apologise to Graham, Duncan, Pete, Stephen, Andrew, Nicolina, John, Chris, Kris, David, Paul, Dina, Aaron, Tony and Ben. Thank you to all of you. I will keep in touch.

I, of course, must thank my parents without whom I could never have hoped to have made it to day 0 of the PhD. Thank you for the love, the patience, the effort, the money, the understanding and the seemingly eternal hours on the phone listening to fairly bland conversation. I don't say it nearly enough, but thank you.

In no particular order is everyone else whose name springs to mind at the time of writing; Nic, Norman, Hugh. Hamish, Alec, Rachel, Eduard, Natasha, Paulo, Iain, Jim (pints most definitely needed), Aileen & Moira, Felicity & Elbie, the Bright Club crew, the entire A1 labs team, and anyone else who has supported me on the way. Thank you.

Finally, I'd like to thank COVID-19 for locking me in my room for 6 months and forcing me to write a thesis.

Declaration

With the exception of chapters 1, 2 and 3, which contain introductory material, all work in this thesis was carried out by the author unless otherwise explicitly stated.

"Here, it must needs be said, that accidents like this have in more than one case occurred to ships in violent storms. The magnetic energy as developed in the mariner's needle, is, as all know, essentially one with electricity beheld in heaven; hence it is not to be much marvelled at, that such things should be."

CAPTAIN AHAB, MOBY DICK

Chapter 1

Introduction

A plasma is a gas that contains a significant fraction of positive and negative free charges such that electromagnetic forces dominate the dynamics. The charges interact with and respond to the ambient electromagnetic fields which is comprised of any imposed field and the self-field of the constitutent charges. This collective response to an electromagnetic disturbance is a fundamental difference between a plasma and a gas which has granted plasmas the classification of the fourth state of matter. This fourth state of matter requires a change of state to occur (typically from a gas to a plasma) known as ionisation. This is, generally speaking, achieved by injecting kinetic or thermal energy into a body of neutral gas which creates a substantial fraction of particles with kinetic energy exceeding the potential energy of the bound electrons in their atomic state. Collisions between the constituent gas particles transfer energy to the electrons which dissociate from their parent ion and freely move as individual particles. Alternatively, radiative energy in the form of ultra-violet photons in particular typically has enough energy to ionise an atom. In this case, the photon itself must have an energy greater than the ionisation energy of the atom which is around 16eV for hydrogen and ultra-violet photons largely meet this criterion. Once a considerable portion of this neutral gas has been ionised and its dynamics demand an electromagnetic description, it can be described as a plasma.

Plasmas constitute the overwhelming majority of the Universe in the form of stellar bodies, the intergalactic medium and portions of planetary atmospheres. Admittedly, these are fairly detached from most people's daily work but plasmas are becoming more common in daily life with markets such as flameless lighters and domestic lighting incorporating plasmas into their products. The field of plasma physics has grown beyond purely academic and astronomical studies and have contributed to commercial and practical terrestrial problems not least of all is the mission to achieve controlled and sustained thermonuclear fusion as a viable energy source, a subject which is closely tied to the content of this thesis. Each of these plasmas possess their own parameters which determine their set of time and

length scales that uniquely identify a plasma for study. A series of these characteristic quantities are discussed followed by the appropriate regime to study them based on the connection between these scale lengths in this chapter.

1.1 Common Lengthscales and Timescales

A common means of assessing the relevance of a plasma description of a medium is to consider the sum of the number density of electrons and ions, $n_e + n_i$, in the medium compared to the total number density, n_T, which is the combined number density of atoms and ions. Typical ionisation fractions, f, can sit from 10^{-5} for partially ionised plasmas to 1 for fully ionised hydrogen plasmas as found in the bulk plasma in tokamaks or the solar corona,

$$f = \frac{n_e + n_i}{n_T}. \tag{1.1}$$

This is an acceptable metric for determining the measure of ionisation but can describe a plasma as little more than "partially" or "fully" ionised. To learn more about the relevance of certain plasma effects with respect to others it becomes necessary to explore the characteristic lengths and times associated with those processes.

1.1.1 Lengths

The most fundamental of all the lengthscales associated with plasmas is the *Debye length* and is sometimes referred to as the *screening length* which is identified with the ability for a plasma to minimise the impact of its own potential on itself. This distance corresponds to the scale length over which the charge from a particle in a plasma is diminished by a factor of e. This notion is developed in full in texts such as Gurnett and Bhattacharjee (2005) and Boyd and Sanderson (2003) but is also explored here.
Supposing that in a fully ionised hydrogen plasma, the distribution of ions and electrons in the plasma is represented by Boltzmann statistics and therefore for a temperature, T, and potential field, ϕ, the species density, n_s, can generally be given by equation 1.2,

$$n_s = n_0 \mathrm{e}^{-\frac{q\phi}{k_B T}}, \tag{1.2}$$

for a uniform background density n_0, the charge of the species, q, and the Boltzmann constant, k_B. Assuming that the potential is much smaller than the temperature, the density can be expanded and the individual charge of the species taken into account to yield equations 1.3 and 1.4:

$$n_i \approx n_0\Big(1-\frac{e\phi}{k_BT}\Big), \tag{1.3}$$

$$n_e \approx n_0\Big(1+\frac{e\phi}{k_BT}\Big). \tag{1.4}$$

The charge density within the plasma can then be defined:

$$\begin{aligned}\rho_c &= e\Big(n_i - n_e\Big)\\ &= en_0\left(\left(1-\frac{e\phi}{k_BT}\right)-\left(1+\frac{e\phi}{k_BT}\right)\right) &(1.5)\\ &= -\frac{2n_0e^2\phi}{k_BT}. &(1.6)\end{aligned}$$

This result can now be used in Poisson's equation to find an expression for the potential in the plasma. This method highlights the meaning behind the Debye length and removes any confusion regarding the term "screening length" because it features in the solution to the subsequent differential equation,

$$\begin{aligned}\nabla^2\cdot\phi &= -\frac{\rho_c}{\epsilon_0},\\ &= \frac{2e^2n_0}{\epsilon_0k_BT}\phi. &(1.7)\end{aligned}$$

Looking at the right hand side it's clear that the fraction term has the dimension of L^{-2}. This term then gets adopted into the definition of Debye length with the omission of the factor 2:

$$\lambda_D = \left(\frac{\epsilon_0k_BT}{n_0e^2}\right)^{\frac{1}{2}}. \tag{1.8}$$

A general solution to equation 1.7 will present an exponential solution with the Debye length as its scaling term within the argument. This accounts for behaviour far from the charge but inside a Debye radius it is essential to maintain the Coulomb Law which is found in the formal solution to equation 1.7. This solution will not be expanded upon any

further but is presented here in equation 1.9 for a total charge Q, a radial distance from the source, r, and an electric potential, ϕ.

$$\phi = \frac{Q}{4\pi\epsilon_0 r} \mathrm{e}^{\frac{-r}{\lambda_D}}. \tag{1.9}$$

So important is this scale length that it is necessary to determine how appropriate the plasma description is for a medium by considering the number of charged particles within a volume, known as the *plasma parameter*. Neglecting geometric factors the plasma parameter, N_λ, is given by

$$N_\lambda = n_s \left(\frac{\epsilon_0 k_B T}{e^2 n_0} \right)^{\frac{3}{2}}. \tag{1.10}$$

If N_λ is much greater than 1 then the criteria for a plasma description is comfortably satisfied, otherwise the medium is not predominantly governed by plasma dynamics and can be considered "neutral".

Another scale length is the *mean free path* for a particle between collisions. It can be considered the average distance a particle traverses before interacting in a binary manner with another particle. However, the distance over which a particle may interact is not limited to its physical area presented to the target but to a cross-section determined through quantum mechanical calculations. Neglecting these quantum details allows for a rather simple expression for a mean free path, λ, for a gas of number density, n, and a total cross-section of interaction, σ. It is important to note that the cross-section is a function of the particle energy and therefore not a constant even if it may justifiably be treated as one for certain calculations,

$$\lambda = \frac{1}{n\sigma(E)}. \tag{1.11}$$

For an interaction of interest the cross-section for exclusively that interaction could be used to calculate a mean free path associated with it. The cross-section itself is energy dependent and will typically be more significant in describing behaviour in the range of a few 10s of electronvolts but values of σ are typically of the order $\sim 10^{-20}\mathrm{m}^2$. Some of these specific interactions will excite short-lived states in atoms/molecules that may go on to interact through mechanisms that have unique electromagnetic signatures, such as spectral lines, or products that go on to react in other unique or interesting ways. The subject of cross-sections and collisions will be expanded upon more in chapter 3.

If the plasma is magnetised then the constituent particles will gyrate perpendicular to the magnetic field direction in a circular orbit. This is because magnetic fields do not formally do work on charged particles (i.e. $\mathbf{v} \cdot \mathbf{v} \times \mathbf{B} = 0$) and therefore the velocity perpendicular to the field will remain constant. Assuming no electric fields are present then the force on the particle in a circular orbit can be expressed as,

$$\begin{aligned} \frac{mv^2}{r_L} &= qvB, \\ r_L &= \frac{mv}{qB}. \end{aligned} \tag{1.12}$$

This is the *Larmor radius* and is a useful metric for deciding on a theoretical approach to a problem where the relevance of magnetic effects must be considered.

1.1.2 Times and Frequencies

A common timescale used to relate the length of interactions is the *plasma frequency*. The plasma frequency, ω_p, is a timescale associated with the natural oscillations that occur in an electrically charged gas. The random thermal fluctuations associated with a distribution of energies causes perturbations to the background density of charges. These deviations generate an excess in Coulomb repulsion between particles which repels the particles farther in the opposite direction and closer to another particle. This establishes a natural oscillation of local charge density in the medium at the plasma frequency.
An expression for the plasma frequency can be derived with this thinking in mind. The perturbations to the uniform background are due to the thermal motions and will occur over a Debye length. The ratio of the thermal velocity to the Debye length will yield the plasma frequency given by,

$$\begin{aligned} \omega_p &= \left(\frac{k_B T_e}{m_e}\right)^{\frac{1}{2}} \frac{1}{\lambda_D}, \\ &= \left(\frac{k_B T_e}{m_e}\right)^{\frac{1}{2}} \left(\frac{\epsilon_0 k_B T_e}{n_0 e^2}\right)^{-\frac{1}{2}}, \\ &= \left(\frac{n_0 e^2}{m_e \epsilon_0}\right)^{\frac{1}{2}}. \end{aligned} \tag{1.13}$$

An expression can be evaluated for electrons or ions by substituting in the appropriate densities and for λ_D.
Magnetic fields and the Lorentz force also have an associated timescale. The gyration of particles about a magnetic field exhibit periodic behaviour and there will be a frequency determined by that period. This is given by the *gyrofrequency* of the particle in equation 1.14,

$$\omega_c = \frac{qB}{m}. \tag{1.14}$$

The final common timescale of interest is the *collision timescale* for ions and electrons, which will realistically differ. As will be shown in the next section, an equilibrated plasma with a well-defined temperature will have a distribution of particle energies within it. If, for example, the root-mean-square velocity is taken, then the time between collisions is the time taken for a particle travelling at v_{RMS} to travel a mean free path λ,

$$\tau_s = \frac{\lambda}{v_{RMS,s}}, \tag{1.15}$$

where the subscript s identifies the species, used here generally. Timescales here will be due to many differences such as temperature, particle energy, species, plasma density and many more. It is therefore difficult to generalise such a timescale but the process remains the same for a particular instance of parameters. Table 1.1 presents some typical scale length values for a few different plasmas to illustrate the range in parameter plasmas can possess and justifiably still be described as a plasma. The method to model these plasmas may require tailoring to each individual case but each approach described in the following section is perfect valid as long as a set of criteria relating to the scale lengths is satisfied.

1.2 Descriptions of a Plasma

To study plasmas, and indeed anything, effectively an appropriate theoretical framework must be constructed and used to describe the behaviour under observation. In the study of any electromagnetic phenomenon the use of Maxwell's equations can yield tremendous insight. They describe the interwoven nature of electric and magnetic fields to each other and the motion (or its absence) of charges. The value of Maxwell's equations to plasma

Table 1.1: Typical length and time scales for plasmas that occupy different parameter regimes. Tokamak data taken from Keilhacker et al. (1999) for JET. Interstellar medium data taken from Lieberman and Lichtenberg (2005) and Livadiotis et al. (2018).

Quantity	**Tokamak**	**Interstellar medium**
r_L/m	10^{-4}	10^{2}
λ_{mfp}/m	10^{-5}	10
λ_D/m	10^{-8}	10^{-2}
ω_p/Hz	10^{11}	10^{5}
τ_{mfp}/s	10^{-12}	10^{-4}
ω_c/Hz	10^{11-12}	10^{4}

physics can not be overstated and will be succinctly described below,

$$\nabla \cdot \mathbf{E} = \frac{\rho_q}{\epsilon_0}, \tag{1.16}$$

$$\nabla \cdot \mathbf{B} = 0, \tag{1.17}$$

$$\nabla \times \mathbf{E} = -\frac{\partial \mathbf{B}}{\partial t}, \tag{1.18}$$

$$\nabla \times \mathbf{B} = \mu_0 \epsilon_0 \frac{\partial \mathbf{E}}{\partial t} + \mu_0 \mathbf{J}. \tag{1.19}$$

In these equations $\mathbf{E}$ is the electric field vector, $\mathbf{B}$ is the magnetic flux density vector, $\mathbf{J}$ is the current density vector, ρ_q is the charge density, t is time co-ordinate, μ_0 is the permeability of free space and ϵ_0 is the permittivity of free space. Equation 1.16 describes how the structure of an electric field depends on the distribution of charge over a region, equation 1.17 states that there are no magnetic monopoles, equation 1.18 states that a time varying magnetic field will induce an electric field and equation 1.19 shows that conduction or displacement currents will generate magnetic fields.

Maxwell's equations and their applications have been well-documented and will be discussed only when necessary. The remainder of this section is devoted to providing a brief description of the common mathematical frameworks used to model plasmas. The single particle description will be discussed first, owing to its simplicity both algebraically and conceptually.

1.2.1 Single Particle Description

The dynamics and kinematics of an individual charged particle within electromagnetic fields is comparatively simple to study when placed next to collective descriptions such as kinetic or fluid models. However, the very definition of a plasma should be in apparent contrast with describing any kind of plasma which displays collective behaviour. Collective behaviour cannot arise when there is only a single particle to examine but when studying low density plasmas, the collective effects may only play a small role in the dynamics and the single particle approach can produce useful results. In terms of the scale lengths defined previously, the plasma parameter must be significantly greater than 1 i.e $N_\Lambda \gg 1$ and also that the influence of the magnetic field is greater than any binary collision between molecules, $\omega_c^{-1} \ll \tau_s$. Alternatively, a measure of the relative importance of the applied fields to the "self-field" of the plasma can be used. If the applied fields are significantly larger than the field of a nearest neighbour then the single particle description is valid. Similarly, if the gyroradius, or Larmor radius, r_L, is much larger than the actual scale of the plasma, L, then the motion of the gyrocentre can be studied instead.
A common starting point for the single particle treatment is to simply consider the equation of motion of a particle and the relevant forces acting on it. This is given by equation 1.20 where $\mathbf{v}$ is the velocity vector of the particle and $\mathbf{F}$ is a general force acting on the particle such as gravity,

$$m\frac{\mathrm{d}\mathbf{v}}{\mathrm{d}t} = q\Big(\mathbf{E} + \mathbf{v}\times\mathbf{B}\Big) + \mathbf{F}. \tag{1.20}$$

For a homogeneous magnetic field in a static equilibrium, the relatively simple helical trajectory around a stationary line known as the *guiding centre* is produced. The study of any motion of the guiding centre then illustrates any deviation of particles from their helical trajectory due to the addition of any electric or magnetic fields or changes to the linear geometry. These drifts can be determined analytically with some approximations in the case of crossed electric and magnetic fields, gradients in the magnetic field or any curvature in the magnetic field. Once the number of particles in a Debye sphere becomes much larger than 1, the self-fields become comparable to any applied fields or the mean free path of particles becomes much smaller than the scale of the plasma then a collective description becomes more appropriate. The effect of collisions and interactions between particles is now a dominating force in the governance of the plasma dynamics which neatly leads to the kinetic description which captures the effect of particles on one another.

1.2.2 Kinetic Description

The limitations of the single particle approach are its own advantages. Whilst it is relatively easy to evaluate the motion of a singular particle in electric and magnetic fields, it is often not a suitable description of the physics. Frequently there are many particles interacting with each other significantly either through varying long-distance electromagnetic forces or short-distance binary collisions. The single particle approach will not be able to capture this detail but the kinetic model can.

One of the shortcomings of the kinetic model is that applying it to real world systems involves the solution of 10^{23} simultaneous equations for a mole of hydrogen gas, ionised or not. This is an impossible task analytically or numerically but a statistical approach can make this problem more tractable by assigning a distribution of energies to the particles with a uniquely qualifying quantity - the temperature. This somewhat complicates the situation further in that it also means that thermal effects must always be accounted for in a kinetic analysis however the power in the distribution function and its ability to return thermodynamic properties (which will be shown later) make this an acceptable trade-off. The most commonly used distribution function is the Maxwell-Boltzmann distribution, given in terms of velocity and energy in equations 1.21 and 1.22 respectively,

$$f_{MB}(v) = 4\pi n_0 \left(\frac{m}{2\pi k_B T}\right)^{\frac{3}{2}} v^2 \exp\left(-\frac{mv^2}{2\pi k_B T}\right), \tag{1.21}$$

$$f_{MB}(E) = n_0 \frac{2}{\sqrt{\pi}} \left(\frac{3}{2\bar{E}}\right)^{\frac{3}{2}} E^{\frac{1}{2}} \exp\left(-\frac{3E}{2\bar{E}}\right). \tag{1.22}$$

Equation 1.22 is represented for several mean energies in figure 1.1. The characteristic shape of the distribution is visible here with the value of the distribution associated with the most common energy decreasing with increasing mean energy. This is because the distribution is normalised to 1 and as the "peak region" covers a greater range of energy values, the peak itself must be smaller. Equations 1.21 and 1.22 are both purely one-dimensional but it is simple to extrapolate to three velocity co-ordinates. Similarly, if a spatial distribution of particles across a room for example is considered, there is a spatial element to their distribution in addition to any velocity (or energy) distribution. Supposing finally that this six-dimensional distribution is subject to change in time then the distribution function, f, that is most commonly associated with kinetic physics is defined. While it is possible to expand upon the properties of the distribution function,

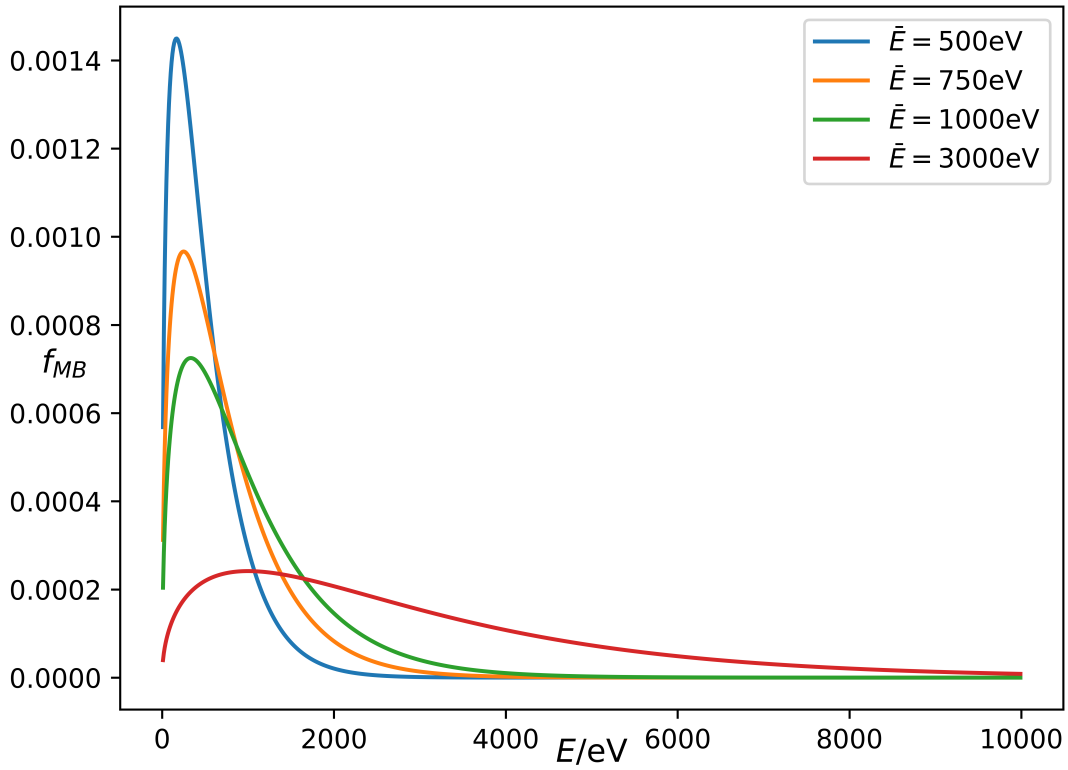

Figure 1.1: A selection of normalised Maxwell-Boltzmann curves (given by equation 1.22) in the range $[10, 10000]$eV.

only a select few will be discussed here. The first is essential to understand what the distribution function means and which derives from its fundamentally statistical nature. The distribution function defines the number of particles contained within a small element of the six dimensional *phase space* defined by the spatial and velocity co-ordinates. So the average number of particles inhabiting a small volume of phase space at a given time is defined as,

$$\mathrm{d}N = f(x, y, z, v_x, v_y, v_z, t))\mathrm{d}x\mathrm{d}y\mathrm{d}z\mathrm{d}v_x\mathrm{d}v_y\mathrm{d}v_z. \tag{1.23}$$

As with any statistical approach, it is possible to determine the large-scale average properties of this function by multiplying by powers of the velocity and integrating over all of velocity space. Some quantities that can be calculated are the density, mean velocity and pressure tensor to name a few. These calculations are not performed explicitly here but are well-

documented in texts such as Gurnett and Bhattacharjee (2005). The results are presented below with m denoting the particle mass.

$$n(\mathbf{r},t) = \int f(\mathbf{r},\mathbf{u},t)\mathrm{d}\mathbf{u} \qquad \textit{number density}, \tag{1.24}$$

$$\bar{\mathbf{u}}(\mathbf{r},t) = \frac{1}{n}\int \mathbf{u} f(\mathbf{r},\mathbf{u},t)\mathrm{d}\mathbf{u} \qquad \textit{fluid velocity}, \tag{1.25}$$

$$\mathbf{P}(\mathbf{r},t) = m\int (\mathbf{u}-\bar{\mathbf{u}})(\mathbf{u}-\bar{\mathbf{u}}) f(\mathbf{r},\mathbf{u},t)\mathrm{d}\mathbf{u} \qquad \textit{pressure tensor}. \tag{1.26}$$

These are macroscopic properties of the plasma that can be recovered from the microscopic description and will be addressed in more depth later. So far the discussion has been limited to a singular time with variation in phase-space co-ordinates but temporal variation in the distribution function due to the action of forces yields a deeper understanding of the physics. A number of governing equations in the kinetic limit exist depending on the forces under consideration but the simplest is the equation 1.27 which considers only the effect of longer range forces and neglects "instantaneous" collisions,

$$\frac{\partial f}{\partial t} + \mathbf{u}\cdot\nabla f + \frac{\mathbf{F}}{m}\cdot\nabla_v f = 0. \tag{1.27}$$

If the general force term $\mathbf{F}$ is substituted for the long-range electromagnetic forces which are commonly associated with plasmas equation 1.28 is defined. This equation describes the change in the distribution function due to long range electromagnetic forces in a collisionless plasma. This is known as the *Vlasov equation*,

$$\frac{\partial f}{\partial t} + \mathbf{u}\cdot\nabla f + \frac{q}{m}\Big(\mathbf{E}+\mathbf{v}\times\mathbf{B}\Big)\cdot\frac{\partial f}{\partial \mathbf{u}} = 0. \tag{1.28}$$

Not all plasmas are collisionless. In cases where the mean free path is much smaller than the scale of the plasma then collisions are frequent and their immediate and drastic change in a particle's phase space co-ordinate should be considered. This is achieved by requiring that the above equations are not in fact equal to zero, but have a value determined by a collisions operator, defined here generally as $\frac{\delta_c f}{\delta t}$. This change is captured in equation 1.29 known as the *Boltzmann equation*,

$$\frac{\partial f}{\partial t} + \mathbf{u}\cdot\nabla f + \frac{\mathbf{F}}{m}\cdot\nabla_v f = \frac{\delta_c f}{\delta t}. \tag{1.29}$$

The detail offered by a kinetic model is only glanced at in this section but achieves the goal of presenting the fundamentals of kinetic theory and the notion of the distribution function. The concept of collisions themselves has not been covered appropriately in this section but will be returned to in chapter 3 where their relevance to the contextual matter of this thesis is more apparent.
As mentioned earlier, the statistical approach comes with a loss of precision on for individual particles but if those microscopic quantities are averaged out over all the particles, the macrosopic properties are returned. The moments of the Boltzmann equation will return the macroscopic conservation laws for fluid mechanics such as mass continuity, momentum conservation and energy conservation to name the first three. The moment equations are the vector equivalent of a number of fundamental conservation laws in physics but extended to the continuous fluid limit with the macroscopic quantities derived from the microscopic quantities associated with kinetic theory. Describing a plasma based on these large-scale quantities is the domain of hydrodynamics and, when electromagnetic effects are considered, magnetohydrodynamics.

1.2.3 Fluid Description

Operating in the fluid limit requires that the distribution of particles have reached a local thermodynamic equilibrium. This can only be achieved if a sufficient number of collisions have occured over the shortest relevant fluid timescale. Another way to qualify the fluid approach is to demand that the physical size of the plasma must be much larger than the mean free path of a particle. The principle of this approach was demonstrated above but the exact meaning of the resultant equations will be dealt with in more detail here. The zeroth moment is the continuity equation which bears more importance for this thesis than the others. This is given in the fluid limit as

$$\frac{\partial \rho}{\partial t} + \nabla \cdot (\rho \mathbf{u}) = S. \tag{1.30}$$

This is the conservation of mass per unit volume - as is always the case with hydrodynamic equations, everything is studied on a “per unit volume” basis. This equation states that any change in density at a given point can only be achieved by a net flow of material at that point and for the addition of material into the system accounted for by S. Equation 1.30 will bear greater significance for results later in this thesis in chapter 5.
The continuity equation given above is the only equation to be used in this thesis but

the remaining equations are documented below for completion. In these equations $\mathbf{u_s}$ is the fluid velocity vector of a species s, P is the scalar pressure, σ is the conductivity of the medium in this instance alone and should not be confused with the energy dependent cross-section, and γ is the adiabatic index.

$$\rho\frac{\mathrm{D}\mathbf{u}_s}{\mathrm{D}t} = \mathbf{J}\times\mathbf{B} - \nabla P, \tag{1.31}$$

$$\mathbf{J} = \sigma(\mathbf{E} + \mathbf{u}\times\mathbf{B}), \tag{1.32}$$

$$\frac{\mathrm{D}}{\mathrm{D}t}\left(P\rho^{-\gamma}\right) = 0. \tag{1.33}$$

The new operator here $\frac{\mathrm{D}y(x)}{\mathrm{D}t}$ is the *material derivative* which constitutes a change in time of a quantity y due to a local change in y at a point x and also the change in y due to material moving into and away from the point x at a rate defined by the local flow speed. More formally, the material derivative is mathematically defined as,

$$\frac{\mathrm{D}}{\mathrm{D}t} = \frac{\partial}{\partial t} + \mathbf{u}\cdot\nabla. \tag{1.34}$$

A detailed description of these equations is unnecessary but equation 1.31 is an application of Newton's second law to fluids, the net force on the left hand side is equal to the sum of the Lorentz force and any gradients in the pressure. Equation 1.32 is a simple version of Ohm's law in vector form and equation 1.33 is a generalised equation of state where γ is chosen based on the thermodynamic properties of the plasma and the processes under examination. Combined with Maxwell's equations (equations 1.16 - 1.19, neglecting the displacement current's negligible influence) these form the theoretical framework known as magnetohydrodynamics or MHD and enables a strong understanding of the low frequency phenomena associated with hydrodynamic scales. This means that any analysis must occur over timescales much larger than the collision timescale. However, there are many phenomena that exist on shorter timescales and require a different approach. This is one advantage the cold plasma model presents.

1.2.4 Cold Plasma Description

The cold plasma model, as explained above, requires that phenomena occur at a frequency greater than the collision frequency which is defined by the thermal speeds in the plasma. An analysis of the physics working at a sub-thermal timescale is possible if the temperature

is, effectively, ignored. Higher frequency phenomena can now be studied without the limitations imposed by the temporal resolution of MHD at the cost of neglecting any thermal effects and any effects uniquely determined by a Maxwell-Boltzmann distribution. One useful consequence of the crude assumption that the temperature of each species is zero is that all particles are initially at rest. Having no thermal motion, particle collisions can be ignored and then the only forces acting are the long-range electromagnetic forces which lead to wave modes particular to the electromagnetic nature of plasmas and so are completely absent in neutral gases. These electromagnetic wave modes can be studied in an analytical treatment and dispersion relations can be attained for a number of configurations of magnetic fields. The cold plasma description also highlights the difference in timescales for the characteristic wavemodes of each species which can be critically important in selecting a parameter regime in, for example, experimental studies of plasmas.
All of these methods are perfectly valid provided that the specific methodology is appropriate and the strengths and weaknesses of each description is known. All manner of plasmas have been studied extensively such as astrophysical (including solar and interstellar), fusion, discharge lamps and low density, low temperature plasmas for industrial applications which are becoming more important in modern day manufacturing methods. Of particular value to the circuitboard manufacturing industry is the concept of a "sheath" - an electro-positive region of charge owing to the greater mobility of electrons. Most sheaths in industrial settings are prescribed a voltage (they are driven) but for this thesis the so-called "floating sheath" is more relevant.

1.3 The Plasma Sheath

When a neutral body is immersed in a quasi-neutral plasma the more mobile electrons will attach to the body and a negative potential will develop. The now negatively charged wall will attract ions and a competition of fluxes ensues until the number flux of ions towards the wall is matched by that of the electrons. At this stage, a steady-state floating sheath has developed with a potential that is no longer evolving in time. An analytical form for the floating sheath can be initially found by solving Poisson's equation (equation 1.16 in 1D) for the densities associated with each charge species,

$$\frac{\partial^2 \phi}{\partial x^2} = \frac{e(n_e - n_i)}{\epsilon_0}. \tag{1.35}$$

If cold ions are assumed and the electrons possess a Boltzmann distribution then the electrons will have an exponential decay in density and the ions will follow the conservation law given in equation 1.30,

$$n_e = n_0 \exp\left(\frac{e\phi}{k_B T_e}\right), \tag{1.36}$$

$$n_i(x) = \frac{n_0 u_0}{u_i(x)}. \tag{1.37}$$

The ions have been described as cold, and therefore have no significant initial velocity but the velocity at any point x in the sheath can be calculated by conserving energy,

$$\frac{1}{2} m_i u_i(x)^2 = e\phi + \frac{1}{2} m_i u_0^2, \tag{1.38}$$

$$\implies u_i(x) = \sqrt{\frac{2e\phi}{m_i} + u_0^2}. \tag{1.39}$$

Substituting equation 1.39 into equation 1.37 and then substituting this result and equation 1.36 into equation 1.35 will yield equation 1.40,

$$\frac{\partial^2 \phi}{\partial x^2} = \frac{e n_0}{\epsilon_0} \left(\exp\left(\frac{e\phi}{k_B T_e}\right) - \left(1 - \frac{2e\phi}{m_i u_0^2}\right)^{-\frac{1}{2}} \right). \tag{1.40}$$

Equation 1.40 is the differential equation which governs the competition of fluxes between ions and electrons in the sheath region which ultimately determines the formation and structure of the sheath potential. Steps towards a solution can be made by multiplication by $\frac{\partial \phi}{\partial x}$ which permits integration of the equation,

$$\begin{aligned}
\frac{\partial \phi}{\partial x}\frac{\partial^2 \phi}{\partial x^2} &= \frac{\partial \phi}{\partial x}\frac{e n_0}{\epsilon_0} \left(\exp\left(\frac{e\phi}{k_B T_e}\right) - \left(1 - \frac{2e\phi}{m_i u_0^2}\right)^{-\frac{1}{2}} \right), \\
\frac{1}{2}\left(\frac{\partial \phi}{\partial x}\right)^2 &= \int_0^x \frac{\partial \phi}{\partial x}\frac{e n_0}{\epsilon_0} \left(\exp\left(\frac{e\phi}{k_B T_e}\right) - \left(1 - \frac{2e\phi}{m_i u_0^2}\right)^{-\frac{1}{2}} \right), \\
\frac{1}{2}\left(\frac{\partial \phi}{\partial x}\right)^2 &= \frac{e n_0}{\epsilon_0} \left(\frac{k_B T_e}{e} \exp\left(\frac{e\phi}{k_B T_e}\right) - \frac{k_B T_e}{e} - \frac{m_i u_0^2}{2e}\left(1 - \frac{2e\phi}{m_i u_0^2}\right)^{\frac{1}{2}} + \frac{m_i u_0^2}{2e} \right).
\end{aligned} \tag{1.41}$$

A solution to equation 1.41 is not possible through analytical means but a limit on the entry speed u_0 for the ions can be determined.

1.3.1 The Bohm Speed

The right hand side of equation 1.41 must be positive in order for a real solution to exist. What this really translates to is a greater density of ions than electrons in the sheath region. A strong potential field will quickly diminish the electron flux but in the case of smaller potentials this won't always be guaranteed. The bracket on the right hand side of equation 1.41 can be Taylor expanded around $\phi = 0$ to second order to reveal a lower limit on the initial speed of ions.

If the bracket terms in equation 1.41 are called κ then to second order the Taylor expansion is,

$$\kappa(x) \approx \kappa(a) + \frac{\kappa'(a)}{1!}(x-a) + \frac{\kappa''(a)}{2!}(x-a)^2. \tag{1.42}$$

These terms in turn for $a = 0$ are;

$$\begin{aligned}
\kappa(a) &= \frac{k_B T_e}{e} - \frac{k_B T_e}{e} + \frac{m_i u_i^2}{e} - \frac{m_i u_i^2}{e}, \\
&= 0; \\
\kappa'(a) &= \exp\left(\frac{e\phi}{k_B T_e}\right) - \left(1 - \frac{e\phi}{m_i u_i^2}\right)^{-\frac{1}{2}}, \\
&= 0; \\
\kappa''(a) &= \frac{e}{k_B T_e}\exp\left(\frac{e\phi}{k_B T_e}\right) - \frac{e}{m_i u_i^2}\left(1 - \frac{e\phi}{m_i u_i^2}\right)^{-\frac{3}{2}}, \\
&= \frac{e\phi^2}{2k_B T_e} - \frac{e\phi^2}{4m_i u_i^2}.
\end{aligned}$$

Using these results in equation 1.42 and stipulating that it must be greater than or equal to zero:

$$\begin{aligned}
\frac{e\phi^2}{2k_B T_e} - \frac{e\phi^2}{2m_i u_i^2} &\geqslant 0, \\
\frac{1}{k_B T_e} - \frac{1}{M u_i^2} &\geqslant 0.
\end{aligned}$$

For the case of the minimum ion velocity the two terms on the left hand side are equal and the speed is called the *Bohm speed*,

$$u_B = \left(\frac{k_B T_e}{m_i}\right)^{\frac{1}{2}}. \tag{1.43}$$

This analysis is only valid for a collisionless sheath: the development of a sheath structure in an environment without collisions with neutral particles. Mathematically describing a collisional sheath is a more nuanced process with no universally accepted analyticaly approach. Various approaches have been taken, notably by Godyak and Sternberg (1990) and Riemann (1991). Ultimately, in the current state of the field, simulations are required to dissect any clear conclusion from a discussion of the effects of ion-neutral and electron-neutral collisions in sheath formation.

1.3.2 The Floating Potential

To calculate this potential given by ϕ_w here, the mono-directional flux from a Maxwellian plasma must be defined using $v_{th} = \left(\frac{8k_B T}{\pi m_e}\right)^{\frac{1}{2}}$,

$$\begin{aligned}\Gamma_e &= \frac{1}{4} n_e(x) v_{th}, \\ &= \frac{1}{4} n_0 \exp\left(\frac{e\phi_w}{k_B T_e}\right)\sqrt{\frac{8k_B T_e}{\pi m_e}}.\end{aligned}$$

The flux from the ions is calculated from the mass-conservation calculation performed earlier except u_B can now be used instead of some unknown u_0,

$$\begin{aligned}\Gamma_i &= n_0 u_B, \\ &= n_0 \left(\frac{k_B T_e}{m_i}\right)^{\frac{1}{2}}.\end{aligned} \tag{1.44}$$

Equating both of these fluxes gives an expression for the steady-state wall potential for a floating sheath.

$$\begin{aligned}
\Gamma_e &= \Gamma_i, \\
\frac{1}{4} n_0 \exp\left(\frac{e\phi_w}{k_B T_e}\right) \sqrt{\frac{8 k_B T_e}{\pi m_e}} &= n_0 \left(\frac{k_B T_e}{m_i}\right)^{\frac{1}{2}}, \\
\exp\left(\frac{e\phi_w}{k_B T_e}\right) &= \left(\frac{2\pi m_e}{m_i}\right)^{\frac{1}{2}}, \\
\phi_w &= \frac{k_B T_e}{2e} \ln\left(\frac{2\pi m_e}{m_i}\right).
\end{aligned} \tag{1.45}$$

Equation 1.45 predominantly depends on the electron temperature and ion mass given that the electron mass is always a constant. The wall potential always evaluates to be negative as the argument of the logarithm function is always less than 1 which aligns with the physical expectation of a negative potential for a higher charge density of electrons than ions on the wall. These types of sheaths are rarely used in manufacturing processes because there is a pressing need to control the particle energies to achieve the desired structures but they are still a common occurence. The passing of satellites through the interplanetary medium will initiate a floating sheath on the satellite exterior and the diagnosis of electron plasma properties with a Langmuir probe will exploit the floating sheath.

1.4 Conclusion

This first chapter has presented a series of models that capture the greatly varying behaviour that plasmas exhibit and some fundamental results. Each model has its own strengths and weaknesses and their suitability towards a particular problem ultimately depends on the context. For this thesis, the setting is the injection of deuterium pellets into magnetically confined fusion reactors. The pellets are extremely cold and dense compared to the fusion plasma and it is initially neutral but it once immersed in the plasma will develop a floating sheath making for an interesting contrast in parameters. The pellets themselves ablate (or evaporate) abruptly upon injection and release their atoms into the plasma in an initially neutral and gaseous form of an ablation cloud. The cloud eventually ionises and reinforces the density of ions in the machine. The concept of the fusion machines and a review of

the literature is explored in chapter 2. Chapter 3 will explore and justify the use of the continuous slowing down approximation (CSDA) which is needed later to develop a model for stopping electrons within an ablation cloud. The next three chapters contain the new research that has been carried out starting with chapter 4 which compares the ablation of the solid-state pellets in tokamaks to the evaporation of aerosol droplets by borrowing an empirical law from evaporation studies. This permits calculations to be performed which define quantities such as density of the neutral cloud and its size. Chapter 5 uses these quantities to test the CSDA in a tokamak environment by exploring how a distribution of tokamak electrons will be stopped and distribute themselves spatially within the cloud. It also considers the influence of a potential field within the cloud that is defined arbitrarily but also considers calculations to determine the field produced by any stopped electrons. Chapter 6 captures all of these details by evolving the system in time and examining the differences that develop in the system when self-charging, a sheath field and the generation of ions due to ionising events are cummulatively added. A series of conclusions are drawn in chapter 7 to summarise the results presented within the thesis.

Chapter 2

Nuclear Fusion and Cryogenic Pellets

The previous section presented some typical and common ideas and results associated with plasma physics that will be of relevance to this thesis. However, there is a very real application of the work contained in this thesis and this chapter will set the context for that work. This work relates to the most obvious and publicised application of plasma physics: nuclear fusion. Nuclear fusion is the dream energy source of humankind, having no carbon emissions and almost unlimited resources but the technical challenge it presents has kept it from reality. This chapter will explain some of the fundamental issues with achieving steady-state operation of a fusion machine with a particular focus on the refuelling processes and the associated phenomena and research.

2.1 Nuclear Fusion

The pursuit of nuclear fusion as a viable means of energy has been a challenge for many decades. Progress has been made, funding has been approved and machines have been getting larger, culminating in the construction of the ITER machine in Cadarache. Whilst there are a multitude of fusion reactions available, the most favourable is the D-T reaction (equation 2.1) taken from Morse (2019),

$$ {}^{2}_{1}\mathrm{D} + {}^{3}_{1}\mathrm{T} \longrightarrow {}^{4}_{2}\mathrm{He} + {}^{1}_{0}\mathrm{n}. \tag{2.1} $$

The energy released by this reaction is determined by the difference in the total binding energy of the products and the reagents, termed the mass defect. In this case the mass

defect is appoximately 17.6MeV, split across the alpha particle and neutron in such a way that satisfies momentum conservation. With E representing the total binding energy of products and reagents denoted by a subscript and Θ is the mass defect the energy is conserved according to equations 2.2 - 2.4,

$$E_r = E_p + \Theta, \tag{2.2}$$
$$\Theta = \Theta_\alpha + \Theta_n, \tag{2.3}$$
$$= 3.02\text{MeV} + 14.56\text{MeV}. \tag{2.4}$$

The parameter space fusion plasmas occupy is vastly different to that of technological and solar plasmas. Temperatures of $\approx 10^7$K (or 1keV) at a density of approximately 10^{19}m^{-3}, a pressure of about 1 atmosphere and a magnetic field in some cases of 1T are not uncommon. These high temperatures and pressures are needed to give the particles enough energy to overcome any electrostatic repulsion and get close enough to each other such that the strong nuclear force dominates and draws ions together. After the fusion of the nuclei, the mass defect is released as energy. If the sum total of all energy released by the reactions is greater than the energy required to keep the plasma confined then $Q = 1$ (breakeven) is said to be achieved. The conditions needed for breakeven to occur have been summarised loosely in the Lawson criterion by equating power losses and gains in the system. Typically this captures the injected power to heat the plasma, any self-heating that occurs from fusion products, all manner of radiative losses such as bremstrahlung and synchrotron radiation, and conductive heating losses. The Lawson criterion is presented in full in equation 2.5 for an ion density n and a confinement time τ,

$$n\tau = \frac{3T}{\frac{1}{4}\langle\sigma v\rangle E_f(\frac{1}{Q} - f_c - \chi_R)}, \tag{2.5}$$

where $\langle\sigma v\rangle$ denotes the average collision rate per unit particle density, E_f the mass defect, Q the ratio of created to injected power, f_c and χ_R are numbers describing the efficiency of self-heating and radiative losses respectively. Typically, this expression is evaluated for D-T reactions with $Q = 2$ which defines all other parameters and creates a function that varies implicitly with T through the collisional term $\langle\sigma v\rangle$. This leaves only n, τ_E and T free to vary creating the *triple product* for energy breakeven. At 10keV this evaluates to equation

$$n\tau > 10^{20}\text{m}^{-3}\text{s}. \tag{2.6}$$

When the product of the particle density and confinement time exceeds this limit the reactor is now producing more energy than is needed to maintain the plasma. The mission of fusion research is to create a machine that is self-sustaining and requires no input power. Such a machine would effectively power itself.

The plasma properties needed to achieve breakeven, particularly the temperature, make for a imposing challenge to contain the fuel in a chamber. Novel approaches that exploit the electromagnetic properties of the plasma have been developed to contain the plasma in a magnetic vessel contained within a physical one. For a plasma to be macroscopically manipulated by magnetic forces the influence of fluid or thermal forces should be comparatively small. In a fluid context the thermal pressure must be much smaller than the magnetic pressure. This defines the *plasma beta*. An approximate calculation proceeds as

$$\begin{aligned}\beta &= \frac{P_T}{P_B}, \\ &= \frac{2nk_BT\mu_0}{B^2}, \\ &= \frac{2\times10^{19}\mathrm{m}^{-3}\times1.38\times10^{-23}\mathrm{JK}^{-1}\times10^{7}\mathrm{K}\times4\pi\times10^{-7}\mathrm{Hm}^{-1}}{1^2\mathrm{T}^2}, \\ &\approx 3.468\times10^{-3}.\end{aligned} \tag{2.7}$$

This is comfortably less than 1 for a typical set of fusion parameters. Consequently, a magnetic field can shape and mould the plasma into a geometry that can be matched by the applied field, and ultimately keeps the plasma-facing components of any confinement chamber safe from sputtering by high energy particles. In the end, a toroidal geometry won out over others in a competition of experiments in confining hot plasmas with a magnetic field and has set the stage for fusion research firmly in a toroidal magnetic chamber, or tokamak.

Tokamaks have a poloidal (around the ring the short way) and a toroidal field (around the ring the long way), the sum of each resulting in a helical field along the toroidal direction with a magnitude of about 1T in modern machines. The geometry of these machines is simply illustrated in figure 2.1. This field configuration has been selected for a number of reasons but the reason with most contemporary relevance is the defence against instabilities. The topic of instabilities will be discussed in slightly more detail later.

Like any other form of new energy source, a wealth of concerns must be addressed in order to become viable for commercial use. One of the key issues is the prospect of

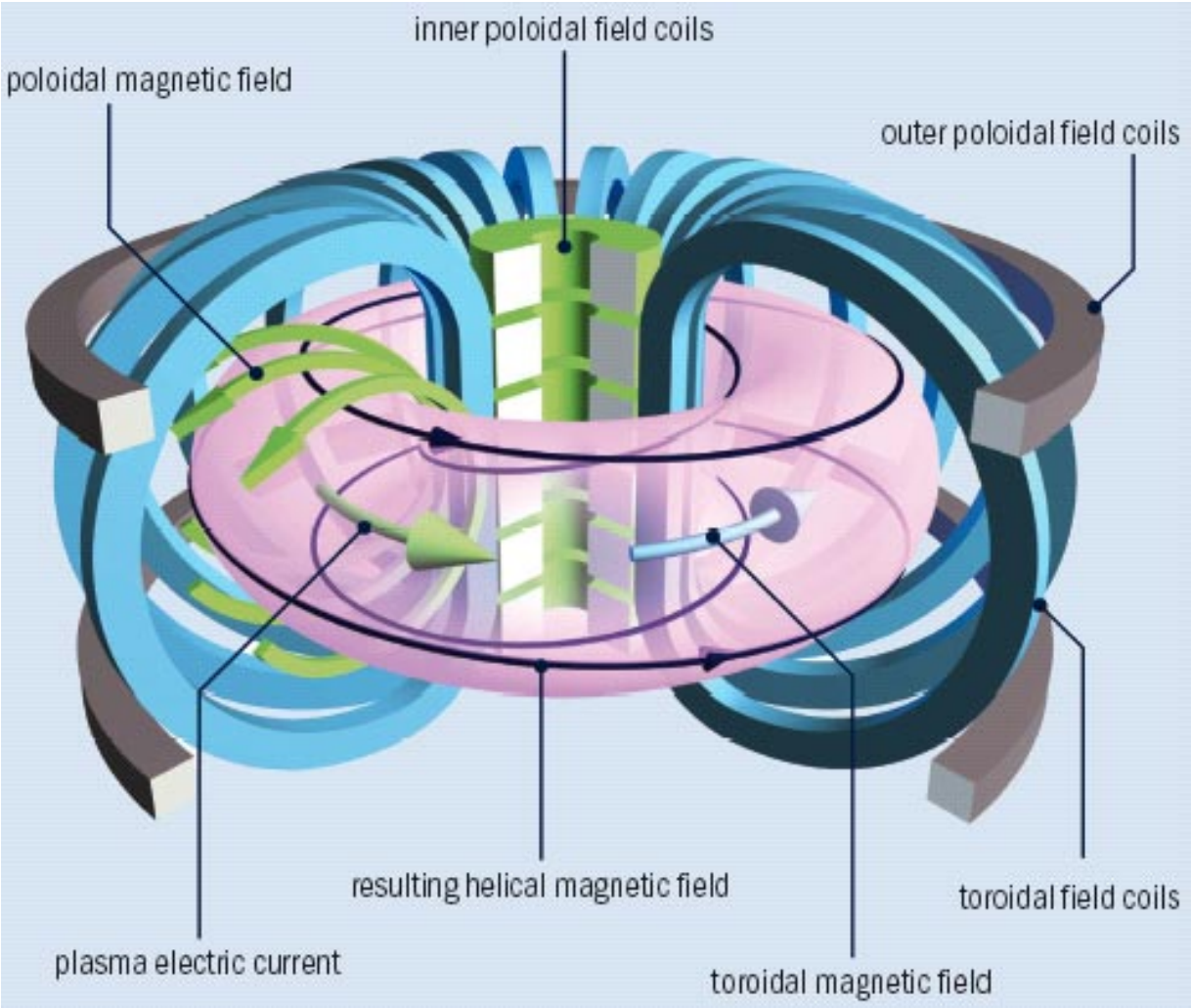

Figure 2.1: Cartoon schematic of the main magnetic field components in a tokamak. The poloidal (green, square arrows) and toroidal (blue, round arrows) sum to give a total helical field (black lines with arrows). Image taken from https://physicsworld.com/a/fusion-the-way-ahead/

continual energy release. This is a problem that certain renewable sources will not be able to overcome such as wind and solar. Looking back at the Lawson criterion, there are two key parameters which inhibit the success of a steady-state fusion reactor with a continuous release of energy: the prolonged confinement of the plasma and the fuel density within the vessel. The solution to confinement carries complications in the form of managing instabilities and minimising perturbations to the equilibrium of the plasma. This challenge is not the focus of this thesis and will only be discussed in sparse detail throughout. The challenge that is being tackled in this document is the subject of plasma density.

Establishing the initial density of the plasma "before any fusion reactions", as such, is a separate problem to that of maintaining the density during the operation of the machine. For any tokamak at startup, there is a finite amount of fuel within the vessel that is available for fusion reactions. Over time, this fuel will need replenished in order to maintain a density great enough that the Lawson criterion is satisfied. Of course, if the tokamak can continue to operate that would be ideal and is the goal of the ITER project but this will also require an addition of deuterium and tritium particles into the chamber. The remainder of this chapter is devoted to a review of the progress and current state of refuelling procedures and the understanding of the phenomena observed or surmised during operation.

2.2 Refuelling

There are two components to the plasma fuel for the D-T reaction. The half-life of tritium (about 12 years) makes storage possible but not cost-effective for large projects which span many decades. This problem has found a subtle solution. Coating the walls of the reactor in lithium will naturally release tritium if a neutron successfully interacts with a lithium atom undergoing the following reaction:

$$^{6}_{3}\mathrm{Li} + ^{1}_{0}\mathrm{n} \rightarrow ^{4}_{2}\mathrm{He} + ^{3}_{1}\mathrm{H}. \tag{2.8}$$

This is the chosen method for refuelling the reactor with tritium for ITER (see Kumar et al. (2008)) but the challenge of refuelling the deuterium still exists which the remainder of this chapter will discuss.

2.2.1 Gas-puffing

In early tokamak designs, refuelling of deuterium was done by means of "gas-puffing". This was a simple process of injecting gas at the outer edges of the tokamak vessel and relying on transport properties of the plasma to move the initially neutral material towards the plasma core - this is mentioned in sparse detail in a JET project report Rebut et al. (1985). This is a rather simple approach but unfortunately saw little success. The poor penetration of the gas into the plasma means a significant fraction of the gas flows along the periphery of the plasma and towards the exhaust. The problem here is two-fold: not only is there a poor deposition of fuel in the plasma centre but the addition of fuel exclusively at the

plasma edge encourages instability. The Greenwald density limit (which is accounted in Greenwald (2002)) exhibits a scaling law in units of $10^{20}\mathrm{m}^{-3}$ which increases with total plasma current (in MA) and decreases with the major radius (in m) of the tokamak. This density limit is also alluded to in Rebut et al. (1985).
Violation of this density limit at the plasma edge has been found to be associated with a number of phenomena detrimental to plasma stability and have been collated with their associated parameter regimes in Greenwald (2002). The collapse or breakdown however is only associated with densities that supersede this limit near the plasma edge. The shape of the density profile may then offer a means to manoeuvre around this constraint and structure the plasma such that prohibitive densities are achieved at points that preserve stability. Critically, the author states that "particles added to the central plasma apparently don't induce density limiting pehnomena". If this is indeed the case for all toroidal machines then it is of great interest to the fusion community to deposit as much material as possible to the core of the plasma to circumvent collapse. This is a key area where gas-puffing fails and an alternative method is needed. An unlikely candidate exists in the form of a heating method - neutral beam injection.

2.2.2 Neutral Beam Injection

Neutral Beam Injection (NBI) is designed to be a heating method, to increase the plasma energy as a means to access the Lawson criterion. Early designs began in 1985 on the Joint European Torus (Rebut et al. (1985)) and proved to be valuable as a heating source to the extent that 17MW sources will be provided for ITER Sonato et al. (2009). The process of heating via high energy neutrals is rather straight-forward. A low temperature plasma is produced in a chamber and accelerated (to about 100keV in the projected case of ITER) into a chamber populated with electrons that recombine and neutralise the ions before moving at high energy into the tokamak. The plasma contained in the tokamak then ionises the material and it becomes confined by the magnetic field in the same way as the plasma. Of course, the primary focus with neutral beams is to heat the plasma, not refuel it however the injection of matter itself may contribute significantly to populating the plasma interior with ions as a secondary effect. Unfortunately this is not the case, as reports from Wagner et al. (1982) demonstrates in figure 1 of the article. The density barely increases however a significant increase in temperature is observed in panel d of the figure. In light of this failure, an additional method exists (intially proposed by Spitzer in 1954 but a comprehensive review by Pégourié (2007) covers contemporary phenomenological

and technical understanding) that has presented more promising results .
A much more utilitarian approach has been offered, and delivers much more favourable density deposition than gas puffing, in the form of cryogenic pellet injection. The benefits of this new method outweigh the convenience offered by gas-puffing and cryogenic pellet injection techniques became the norm for tokamak refuelling processes. Understanding the physics at work during pellet injection through both modelling and experimental studies to maximise pellet penetration into the plasma and minimising particle losses at the plasma edge are a clear path to satisfying the Lawson criterion.

2.2.3 Pellet Injection

Cryogenic pellets, of a temperature of approximately 14K are injected at high velocity (of several hundreds of metres per second, although this is machine-dependent) into the highly energetic tokamak plasma. The particles strike the pellet and transfer energy to the neutrals which break free from their inter-molecular bonds and form a vapour that envelopes the pellet. The process itself is probably quite similar to sublimation although it has been referred to almost interchangeably as evaporation or ablation (a term more commonly used in high-energy laser experiments) to describe the process which has been documented in publications such as Milora and Foster (1978), Parks (1992) and Pégourié (2007). The strengths of pellet injection has seen it become the preferred method of deep fuelling and has been planned for ITER for decades (Gouge et al. (1992)) with continuing progress updates (Combs et al. (2012)) and is already suggested for DEMO (Vincenzi et al. (2015)). The arguments for this preference will be covered in minor detail in the following section.

2.2.4 The Benefits of Pellet Injection

Instability excitation and heat flux mitigation

Instabilities such as edge-localised modes (ELMs) have become a serious concern to the success of functioning reactors. Violent expulsions of hot plasma directed towards the plasma-facing components causes significant damage necessitating replacement. These expulsions also threaten the confinement of the plasma and the massive release of energy is a hazard to the divertor region which must extract an immense heat flux. Mitigation of ELMs has become a topical and essential focus of fusion research to accommodate the

large scale of future reactors and prove the efficacy of fusion. To that end, the injection of smaller (sometimes called "shattered") pellets that are intended to perturb the outer region of the plasma can excite ELMs to occur more frequently, exciting smaller ELMs and releasing less energy during a single event Evans et al. (2008) and Baylor et al. (2016). This eases the power load on the divertor and also preserves the integrity of the plasma facing components. Therefore, the use and study of pellets can be of immense value to maintaining the lifetime of internal structures of the tokamak vessel and minimising costs to future and ongoing projects. Some studies have shown that there is no significant benefit to pellet injection to minimising power loads at the divertor compared to gas puffing but with a higher injection frequency this may be possible Tvalashvili et al. (2015)
A thorough examination of the effects of pellet injection on the onset of ELMs is recorded in Lang et al. (2004). An interesting result was presented in section 3 of the article that smaller pellet sizes than routinely used for fuelling purposes would be sufficient to initiate an ELM. In addition to this, slower injection speeds were reported as being more valuable for ELM excitation owing to the greater perturbation at the plasma due to the greater local ablation. A combination of these observations could be useful in preserving fuel for experimental runs over months and preserving the energy budget for break-even experiments that would be so costly with using NBI.
Loarte et al. (2014) presented a key conclusion from pellet studies on the D-IIID tokamak in figure 9 of that article that is of relevance to future reactors, namely ITER. With the heat loads on the divertor being unsustainable for continuous operation, which is the desired output from the ITER project, it is essential to find a way to minimise the energy deposited on the divertor plates as a result of ELMs during operation. Figure 9 of Loarte et al. (2014) illustrates that pellet-induced ELMs undergo a dramatic (about an order of magnitude) decrease in peak energy flux on the divertor plates and a similar decrease is seen in the average load. Of course, upscaling to ITER will not be simple but the results themselves are encouraging and demonstrate the need to invest resources in researching and understanding the fundamentals of pellet ablation.

Density profile

Milora et al. (1995) provides an extensive examination of the possible benefits of pellet injection when contrasted with gas-puffing methods. As was discussed briefly in an earlier section, the deposition of fuel is essential to satisfying the Lawson criterion but if the fuel

is deposited at the edge, instabilities and damaging phenomena may occur. It becomes essential therefore to insert the fuel at a point much closer to the core of the plasma. Studies such as those conducted by Greenwald et al. (1984) demonstrate two things. The first is that a more favourable confinement of energy in the tokamak (in this case Alcator C-Mod) can be achieved and consequently a more favourable Lawson product can be attained too. These results are presented concisely in figures 1 and 4 of Greenwald et al. (1984). The second is that the electron density clearly increases upon injection into a typical tokamak plasma as demonstrated from figure 2 in Greenwald et al. (1984), increasing by a factor of 2. Experimental results from Baldzuhn et al. (2019) indicate that the average density along a line in the Wendelstein -7X stellerator - a device similar to tokamaks but with a fundamental difference in geometry - increases by almost a factor of 2. This of course, makes no statement on where the density has increased, only that along a line, it has on average increased which could be exceeding the Greenwald density limit but on terms that do not excite exterior instabilities. Once more, the case has been made here that pellets can effectively increase the density within the reactor plasma and their study for devices like ITER is needed to maximise their potential benefits.

Plasma shutdown and "killer" pellets

Pellet injection can also serve as a means to mitigate the damage caused by disruptions within the vessel. Recent results from Commaux et al. (2010) have demonstrated that the injection of shattered D_2 pellets can significantly increase local electron density and consequently cause a "thermal quench" and a "current quench". During disruptions, currents known as halo currents may flow from the plasma to the vacuum vessel walls which may cause significant damage when the $\mathbf{J} \times \mathbf{B}$ force acts on the vessel wall. Smaller poloidal halo currents (see figure 2 of Commaux et al. (2010)) are observed for gas injection (known to mitigate disruptions) and similar profiles are seen for small pellet injections. Suggestions are made in this article to explore the shattering processes of these pellets given that approximately 30% of the mass tends to remain in a singular object which could be simultaneously used to fuel the vessel while the smaller fragments manage disruptions. The authors also state the value in studying the contribution to shutdown that shattered pellets may have with different elemental constituents, notably neon, due to the large number of electronic transitions and radiative losses that may occur. The results make a credible case for "killer" pellet injection into tokamaks to avoid this damage and other phenomena at the expense of large heat loads on the divertor.

Some prior numerical studies to model the losses due to radiative transitions in the pellet and plasma atoms (once recombination occurs) include Lengyel et al. (1999). The authors here performed numerical simulations of both carbon and neon pellets with reasonable agreement on the similarity between calculated and observed penetration depths for carbon pellets in Wendelstein 7-X and neon in ASDEX-Upgrade. Discrepancies between the predicted and observed radiative emission are put down to poor radiative transport modelling and background emission in the case of the neon experiment. Additional work was also taken to understand the loss of runaway electron currents (also reported in Yoshino et al. (1997) for magnetic perturbations) in Harvey et al. (2000) for similar perturbations. The process is understood to limit the energy available to electrons as the approach the wall, therefore reducing the runaway current.
These results indicate that "killer" pellets are suitable methods for engaging the fast shutdown of the plasma if there is a risk of losing control. The study of these pellets in shutting down the plasma has not been carried out extensively but is shown to be desirable but if an effective model was to be produced then additional studies may be prompted.

2.3 Cryogenic Pellets

One of the most remarkable things about using cryogenic pellets to refuel a fusion plasma is the tremendous difference in scale lengths and values of parameters that they share. The temperature is an obvious comparison to draw but properties such as density and radius merit attention. These differing quantities create the most unique physical arena exhibiting all manners of phenomena which will be presented in due course but the parameter range must first be established. This is presented in table 2.1.

Table 2.1: The vastly different physical properties of the pellet and plasma compared. Data taken from Rebut et al. (1985), Keilhacker et al. (1999) and Geraud et al. (2007) for JET.

Physical Quantity	**Pellet**	**Tokamak**
Radius/m	10^{-3}	1
Volume/m^3	10^{-8}	10^2
Density/m^{-3}	10^{28}	10^{19}
Temperature/K	~ 10	10^7
Lifetime/s	$\sim 10^{-3}$	~ 1

2.3.1 Properties and Phenomenology

The most visually striking and dominant feature in the interaction between pellets and plasma is the formation and evolution from a "two-body" pellet-plasma system to a "three-body" pellet-*cloud*-plasma system. Following the immersion into the plasma environment, particles from the plasma strike the pellet surface (in a process akin to sputtering) and release particles if their incident energy is greater than the sublimation energy of solid hydrogen. The particles which are emitted from the surface are assumed to be neutral, molecular hydrogenic isotopes for refuelling purposes but other experiments may use pellets doped with elements such as aluminium or neon to rapidly cool the plasma to shut down the machine. Portions of the ablatant cloud that become ionised suffer limited expansion across the field relative to the parallel expansion producing an ellipsoidal, cigar-shaped clouds. Within the context of fusion this process is called *ablation*.

The topic of ablation itself is mostly confined in fusion studies to the study of the *ablation rate*. This is the quantity that connects the plasma to the evolution of the three-body system and prescribes the entire system's behaviour. The energy from the plasma releases neutral particles into the cloud which interacts and slows any additional particles from the plasma that enter the cloud. Inelastic collisions then mute the energy impacting the pellet and causes less ablation than previously which in turn effects the evolution of the cloud. This feedback system is dependent on the initial conditions of the plasma and pellet chemical composition. The combination of these two determine the ablation rate which has been explored heavily in this field (see Garzotti et al. (1997),Yu et al. (2009),Panadero et al. (2018)), particularly in Parks and Turnbull (1977) which was one of the earliest attempts to model the process that saw success. This competing model will be addressed in a later section.

In the remainder of this thesis, the instantaneous pellet size is denoted by r_p and the instantaneous cloud radius (centred on the centre of the pellet) is denoted by r_c. A cartoon depicting the three-body system is illustrated in figure 2.2. A crucial quantity for understanding ablation on a molecular level is the intermolecular bond energy, mentioned briefly in relation to the sputtering of molecules from the pellet surface. Where data can not be found for the sublimation energy, an approximate result can be calculated by simply adding the heat of fusion and heat of vaporisation for hydrogen molecules including some conversion factors. This returns a total energy per bond of the order 5.27meV. This is supported by Gál et al. (2008) with a reported sublimation energy of 5meV.

Two inter-related phenomena dominate the diagnostics and discussion surrounding these

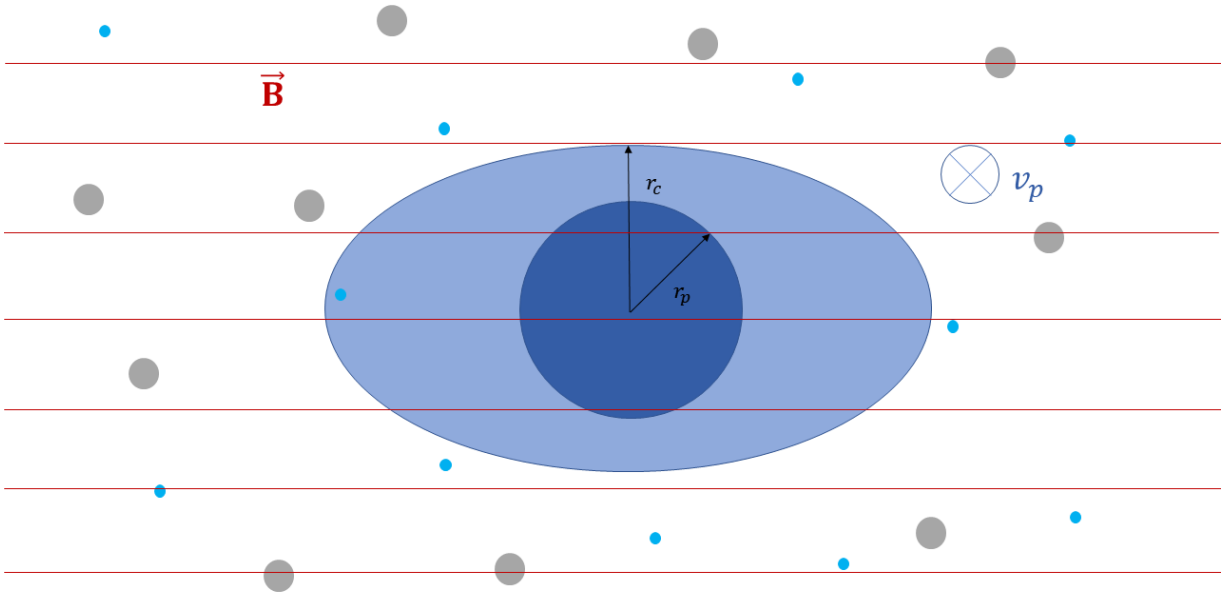

Figure 2.2: A cartoon depicting the ablation and cloud structure surrounding a pellet in a tokamak. The deep blue represents the pellet enveloped by a molecular hydrogen cloud in a lighter blue. Plasma particles, electrons and ionic isotopes of hydrogen, surround the pellet-cloud system which is moving into the page. The magnetic flux density is represented by the red lines which limit expansion of an ionised portion of the cloud perpendicular to the field vector. This produces the elongated, cigar-shaped clouds seen from pellet-injection experiments.

systems: the atomic emission and the striations. The matter of atomic emission concerns the excitation and relaxation of electrons in atomic hydrogen. The neutral atoms in the cloud undergo excitation from collisions and either directly or through higher excitation and subsequent relaxation results in an electron in the $n = 3$ state. From the $n = 3$ energy state the electron relaxes to the $n = 2$ energy state with an associated release of radiation - in this particular case Balmer alpha at 656nm. Being an electronic transition there is very little influence from the nuclear structure and there will be equivalent lines emitted from isotopes such as deuterium and tritium. It is worth stating a rather obvious fact for clarity. Balmer alpha is a neutral and atomic spectral line from hydrogen. These observations mean that any H_2 that is released from the pellet must dissociate somehow and must not currently be ionised to produce the line. It is therefore expected that a variety of species will exist in the cloud that is initially neutral but over time the population of particles is likely to vary.

The atomic emission itself can be recorded via cameras and the intensity across the cloud measured as has been achieved in Cseh et al. (2017) and is a well-understood process. However, the periodic structures of emission trace out a cloud-shaped structure along the trajectory of the pellet are a mystery. Known as *striations* they have had a variety of explanations over the course of their study but a widely accepted understanding continues to evade the community. These striations are presented in an image taken from Wurden et al. (1990) given in figure 2.3a with the banded structure clearly visible. Suggested mechanisms have included the Rayleigh-Taylor instability, the crossing of rational q-surfaces and particle drifts within the cloud relative to neutral matter but none have met widespread acceptance within the fusion community. These solutions have been explored briefly in Pégourié (2007) with the references therein expanding further.

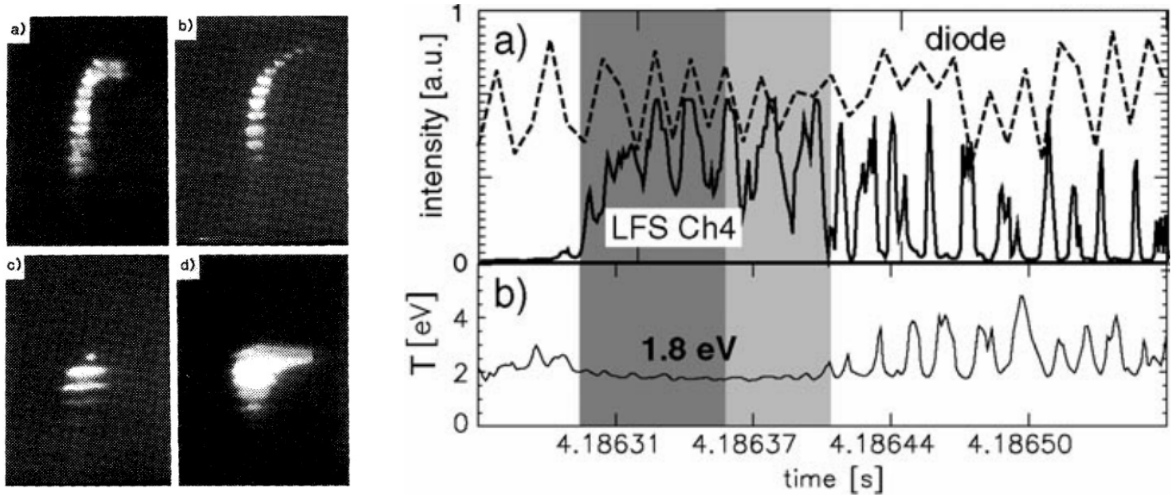

(a) Ablation clouds

(b) Balmer alpha intensity

Figure 2.3: Panel a) is an image (Wurden et al. (1990)) from a Dα camera that captured emission from an ablation cloud in ASDEX, presenting the striations clearly. Panel b) is taken from Müller et al. (2002). The variation in intensity of the Dα emission in time is represented in the dashed line of the panel from the upper portion of the figure.

Irrespective of any understanding of the formation of the banded structures in these ablation clouds one thing is taken as fact: the formation and evolution of the cloud, and indeed the entire system, is dependent on the ablation rate. This quantity is the rate at which particles are released from the solid state into the gaseous state of the cloud, typically measured in s^{-1} and denoted by $\dot{N}$. This is the key quantity in pellet studies that connects the physics and properties of the background plasma to those of the pellet. This quantity is expected to change over time due to a muting of the incident energy flux

due to energy losses in the cloud, thereby causing the emission. Understanding, in a simple way, how the plasma interacts with the cloud and continues to perform ablation with losses considered and a self-consistent and accurate manner is a fundamental challenge of pellet studies. This thesis will develop an alternative solution to this problem but the dominant work in this particular area must be first be studied.

2.3.2 Neutral Gas Shielding Model

The defining model for pellet ablation studies is the neutral gas shielding model, hereby referred to as NGS, from Parks and Turnbull (1977). NGS is a relatively simple model in terms of its premise - the energy flux at the pellet surface and the ensuing thermodynamic exchange releases neutral material as a dense gas. Inelastic collisions in the neutral cloud between the deuterium molecules and the incoming electrons slow the electrons and heat the cloud which in turn modifies the flux and a feedback system results. Perhaps the most important feature of the NGS model is that it is exclusively a neutral shielding model. There is no shielding effect from electrons that have stopped in the cloud due to these collisions.
Some of the integral assumptions in the model are the following:

- The effects of a charged pellet are neglected
- A mono-energetic beam of electrons interacts with the cloud
- The flow of gas in the neutral cloud is assumed to be sonic everywhere.
- The electrons lose their energy due to inelastic collisions but elastic back-scattering and small angle elastic collisions are also included.
- The model permits an expression for the density profile to be derived.

The first three of these assumptions are rather simple to justify. With regards to the charging of the pellet due to electrons it is neglected in this particular study. The most obvious way to incorporate pellet charging is through the floating sheath description which was presented in chapter 1. The expectation here is that the electrostatic potential from the sheath would cause additional stopping of incoming electrons. However, the focus of this work is the shielding due to the neutral gas and is omitted from the model. Similarly, the use of a single mono-energetic beam of electrons simplifies the calculation by ignoring

the contribution of a small portion of high energy electrons in the distribution. These considerations are explored in a later model by Houlberg and Attenberger (1988). The assumption of a sonic flow everywhere in the cloud is employed as a means of solving the system of equations in a simpler manner and assists in closure of the 9 equations in the model. The authors later discard this limiting simplification with a paper that considers the transonic flow of an ablatant cloud Parks and Turnbull (1978).

The incorporation of collisions into this model has been managed for both elastic and inelastic processes. Elastic collisions can cause substantial scattering such that the electron will no longer contribute to the energy flux at the pellet surface with any kinetic energy losses contributing to heating of the cloud. This scattering can come about by either a single back-scattering event or multiple small angle deflections. The cross-sections for both processes are calculated with "double backscatter" events ignored as the remaining energy of those electrons would be negligible. Inelastic collisions are included by means of a fit to data for ionisation, excitation and dissociative processes which is amalgamated into a *loss function* in the article. Both elastic and inelastic processes contribute to a loss of energy flux at the pellet's surface

Finally, the density profile is determined by means of derivation and the prior assumptions. The authors propose early in the article that the density profile should fall "by at least r^{-2}" which is an intuitive relation due to the spherically symmetric expansion in the model. Once the density profile is solved for it is revealed that it does approximately vary as r^{-2}, including some additional terms that do not vary strongly.

These assumptions are applied to a hydrodynamic and thermodynamic model that incorporates elastic and inelastic collisions to moderate the energy flux at the pellet surface. The model is constructed in the following way. Electrons from the background plasma enter the cloud and suffer energetic losses to inelastic processes. Electrons can also be scattered away from the pellet by means of elastic collisions - ions are ignored in this treatment as they are much less mobile. The pellet is additionally protected from the now mitigated electron energy flux due to energy losses to molecular excitation in the pellet and gyrating electrons that do not strike the pellet - this is energy unavailable to heating of the pellet surface. Mass is then conserved at the pellet surface allowing for a calculation of the effluent particle flux at the pellet surface. An understanding of the integrated cloud density is needed and equations are formulated for it in normalised units. At this stage in the development of the model there are nine unknowns and seven equations, necessitating two more equations to achieve closure. This is attained by making the sonic approximation and by considering the effect of particles heating the cloud and the adaptation of the density

profile to accommodate that change with an averaging process to account for anisotropic heating due to magnetic field alignment. This permits solutions for the nine quantities and two essential scaling laws result that were shown to bear agreement with contemporary results in Foster et al. (1977). For the scaling laws detailed in 2.9 and 2.10, T_e is the electron temperature, n_e is the electron density, r_{p0} is the initial pellet radius and $\dot{r}_p$ is the speed at which the pellet's surface recedes,

$$\tau_p \propto T_e^{-1.71} n_e^{\frac{1}{3}} r_{p0}^{\frac{5}{3}}, \tag{2.9}$$

$$\dot{r}_p \propto r_p^{-\frac{2}{3}}. \tag{2.10}$$

What these scaling laws tell us is that a greater electron temperature causes pellets to ablate faster because there is a greater mean energy of particles and more particles occupying the more energetic states. Similarly if there is a greater density of electrons, n_e, there are more electrons striking the pellet in a given time interval and therefore the pellet expires faster. The most clear scaling from equation 2.9 to justify is the scaling of the lifetime with r_{p0}. The pellet should naturally last longer in the plasma if there is more of it to be ablated by the plasma and hence the $r_{p0}^{\frac{5}{3}}$ scaling.The scaling in equation 2.10 can probably be explained by considering that if a pellet is smaller and a constant ablation rate (in terms of particles released per second) would mean that a thicker annulus of matter would be released at smaller r_p than for larger r_p. The determination of a scaling law makes for simple comparison between experimental results in further studies. Owing to the scaling law and the credibility of the model with respect to observations it has become ubiquitous with pellet injection studies, garnering widespread acceptance in the community and is the standard by which any competing models are measured. In absolute terms, the results of the NGS model were compared to experimental observations from the ORMAK tokamak and gave "good agreement". Measured lifetimes of 381μs were found for a predicted 380μs lifetime for a 35μm pellet and 850μs lifetime was observed with a 820μs prediction for a 210μm pellet. The need for these results to be presented here will not yet be apparent to the reader but their relevance to this thesis will be made clear in later chapters.

The strong agreement between prediction and observation encouraged attempts to improve upon these initial results with Milora and Foster (1978) breaking the assumption of continuous flow speeds within the cloud of NGS (similarly addressed in Parks and Turnbull (1978)) and exploring the hydrodynamics more thoroughly. Two key elements that are absent in both models is an examination on the effect that ionisation may have on the

dense neutral cloud and the distribution of energies in the background plasma. These limiting assumptions were discarded in a more robust model proposed by Houlberg and Attenberger (1988) which has since been termed the Neutral Gas Plasma Shielding model (NGPS). Collectively these models have formed a starting point for further work including phenomenological studies such as in Rozhansky et al. (1995) and Krasheninnikov et al. (2011).

In particular a number of numerical works that have followed investigate tokamak and plasma response to an injected pellet either based on these models or calculating quantities based on these models. These works are extensive but some more recent examples include Rozhansky et al. (2004), Lorenzini et al. (2002), Skovorodin et al. (2016) and Pégourié et al. (2005). If the framework of the code does not build itself upon these models then they are the gold standard by which to compare the results of the code which Behringer and Büchl (1989) and Lengyel and Spathis (1994) have demonstrated. Moreover, results from these models have been validated by experimental work and continues to be used in the current decade, particularly in W.a. Houlberg et al. (1992) and Matsuyama et al. (2012). To conclude the subject of the shielding models, they have been discussed in review articles some years after their initial publication, including Milora et al. (1995) and Pégourié (2007), and progress reports on fusion machines (Lloyd et al. (2007)) adding further support for their suitability in the changing direction of the field.

2.4 Conclusion

This thesis will propose an alternative model to NGS. The quasi-static assumption that is employed in the NGS model is justified therein but used to confidently evaluate the hydrodynamic properties of the system. The model proposed later will use the quasi-static assumption to equilibrate the cloud to evaluate other macroscopic quantities. The means by which the shielding of the cloud is performed in this new model also differs from the NGS model. NGS considered particular interactions and their "semi-empirical cross-sections"; excitation, ionisation and dissociation. In place of this, the shielding model developed in this thesis will make use of the continuous slowing down approximation.

This chapter has presented the problem of fusion as energy source for the future by introducing the Lawson criterion and considering the issue of refuelling the chamber. With approaches such as gas-puffing deemed unsuccessful the method of cryogenic pellet injection

has been selected by the fusion community. Pellet injection affords benefits to the density profile and circumvents a violation of the Greenwald density limit but also offers the opportunity for radiative studies with pellets doped with high-Z elements and also the prospect of mitigating the destructive nature of ELMs. The NGS model has been reviewed but after an examination of the more complicated features in the model an simpler model is the focus of this thesis. Before the novel work of this thesis is discussed, a review of the continuous slowing down approximation (CSDA) is conducted in the next chapter.

Chapter 3

The Continuous Slowing Down Approximation

This thesis will be discussing the almost instantaneous immersion of a dense, neutral pellet in a bath of fully ionised hydrogen plasma and the inelastic neutral-plasma collisions that exchanges energy from the plasma to the target. The target in this case is the neutral gas that surrounds the pellet and the projectile is the plasma species that strikes the gas from the background which will lose energy as it moves through the target. The projectile energy is lost through collisions and will either stop if enough energy is lost or will pass through the cloud and strike the pellet with the energy that remains. The concept of collisions were discussed very briefly in Chapter 1. In a gaseous state, a collision can be remarked as having a probability of occurrence given by an energy-dependent cross-section and an associated exchange of energy. This same principle holds true for plasmas when interacting with neutrals with the plasma particles losing energy to the neutrals. In particular, the energy is lost from the high energy projectile and delivered to the bound electrons in the target atoms. This energy exchange could be enough to ionise the atom or just enough to raise the bounded energy state of an electron. Other mechanisms exist in which the projectile is slowed by interacting with the nucleus of the target atoms or with radiation but we expect from observations of pellet-cloud systems that electrons in the target are interacting heavily with the projectile. Emissions of Hα from these systems indicate significant ionisation which of these 3 mechanisms only electronic interactions could achieve. This is well studied in the literature with works such as Wurden et al. (1990) examining not only Hα but also Hβ and Hγ broadening but particular attention is given to Hα with spatially resolved

images. Cseh et al. (2017) endeavoured to characterise the cloud structure based on the Hα emission profile and Morozov et al. (2004) study the various positive ions that form in a carbon pellet-cloud system and includes radiative effects. This brief examination of the literature indicates that the possibility for ionisation to occur via electron-neutral collisions is at the very least a starting point for a pellet ablation model. The study of this electronic stopping has seen great interest since quantum mechanics made it possible to accurately model the atom with the continuous slowing down approximation and it continues to be a popular means of modelling particle interaction with matter.

3.1 The CSDA Model and the Bethe Formula

The continuous slowing down approximation (CSDA) assumes that charged particles continuously lose energy as they traverse a target medium at a rate determined exclusively by their current energy and the target material. The force the target exerts on the projectile particle is termed the *stopping power* or sometimes the *linear stopping power* and values are typically quoted in MeV cm^{-1} and is sometimes denoted by S. Because of the dependence of the target on the slowing of a projectile it is sometimes common to compare models and corrections to those models by the *mass stopping power* denoted here by S_M. Taken from Tolstikhina et al. (2018), the crucial quantity that easily scales the stopping power is the mass density, ρ, which relates the two stopping power quantities by

$$S_M = \frac{1}{\rho} S. \tag{3.1}$$

The CSDA has a relatively simple analytic form which can be readily used for a single particle interacting with a target. This has made it appealing to the nuclear energy industry as applied in Zieb et al. (2018) and Qi et al. (2019) and contemporary medicine as reported in Grimes et al. (2017) and Wohlfahrt et al. (2018) for which understanding the interaction of high-energy charged particles with solid matter is paramount. For those same reasons, among others, it will be used to develop this thesis. The stopping power formula used in this thesis will consider losses from particles to electrons bound in the atoms of the target. This makes it an inherently quantum mechanical process of which the derivation will be omitted but can be explored at the reader's leisure in Sigmund (2006). The Bethe formula was an early attempt to model the stopping of particles much more massive than electrons

in a medium and is presented in equation 3.2 as it is found in Martin (2009),

$$\frac{\mathrm{d}E}{\mathrm{d}x} = -\frac{\Omega q^2}{\beta^2} n_e \left(\ln\left(\frac{2m_e c^2 \beta^2 \gamma^2}{I} \right) - \beta^2 - \frac{\delta}{2} \right). \tag{3.2}$$

The terms in equation 3.2 (taken from Martin (2009)) are defined as follows: E is the particle kinetic energy in MeV, x is the particle coordinate in cm, q is the projectile charge in units of the elementary charge, β is the ratio of projectile speed v to the speed of light c, n_e is the electron density in cm^{-3} of the target, m_e is the electron mass, γ is the Lorentz factor, I is the mean excitation energy of the target medium and δ is a correction term for highly relativistic particles that accounts for dielectric effects in the target. This leaves the Ω term that is a constant defined as

$$\begin{aligned} \Omega &= \frac{4\pi\alpha^2\hbar^2}{m_e}, \\ &\approx 5.1 \times 10^{-25} \mathrm{MeV\ cm}^2, \end{aligned}$$

for a fine structure constant $\alpha \approx 1/137$ and a reduced Planck constant $\hbar = 6.582 \times 10^{-22}$MeVs. The electron density n_e can be rewritten in terms of the material density of the target to make the dependance on the target material properties clearer,

$$n_e = \mathcal{N} \rho \frac{Z}{A}. \tag{3.3}$$

In the above equation $\mathcal{N} = 6.022 \times 10^{23}$ is Avogadro's number, ρ, is the material density in cm^{-3}, Z is the atomic number of the target and A is the mass number of the target.
In the low energy limit a number of simplifications can be made to equation 3.2. For $v \ll c, \beta \approx 0$ and $\gamma \approx 1$. The high-energy dielectric correction δ can be neglected also. This allows for the non-relativistic version of 3.2 to be written as equation 3.4,

$$\frac{\mathrm{d}E}{\mathrm{d}x} = -\frac{\Omega q^2}{\beta^2} \mathcal{N} \rho \frac{Z}{A} \ln\left(\frac{2m_e v^2}{I} \right). \tag{3.4}$$

The quantity I is unique to each target material as it captures all the atomic data through an averaging process such that over many collisions an average energy loss per collision may be applied to achieve an approximate calculation of the energy lost over some distance.

The energy loss mechanisms covered by this averaging process include electronic excitation and ionisation. For more details on the calculation of the mean excitation energy the reader is encouraged to consult a text such as Sigmund (2006).
Particular arrangements of scaling constants and the choice of units can alter the presentation of the equation but ultimately it reduces to a scaling law,

$$S = \frac{\rho}{E}\kappa B(E), \tag{3.5}$$

where κ is the accumulated constants that embody the quantum nature of the mechanisms and $B(E)$ is some non-dimensional number that varies with the energy termed the *stopping number*. In Sigmund (2006) it is denoted by an L where it is shown to collect the competing processes that apply corrections to an initially simple result that increases linearly with mass density and decreases with increasing energy allowing for some competition between the high-energy dominant logarithm term and the low-energy dominant denominator.
This formula and its corrections were developed to describe the interaction of heavy ions with a neutral target. However, for our system, prior studies (see Parks and Turnbull (1977); Pégourié et al. (2005); Samulyak et al. (2007)) have indicated that electrons are likely to be the species interacting with the neutrals in this way. In fact, a brief calculation of the stopping power of deuterium gas at a density of $8.6\times10^{-5}\mathrm{g\,cm^{-3}}$ on a 10keV proton with $\beta \approx 4.62\times10^{-3}$ would show that the stopping power for protons is large enough to stop protons almost immediately

$$\begin{aligned}\frac{\mathrm{d}E}{\mathrm{d}x} &= -\frac{5.1\times10^{-25}\times1^2}{2.13\times10^{-5}}\times6.022\times10^{23}\times0.086\times10^{-3}\times\frac{1}{2}\times\ln\left(1.09\right),\\ \frac{\mathrm{d}E}{\mathrm{d}x} &= -53.4\mathrm{keVcm^{-1}}.\end{aligned} \tag{3.6}$$

This result is supported by examining a separate result from PSTAR calculations from Berger et al. (1999). The turning point at ~0.1MeV proton energy indicates an additional process is accounted for but the stopping is still strong enough to discount the flow of background ions towards the pellet. This calculation highlights the need to model the electron transport and energy losses in the cloud and neglect the small flow of ions from the background plasma through the cloud. A similar database to PSTAR exists for electrons known as ESTAR also taken from Berger et al. (1999). From that database a similar calculation can be carried out which preserves the v^{-2} shape and a lower mass stopping power. Looking at those results it is clear that electrons possibly could cross the cloud

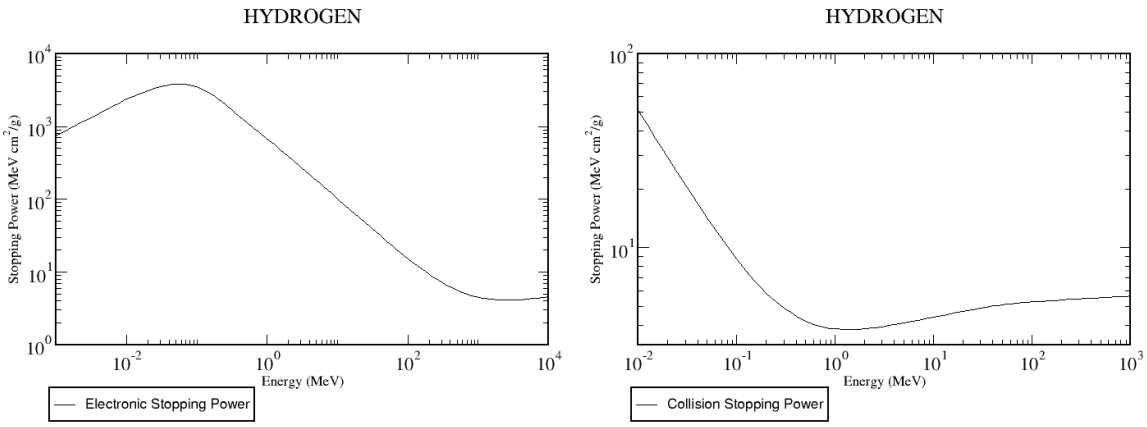

Figure 3.1: Left: The stopping power in MeV cm^2 g^{-1} of protons in a hydrogen gas. Right: The stopping power in MeV cm^2 g^{-1} of electrons in a hydrogen gas taken. Both figures are taken from results procured from Berger et al. (1999).

with sufficient energy. It is now appropriate to find a Bethe-type calculation suited to electrons to model their stopping.

3.1.1 A Bethe Formula for Electrons

One such variant of the Bethe stopping power theory for electrons has been devised bearing some similarity but incorporating additional terms Seltzer and Berger (1984). These are given in equations 3.7 - 3.9,

$$-\frac{\mathrm{d}E}{\mathrm{d}x} = \rho\frac{c_1}{\beta^2}\frac{Z}{A}B(T), \tag{3.7}$$

$$B(T) = B_0(T) - 2\ln\left(\frac{I}{m_e c^2}\right) - \delta, \tag{3.8}$$

$$B_0(T) = \ln\left(\frac{\tau^2(\tau+2)}{2}\right) + \frac{1}{(\tau+1)^2}\left(1+\frac{\tau^2}{8} - (2\tau+1)\ln 2\right). \tag{3.9}$$

The variables in equations 3.7 - 3.9 take their usual meanings or are defined by the following convention in cgs units: Z is the atomic number, A is the mass number of the target, $B(T)$ is the stopping number as a function of the electron kinetic energy T, I is the mean excitation energy, δ is a density-correction term to be discussed later and τ is the electron kinetic energy normalised to the electron rest mass energy $m_e c^2$. The c_1 term is a constant equal to 0.15356MeV cm^2 g^{-1}

The stopping number is a dimensionless number that captures more detailed physics as a measure of the logarithm of ratio of the maximum and minimum energy transfer during a collision. The stopping number is the term that is more accurately refined to gather the mathematical representation of various additional and competing processes in stopping particles depending on the energy. In particular, the indistinguishable nature of fermions means that it is impossible to identify the projectile electron from an electron ejected from the target and demands a more rigorous treatment. One such effect includes the shell-correction effect which incorporates the influence of the electronic configuration of atomic species with many electrons which is not expected to be an issue with a deuteriumc cloud. For more information one should consult Sigmund (2006). The density correction term, δ is needed to quantify the mitigation of stopping power due to the polarising of the medium in response to a passing charge. Seltzer and Berger present results from Sternheimer and Peierls theory that make it clear to the reader how to define the δ term with further details available in Sternheimer and Peierls (1971). For the kind of energies typical of a tokamak plasma, the system is comfortably in the low energy limit and consequently $\delta = 0$.
These expressions should now be evaluated for a cloud of hydrogen molecules with an electron at $\sim 10\text{keV}$ at a mass density of $8.6 \times 10^{-5}\text{gcm}^{-3}$ and using a value of $I = 19.8\text{eV}$ as the mean excitation energy which corresponds to gaseous molecular hydrogen from Seltzer and Berger (1982). The chosen density is approximately one thousandth of the solid state density and falls within the expected values for this system. The calculation proceeds as;

$$
\begin{aligned}
-\frac{\mathrm{d}E}{\mathrm{d}x} &= \rho\frac{c_1}{\beta^2}\frac{Z}{A}B(T), \\
&= \rho\frac{c_1}{\tau}\frac{Z}{A}B(T) \quad \text{because } \beta^2 = \frac{m_e v^2}{m_e c^2} = \tau, \\
&= 8.6 \times 10^{-5}\text{gcm}^{-3} \times \frac{0.15356\text{MeVcm}^2\text{g}^{-1}}{\sim 9.785 \times 10^{-3}}\frac{1}{2}B(T), \\
&\approx 3.302 \times 10^{-4} \times B(T)\text{MeVcm}^{-1}; \\
B(T) &= B_0(T) - 2\ln\left(\frac{I}{m_e c^2}\right) - \delta, \\
&\approx -5.209 - 2\ln\left(\frac{22.3\text{eV}}{\sim 511003\text{eV}}\right) - 0, \\
&= 14.99; \\
\implies -\frac{\mathrm{d}E}{\mathrm{d}x} &\approx 4.95\text{keVcm}^{-1}.
\end{aligned}
$$

So over ~ 2cm the 10keV electron should stop provided the density remains constant. This makes it a reasonable candidate to model the energy loss of electrons across a chord of the cloud but it is expected that the cloud density will vary with r and as the energy of the electron is lost the value of $\frac{\mathrm{d}E}{\mathrm{d}x}$ will vary too. This dependence is shown in figure 3.2 for a variation of a few orders of magnitude in density and electron energy. The dependence on density is obvious from equation 3.7 and easily deduced from figure 3.2. A simple scaling of the density is enough to arrive at the correct evaluation of the stopping power for a given energy, effectively just a linear dependance. The connection of electron energy to this evaluation is more complicated and is more easily understood by examining figure 3.2. The colourbar indicates that the greatest stopping power corresponds to the highest density (which is expected) and lowest energy which is apparent from looking at equation 3.7 which demonstrates the $1/E$ nature of the stopping power. In fact, the transition from purple to red in the colour plot illustrates the $1/E$ nature of the stopping power but also how quickly the stopping power can increase at lower energies, particularly around 3keV. From figure 3.2 a typical stopping power for about 10keV electrons and a density of 1gcm^{-3} is about 10MeV cm^{-1} and closer to 100MeV cm^{-1} for 1keV electrons at the same density.

3.2 Suitability of CSDA

3.2.1 The Assumptions in the CSDA Model

Whilst the formula has been readily used it is essential to note some key assumptions in applying it.

1. The CSDA approach has been used most frequently for solid/liquid targets - Gümü and Kabadayi (2010), Deutsch (2019). The system in this thesis comprises of a deuterium gas target which is in contrast to these typical scenarios.

2. The typical energy range of the formula must be acknowledged. The Bethe formula is mainly used for high energy, in fact relativistic, particles thoroughly in the MeV energy range such as in Adey et al. (2019) and Cesar et al. (2015). This makes it a suitable choice in evaluating stopping of alpha particles and products of nuclear decay but is not conventionally applied to moderate energy electrons.

3. The formula is also entirely one-dimensional. To apply the formula to a system in which there is not a mono-directional flux of particles will require some justification.

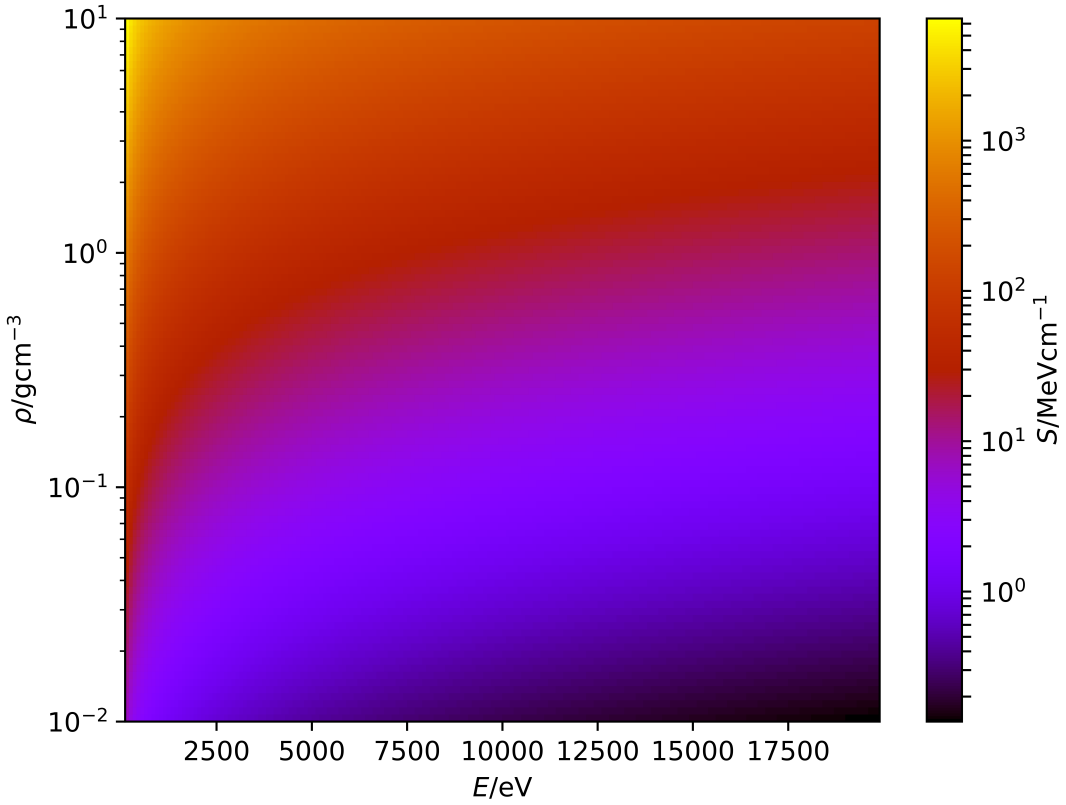

Figure 3.2: The formula outlined in equation 3.7 evaluated for electrons in deuterium for densities spanning 3 orders of magnitude and electron energies spanning 100eV to 20keV. Other parameters include $I = 22.3$eV and $\frac{Z}{A} = \frac{1}{2}$.

4. The CSDA considers a single projectile particle interacting with the target medium at any given time, i.e. a beam. Consequently, there should be no significant interaction between a series of projectile particles entering the target simultaneously and slowing should be dominated by electron-neutral interactions.

If the CSDA model is to be applied to our system then it must meet these criteria. The following list will explain the similarities in these systems and explain any discrepancies with a quantitative argument where possible.

1. Addressing the first term is relatively simple. The chemical makeup of the target plays a significant role in the effect of the CSDA through the $\frac{Z}{A}$ term and the mean

interaction energy term but the density can be freely chosen outwith these other two terms. It is therefore possible to select the density corresponding to the molecular hydrogen gas and not that corresponding to the solid state. Provided the interactions between the projectile and the target are dominant then it is acceptable to implement CSDA i.e. the density of neutrals is expected to be dominant. This is expected to be the case as the density contrast between the neutral cloud and background plasma is expected to be several orders of magnitude and even reviewing measurements from tokamaks will illustrate that this is the case supported by Pégourié et al. (2005) and Lengyel et al. (1991). The large density contrast at work here means that any particle entering the cloud will be dominated by its interactions with neutrals rather than by any interaction with other projectiles or the products of any interactions in the target. The density contrast used will be presented in the following chapter but is expected to be at least of the order 10^3 between the high density neutral cloud and the low density tokamak plasma.The application of this method to gases has been performed in published works such as Kazkaz et al. (2010) and Nguyen-Truong (2015)

One may also argue that because the target in this system is a gas that the neutral particles may move under their own thermal motion enough to break the natural order of any density profile. This is unlikely to be a problem because the lowest energy electrons will have a temperature $\sim$ order of magnitude greater than the neutrals. The particle speeds will then present an even larger difference due to the ratio of m_e to m_n. The distance covered by a neutral in the time taken for an electron to traverse the cloud is safely negligible.

2. The second assumption remarks upon the initial energy of the incoming particles. Whilst it is true that most applications of the CSDA have been in the high energy range, in order to assess where a particle has stopped it would have to descend through all the energies from its initial energy through to 0eV. These types of calculations are routinely performed and are documented in articles such as Grimes et al. (2017) and Han et al. (2016). For an MeV particle this would necessitate an evaluation at the keV range (and lower) unless the model incorporates a change to another model at these lower energies. This is regularly avoided or has a minimal influence on the stopping distance for particles so will be neglected in this instance instead opting to use the CSDA model for electronic stopping from the intial energy to the termination energy.

3. Issues regarding the efficacy of a one-dimensional model to describe a three-dimensional system can be easily addressed. The model developed for this thesis will be entirely one-dimensional but could potentially be expanded to a multi-dimensional model because the intense magnetic field strength of a tokamak along will restrict electron motion to within a Larmor radius of the gyrocentre. This greatly limits the motion of particles (to within $\sim 10^{-5}$m) which effectively collimates the flow and asserts a pseudo-one-dimensional environment making it significantly simpler to incorporate the one-dimensional CSDA into a pellet-ablation model. A similar approach was in fact taken by Houlberg and Attenberger (1988). One could argue that neglecting the effects of the additional spatial dimensions would be omitting significant additional loss mechanisms. For example, motion of electrons into the cloud perpendicular to the magnetic field is not likely because of the difference in scale between the Larmor radius and the size of the cloud. Similarly one may argue that radiative losses across the transverse direction could cause additional heating or ionisation which while possible is expected to be a a higher order effect than the initial impact by electrons along the field line. This does not rule out the possibility that more interesting phenomena may occur due to these higher order effects but is neglected in this elementary treatment of the problem and left for further bodies of work.

4. Queries surrounding the use of a single particle approach can be responded to by referring to the argument against the first issue. The density of neutrals is expected to thoroughly dominate the density of charges and consequently the most likely series of interactions will be between neutrals and electrons. This can be further supported by the short lifetimes of excited atomic states compared to the transit time of particles across the cloud. This will depend on the type of interaction and whether the cross-section for that collision offers a reasonable chance of it existing and then later interacting with more incident electrons. This can be supported by a review of the cross-sections for interactions between electrons and molecular hydrogen and the products of any reactions.

It is crucial to understand that this analysis of the $e^- - H_2$ collision cross-sections is not being used to develop a further correction to equation 3.7 but to better understand the relative importance of the reactions. All of these reactions are captured by the mean excitation energy in the development of the Bethe theory already. These cross-sections will bring a close to the argument that CSDA applied exclusively to molecular hydrogen

provides a strong enough approximation to the system.

3.3 $e^- - H_2$ Collisions

The cross-section for a particular collision acts as a probability of that interaction occuring. Analysis is not typically straight-forward where there are several competing reactions which demands a numerical treatment to solve the system of rate equations unique to the parameter set for the system. However, where certain interactions dominate, particularly for a given set of parameters, it becomes much easier to argue that an individual reaction is substantially more favourable to occur than others. The expected abundance of the products can be approximated and may justify certain assumptions about a simplification of the system to ignore possible but improbable reactions. This section aims to achieve this by making a case for the dominance of $e^- - H_2$ collisions within the system described by the previous chapter. This will be shown by illustrating the one key point that the products of the most important reactions is mainly H_2 and thus preserves the neutral population density in the cloud. Any other products of any other reactions therefore exist in much smaller proportions than the neutral density and any subsequent reactions with them are therefore negligible. To do this, a library of relevant collisions (shown below) and their cross-sections must be constructed and assessed to support the claim that neutral interactions dominate and to justify use of the CSDA.

$$e^- + H_2 \rightarrow 2e^- + H_2^+ \qquad \textit{Ionisation} \qquad (3.10)$$

$$e^- + H_2 \rightarrow e^- + H_2 \qquad \textit{Elastic Collision} \qquad (3.11)$$

$$e^- + H_2 \rightarrow e^- + H_2^* \qquad \textit{Excitation} \qquad (3.12)$$

$$e^- + H_2 \rightarrow e^- + H^{*n=3} + H \qquad \textit{Dissociative Excitation} \qquad (3.13)$$

$$e^- + H_2 \rightarrow H^- + H \qquad \textit{Dissociative Electron Attachment} \qquad (3.14)$$

$$e^- + H_2 \rightarrow e^- + H_2^{*rot} \qquad \textit{Rotational Excitation} \qquad (3.15)$$

$$e^- + H_2 \rightarrow e^- + H_2^{*vib} \qquad \textit{Vibrational Excitation} \qquad (3.16)$$

It is important to note a significance unique to equation 3.13 by way of a radiative signature, namely the Balmer α line at ~ 656nm. As has been presented in the previous chapter, this is a significant diagnostic for pellet injection experiments.

3.3.1 Cross-sections

The cross-sections for the reactions in equations 3.10 to 3.15 need to be examined to determine which interactions are most probable to occur. Online resources such as LXCat and the contained databases (Biagi, IST-Lisbon, Phelps, Triniti) have been consulted to gather the cross-section data and judge the relative importance of reactions. All the reagents present in the above reactions will be discussed in turn. It is clear from looking at figure 3.3 that the effective cross section (line 3) has the largest cross section across the entire range of energies. The effective cross-section is dominated by elastic interactions at energies less than 1 eV and dominated by elastic collisions with a contribution from some atomic excitation and rotational interactions from equations 3.12 and 3.15. For electron energies greater than ~ 10 eV, the key interaction that contributes to the overall cross-section comes from ionisation by means of equation 3.10. Some additional contributions come from certain excitation interactions but ionisation is still the dominant interaction. It is also clear that attachment processes (lines 1 and 13) are completely overhwelmed by the other ongoing interactions and can be safely neglected. Therefore, it can be safely assumed that H_2^+ is unlikely to recombine with an electron to form neutral hydrogen again. More simply put: once molecular hydrogen is ionised, it will remain ionised. Consequently, this acts as a source for positive ions and electrons within the cloud. The produced ions may later contribute to the ablation of neutrals from the surface of the pellet if they are accelerated by the local electric field. This will discussed in more details at the end of this chapter. Low energy rotational excitations may contribute substantially to the total inelastic scattering cross-section but the energies at which they are significant are comfortably below the mean exitation energy in the Seltzer and Berger formula. This means that rotational excitations can be safely neglected as an energy loss mechanism for electrons within the energy range of interest. The dominating reactions here are fundamentally the ionisation and excitation reactions characterised by equations 3.10 and 3.12. The ionised products exist in such short proportions such as not to be important. In addition to this, the pellet is continually ejecting fresh neutral material to populate the cloud. This only acts to dilute further the ionised fraction in the cloud at later times and preserve the neutral dominance in the cloud particularly in the region closest to the pellet that is already the most dense with neutrals and therefore the most effective at stopping particles. The outer region (nearest the plasma) will suffer the brunt of the electron energy as it is closest to the plasma and may become significantly ionised but it is likely to be the least dense and CSDA will be less than influential here than closer to the pellet where the

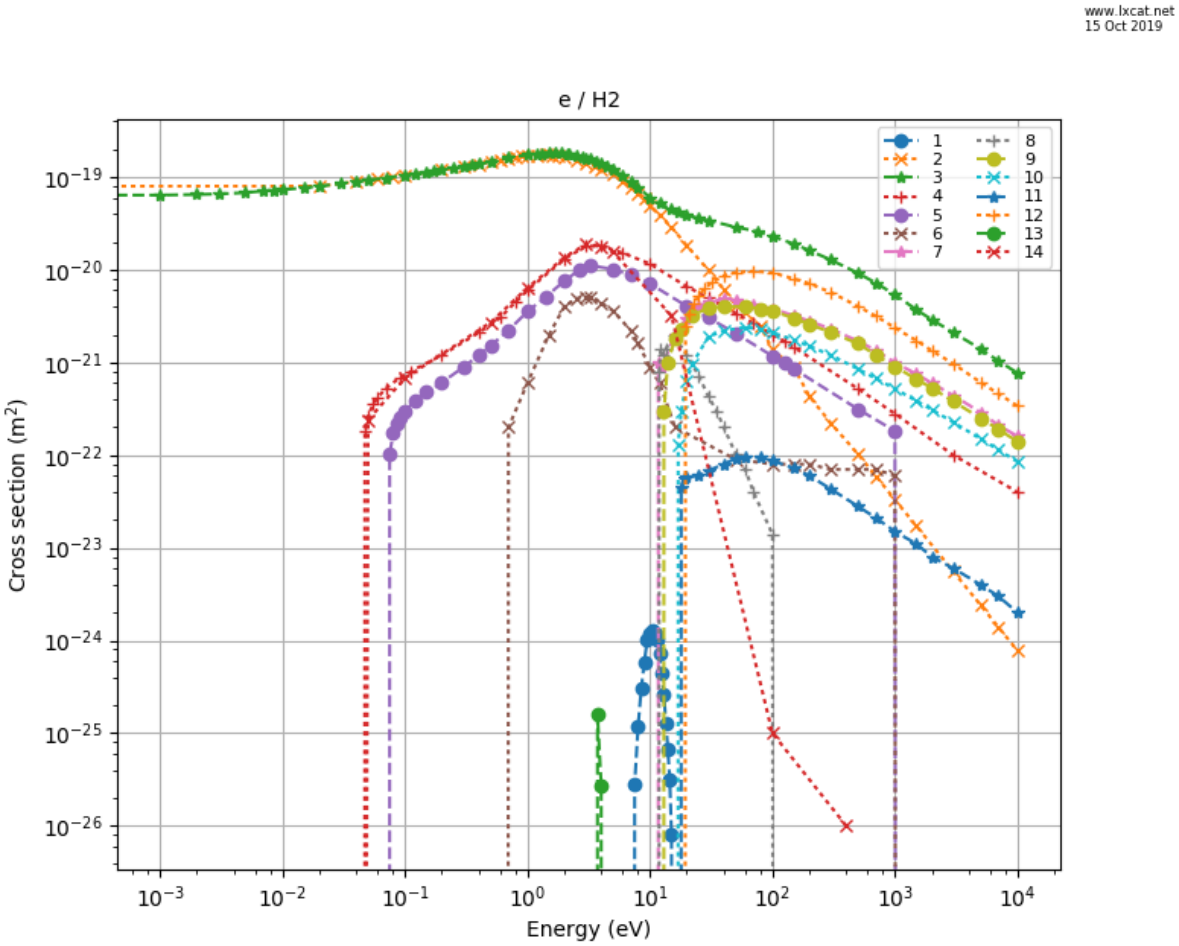

Figure 3.3: The most significant cross-sections for electron and molecular hydrogen collisions from a few meV to a keV. Lines 1 and 13 correspond to attachment reactions with excitation energies 7 and 3.6 eV from Biagi and Triniti respectively (equation 3.14), line 2 presents the elastic cross section from IST-Lisbon (equation 3.11), line 3 presents the effective cross-section with no new species created during the process from Phelps, lines 4 to 10 show excitation cross-sections for several excitation energies between 0.044 to 15.2eV from Phelps (equation 3.12), dissociative excitation is shown in line 11 for 16.6eV interaction energy from Phelps (equation 3.13), line 12 shows the ionisation cross section from Phelps (equation 3.10) and cross-sections for rotational excitation shown in line 14 from Triniti (equation 3.15).

density is greater. This idea has already been applied in various solutions to the ablation problem such as in Parks and Turnbull (1977) and Milora and Foster (1978)

This pre-existing data supports the argument that CSDA can be comfortably applied in this situation. Initially all large particles are neutral molecular hydrogen. The predominant

cross-sections in the energy range relevant to this problem are the ionising and excitation cross-sections. These reactions either produce a molecular hydrogen cation through the ionisation reaction or a short-lived electronically excited state of H_2. These electronically excited states are short-lived and quickly return to the ground state, although they are ultimately neutral H_2 which is an inherent assumption of the model. The ionising reactions, however, have new products including a positive ion and an additional low energy electron. If it is a given that a particle will collide then the probability that an ionising reaction is the one that occurs is given by the ratio of the ionisation reaction cross-section to the total cross-section of an electron reacting with diatomic hydrogen. The density of ions produced is then determined by the likelihood of that reaction occuring given a reaction does occur multiplied by the limiting density which in this case is the electron density,

$$n_+ = \left(\frac{\sigma_+}{\sigma_T}\right) n_{H_2}. \tag{3.17}$$

This equation assumes that an electron only undergoes one collision with a neutral which is not true. However, if it is assumed that any excited neutrals quickly return to the ground state and that if a neutral is ionised or dissociated the significantly lower electron density will not drastically affect the assumption that electrons exclusively interact with neutrals. It is important to note that this relation also lowers the population of neutrals and increases the electron population by this amount. The particles released will be of low energy and remain practically immobile after the collision save for their random-walk diffusive motion.

This positive ion is now produced within the cloud and possibly much closer to the pellet than any of the background ions could have reached because of the excessively high stopping power. It is therefore possible that ions *could* ablate some material to supplement the electron ablation if they can be transported from their position in the cloud towards the pellet. This may happen through two possible mechanisms: diffusion or acceleration via the sheath field which will have competing effects on the charged particles in the cloud that influence their transport. This will be elaborated upon in drift-diffusion model to be discussed in chapter 5.

Another potential concern for our system and the available data is the abundance of parameters for hydrogen and the absence of those for deuterium. This isn't expected to present inaccuracies in the results because isotopes influence nuclear reactions (which is why deuterium is selected for this nuclear reactor) and not the electronic transitions within

an atom. It is because of this that hydrogen data will be applied to our deuterium system with little consequence expected.

3.4 Conclusion

This chapter has introduced the CSDA as a means to study the rate at which electrons would lose energy by traversing through a gaseous target. The approximation is introduced initially in the form of the Bethe formula before illustrating that heavy particles such as ions could not possibly penetrate the cloud from the background plasma. Seltzer and Berger (1982) presents a form of the Bethe stopping formula for electrons that is suitable for the problem at hand and will be used in subsequent chapters to model the stopping of electrons. Any concern over the suitability of the CSDA for the pellet problem is discussed with key concerns such as the use of a gaseous target over a traditionally solid one and the availability of data for molecular deuterium. This preliminary discussion has established the context that this thesis will now explore in greater detail by developing a model to describe the ablation and incorporating it into a computer simulation that iterates over a portion of the life of the pellet. The ensuing dynamics and the connection between subsequent equilibrium states will be modelled through the CSDA. The first step to overcome this challenge is to develop an analytical form for the equilibrium states by comparing to an already established model. This is accomplished in the following chapter.

Chapter 4

The Evaporative Model

The process of ablating cryogenic pellets in tokamaks has been previously dubbed as evaporation in the literature Dunne et al. (2016), Garzotti et al. (2012), Milora et al. (1995), Combs (1993). While the transition of matter from the solid state to the gaseous state is formally defined as sublimation, the physics at work is not dissimilar: energy is injected into the system to such an extent that the bound particles have enough energy to break from their inter-molecular bonds. The rate at which the energy is delivered will then in turn determine the rate of lost material and this rate is essential to determining every other physical quantity in the vapour cloud. This has been the approach taken by Parks and Turnbull (1977) in the dominant work of this field through the neutral gas shielding model (NGS). The authors propose that electrons perform all ablation and quantify this by considering the energy flux delivered to the pellet and the local heating releasing molecules from the pellet. These calculations then predict the evolution of the pellet's size in time by defining the differential flux on the pellet analytically. The model predicts the lifetime of a pellet in a tokamak plasma for various densities and temperatures but does not determine macroscopic quantities such as the cloud size. Fundamentally, the NGS model calculates the pellet and cloud parameters by calculating the form of the ablation rate through thermodynamic arguments. However, the model enclosed in this chapter *assumes* the form of the ablation rate by likening it to an established law in evaporation physics and calculating the physical parameters - and eventually the ablation rate - by assuming a form of this rate initially. The aim of this chapter is to demonstrate that a simple "toy" model can achieve approximate success by accepting that the physics of ablation and evaporation are similar.

4.1 Foundations of the Model

4.1.1 The "D^2" law

The comparisons between ablation and evaporation drawn already has prompted the question: can the ablation of the solid pellet be modelled using some evaporative process? If so, is there a simple analytical form to carry out further mathematical analysis to study the physical properties of the system? Aerosol studies have presented an empirical law to describe the evaporation of macroscopic droplets (defined to be larger than 1μm) in air. The essential point of this law is that the surface area of a droplet immersed in some atmosphere decreases constantly in time. Within this law the $\dot{A}$ term strictly relates the to the rate at which the area of the droplet changes but can be used as a proxy for the ablation rate. In mathematical terms $\dot{A}$ is proportional to some constant, k which has given it the name the "D^2" law, for the diameter of the droplet, D as in Cazabat and Guéna (2010). The system in chapter 2 meets the criteria for size and can not be described as being under vacuum conditions with the flux of energetic particles towards the pellet presenting a substantial input of energy. Modifications to the "D^2" law allow for calculations on the pellet size, r_p, the cloud size, r_c, and the neutral density, ρ, by comparing the ablation process to evaporation.

Now that the foundations of the model have been formulated the "D^2" law and its modifications for pellet ablation may be explored further. A mathematical formulation of the "D^2" law looks as in equation 4.1 but can be integrated to yield an equation for A.

$$\dot{A} = -k, \tag{4.1}$$

$$A = -kt + c, \qquad \text{but at } t = 0,\ A = A_0 \implies c = A_0$$

$$A = A_0(1 - k't) \qquad \text{for } k' = \frac{k}{A_0},$$

Now, at $t = t_f, A = 0$

$$\therefore \qquad 0 = A_0(1 - k't_f),$$

$$\text{So} \qquad k' = \frac{1}{t_f},$$

$$A = A_0\left(1 - \frac{t}{t_f}\right). \tag{4.2}$$

Substitution of radius for the surface area term in equation 4.2 yields

$$r_p = r_0\left(1-\frac{t}{t_f}\right)^{\frac{1}{2}}. \tag{4.3}$$

If equation 4.3 is differentiated to get the recession speed of the pellet's surface, a significant issue is revealed. Inspecting equation 4.2 shows that if t tends to t_f, then the recession speed of the surface tends to infinity which is not physical. An alternative ablation rate is required to eliminate this problem.

$$\begin{aligned} r_p &= r_0 k_1\left(1-\frac{t}{t_f}\right)^{\frac{1}{2}}, \\ \dot{r}_p &= -\frac{1}{2}\frac{r_0}{t_f}k_1\left(1-\frac{t}{t_f}\right)^{-\frac{1}{2}} \end{aligned} \tag{4.4}$$

To maintain some consistency with the "D^2" law, this modified ablation rate should have an approximately constant behaviour to mimic the "D^2" law and should then tend to zero at later times which would remove the problem of an infinite recession speed. One function that has been explored is the hyperbolic tangent function, $\tanh(x)$ where $x = k_2\left(1-\frac{t}{t_f}\right)$. The reason for this modification can be seen in figure 4.1. The "D^2" law maintains a constant ablation rate over the lifetime of the pellet and fundamentally results in an infinite surface recession speed as the pellet gets smaller. What is therefore desirable is an ablation rate which ultimately decreases as the pellet gets smaller but maintains a consistency with the established D^2 law. Figure 4.1 illustrates this with a choice of the parameter k_2 to match the constant ablation rate and, with some freedom, return to zero - which is the needed behaviour. The hyperbolic tangent function preserves the behaviour characteristic of the "D^2" law but prevent the mathematical collapse inherent in the square root function. This amendment is a new piece of work that has not been recorded in the published literature as the "D^2" law is befitting of most instances or is used to support an alternative approach Aguilar et al. (2001),Yu et al. (2017). The same approach that was taken to determine r_p and $\dot{r}_p$ can be taken again with $\tanh\left(k_2(1-\frac{t}{t_f})\right)$ to evaluate a new pellet radius and recession speed, equations 4.9 and 4.10 respectively.

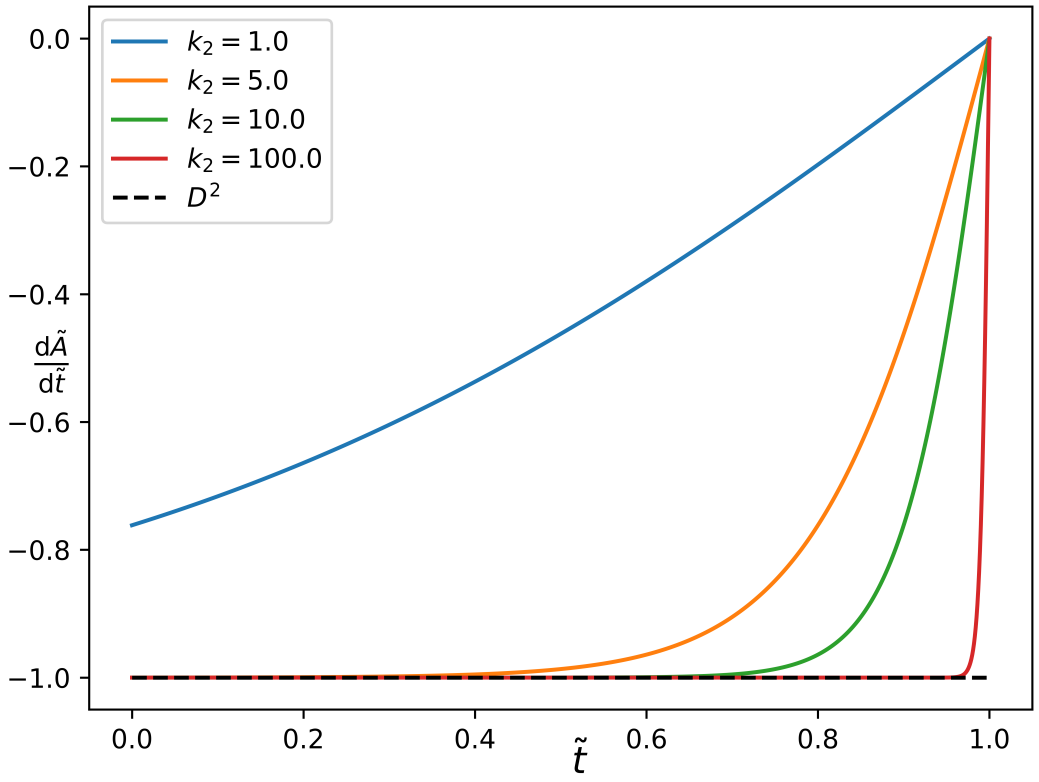

Figure 4.1: The ablation rate prescribed by equation 4.5 for several choices of k_2 and $k = 1.0$ with the "D^2" law ablation rate (dashed line).

$$\frac{\mathrm{d}A}{\mathrm{d}t} = -k\tanh\left(k_2\left(1-\frac{t}{t_f}\right)\right), \tag{4.5}$$

$$\int \mathrm{d}A = -k\int \tanh\left(k_2\left(1-\frac{t}{t_f}\right)\right)\mathrm{d}t,$$

$$A = \frac{t_f k}{k_2}\ln\left(\cosh\left(k_2\left(1-\frac{t}{t_f}\right)\right)\right) + c, \tag{4.6}$$

where c is some constant and k_2 is some positive constant. From equation 4.6 we can insert two separate boundary conditions.

1. At $t = 0$, $A = A_0$ - no ablation has been performed yet and the pellet is at its initial size.

2. At $t = t_f$, $A = 0$ - the pellet is at the end of its life and has been fully ablated

Evaluating each conditions separately will yield two equations describing the behaviour at opposite ends of the pellet's life. The first condition can be used in equation 4.6 to show that $c = 0$. The second can be used in this result directly to relate A_0 to the other system parameters as

$$A_0 = \frac{t_f k}{k_2} \ln\Big(\cosh\big(k_2\big)\Big). \tag{4.7}$$

Rearranging for $-\frac{t_f k}{k_2}$ and inserting into equation 4.6 with $c = 0$ returns

$$A = A_0 \frac{\ln\left(\cosh\left(k_2\left(1 - \frac{t}{t_f}\right)\right)\right)}{\ln\left(\cosh\left(k_2\right)\right)}, \tag{4.8}$$

$$\frac{r_p}{r_0} = \sqrt{\frac{\ln\left(\cosh\left(k_2\left(1 - \frac{t}{t_f}\right)\right)\right)}{\ln\left(\cosh\left(k_2\right)\right)}}. \tag{4.9}$$

Examples of these functions for r_p for different (normalised) parameter regimes are given in figure 4.2. The ablation rate itself dictates the value of t_f and the ablation rate is being changed through choices of k_2. Consequently, each line in figure 4.2 is normalised to a different t_f. That t_f is not known but is not of immediate importance at this time. Differentiating again as was done with equation 4.3 achieves a different result which does not tend to infinity as t goes to t_f. In this case, the pellet recession speed tends to a finite value as t tends to t_f which is a more satisfying result. Again, examples of these recession

speeds are presented in figure 4.3.

$$
\begin{aligned}
r_p &= r_0 \frac{1}{\sqrt{\ln\left(\cosh\left(k_2\right)\right)}} \left[\ln\left(\cosh\left(k_2\left(1-\frac{t}{t_f}\right)\right)\right)\right]^{\frac{1}{2}}, \\
\dot{r}_p &= r_0 \frac{1}{\sqrt{\ln\left(\cosh\left(k_2\right)\right)}} \left[\ln\left(\cosh\left(k_2\left(1-\frac{t}{t_f}\right)\right)\right)\right]^{-\frac{1}{2}} \left(-\frac{k_2}{2t_f}\right) \tanh\left(k_2\left(1-\frac{t}{t_f}\right)\right), \\
\dot{r}_p &= -\frac{r_0 k_2}{2t_f} \frac{1}{\sqrt{\ln\left(\cosh\left(k_2\right)\right)}} \frac{\tanh\left(k_2\left(1-\frac{t}{t_f}\right)\right)}{\sqrt{\ln\left(\cosh\left(k_2\left(1-\frac{t}{t_f}\right)\right)\right)}}.
\end{aligned} \tag{4.10}
$$

It can be seen from figure 4.3 that the $\dot{r}_p$ term remains finite as $t \to t_f$. Further proof of this can be found in figure 4.4 in which, for the same parameters, the acceleration of the pellet surface, $\ddot{r}_p$, can be much more clearly seen to go to zero at later times. The line corresponding to $k_2 = 100$ does not reach zero for the resolution selected but is tending towards following the same trend as the other lines.

4.1.2 Assumptions for the Model

The "D^2" law acts as an analytical starting point for our evaporative model but a number of other assumptions must be accounted for:

1. The process is spherically symmetric with the origin of the coordinate system at the centre of the pellet.

2. The expansion speed of the cloud $\dot{r}$ is much slower than the speed of any particles in the plasma, v_s. This is the *quasi-static* assumption.

3. Mass is conserved in the system. The pellet-cloud system exists in a vacuum with no mass lost to any background matter.

4. Evaporation physics is accepted as the underlying process and the "D^2" law will act as a mathematical basis for further work.

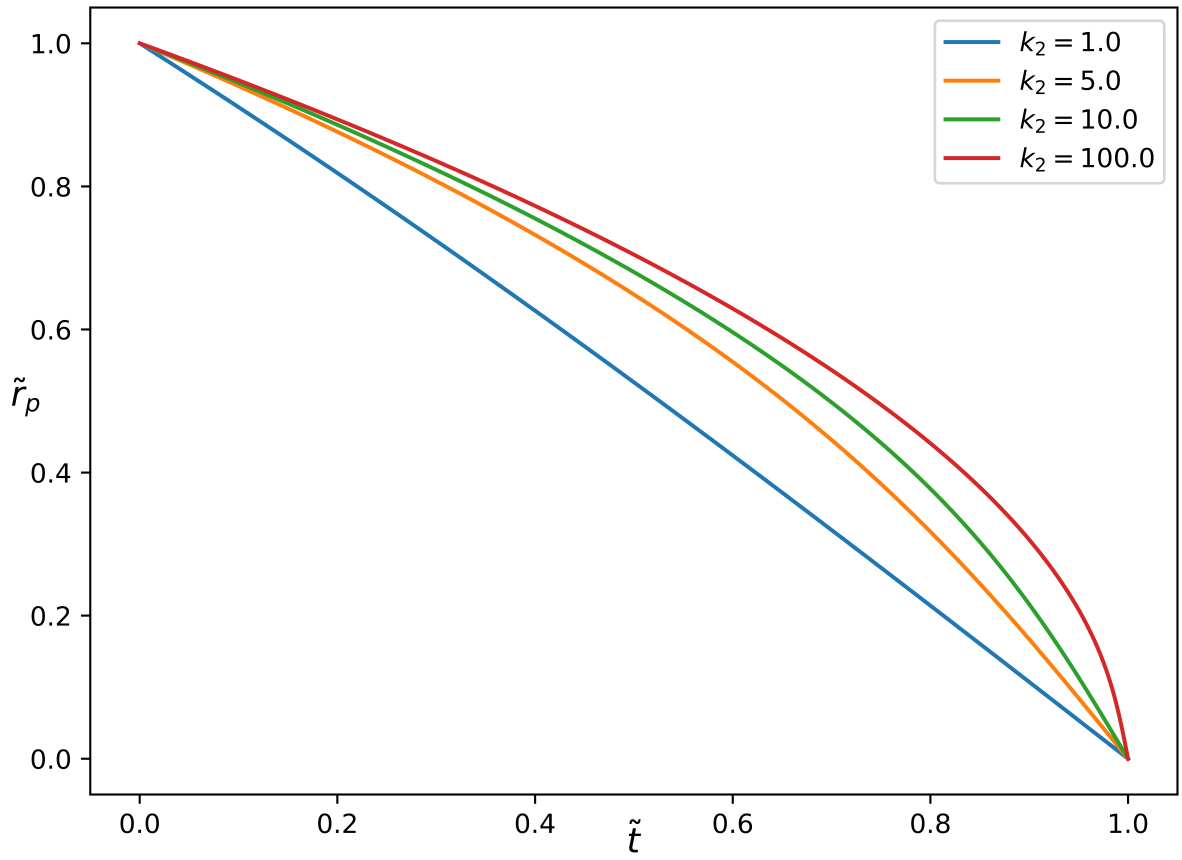

Figure 4.2: The evolution of the normalised pellet radius $\tilde{r}_p$ in time for various choices of parameter k_2. In each case, $\tilde{r}_p$ starts at a value of 1.0 and stops at 0.0 which is as expected but k_2 controls the rate at which the pellet reaches those values. Greater ablation rates, associated with a lower k_2, hasten the rate at which the pellet loses mass.

5. The density profile of the cloud will take a prescribed format that has been selected to be consistent with observations.

I will now justify these assumptions in turn.

1. The symmetry of a sphere makes for a convenient geometry to start with and while observed clouds are elongated along the axis, that has been attributed to ionisation within the cloud and the subsequent alignment of material with the magnetic axis. At this stage in the argument, a spherical geometry will be studied and the possibility of other geometries (spheroidal, ellipsoidal etc) will be demonstrated at a later point.

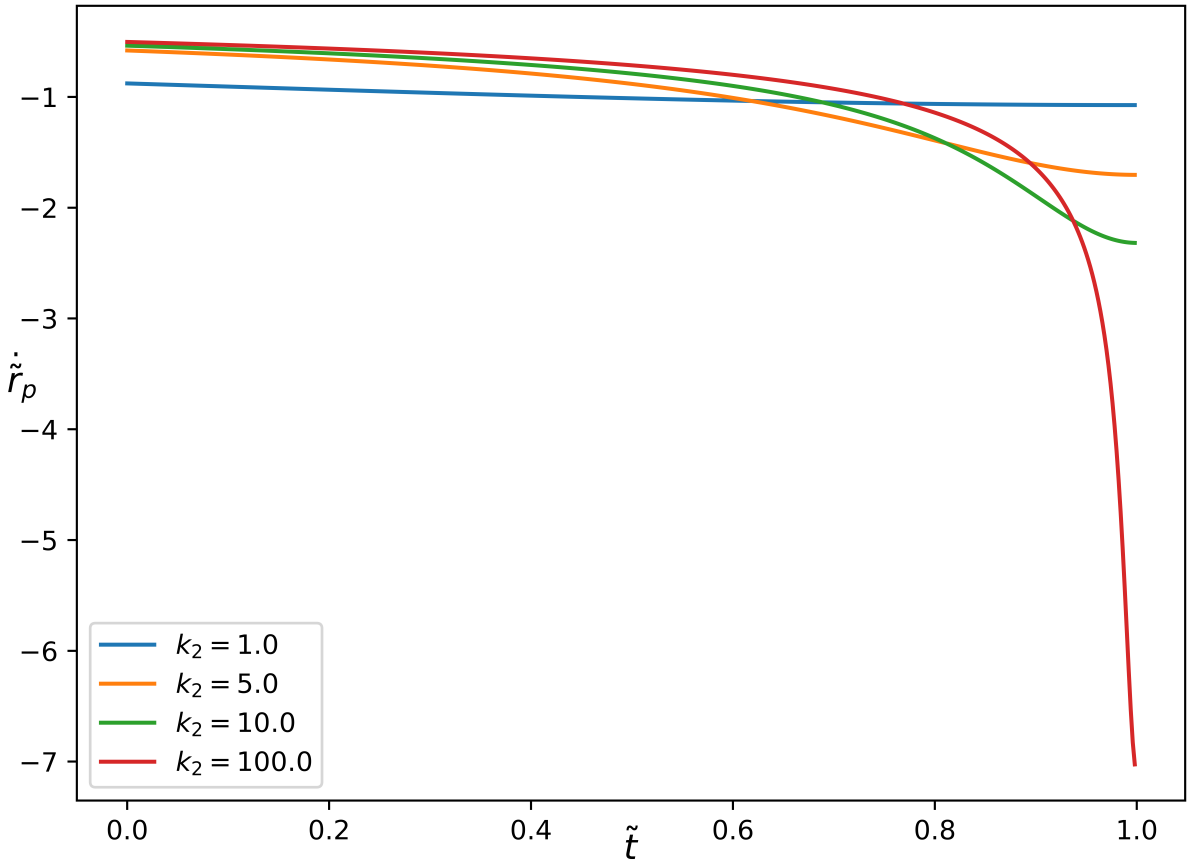

Figure 4.3: Plots of $\dot{\tilde{r}}_p$ against $\tilde{t}$ for a range of values of k_2. When considered in tandem with figure 4.4 in which the acceleration of r_p tends to zero then it is seen that $\dot{r}_p$ remains finite which is more physically sound than an infinite recession speed.

2. Quasi-static assumptions have been made in other works and it should be expected that the majority of electrons in the 10keV plasma will be moving many orders of magnitude faster than the pellet. Therefore it is expected that a significant change in the system will be observed by the particles long before any significant change is observed in the fluid limit.

3. Conservation of mass is essential and, in fact, is the conservation law that will be used to evaluate all derived quantities in this analysis. By assuming that the cloud expands into a vacuum this is easier to manage and the vastly differing densities of background and cloud media and their constituent particles mean that any contribution to the pellet-cloud system by background plasma particles should be negligible.

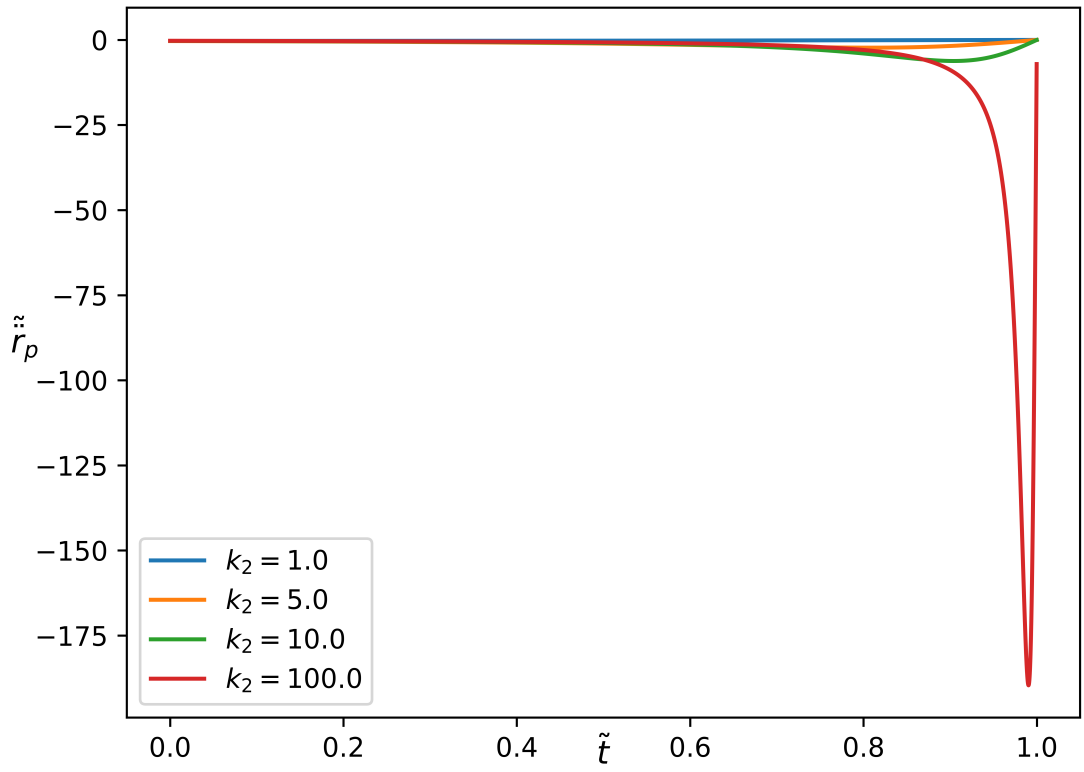

Figure 4.4: The acceleration of the pellet surface with time for the common choices of k_2, clearly tending to zero.

4. The "D^2" law has been studied with regards to droplets evaporating in an atmosphere which is a physical environment bearing many similarities to the pellet problem. The droplet is freely floating in space and evaporates due to interaction with the ambient gases which is in line with the quasi-static assumption (such that the pellet is not moving significantly) and the background plasma performs the ablation. It is therefore implicitly assumed here that the pellet ablates according to evaporation physis.

5. The density profile is a quantity of which we assume the functional form and prescribe one boundary value and allow the other to vary as the cloud expands. The density follows a r^{-2} law in accordance with statements made in Parks and Turnbull (1977) that declare the density should fall off "at least as $\frac{1}{r^2}$" which is in line with typical

spherically symmetric systems. Consequently, the profile that has been selected is given in equation 4.11 where r_p is the instantaneous pellet radius, r_0 is the initial pellet radius, r is the cloud coordinate and ρ_p is the solid-state pellet density,

$$\rho_c = \rho_p \frac{r_0^2 + r_p^2}{r_0^2 + r^2}. \tag{4.11}$$

However, the change in state from solid to gas will be accompanied by a density contrast, ϵ, which scales the density of the cloud at the pellet's surface. The value of ϵ is informed by evaporation and ablation experiments (as in Zhakhovsky et al. (2018)) to be 10^{-2} and the corrected profile is given by equation 4.12,

$$\rho_c = \epsilon\rho_p \frac{r_0^2 + r_p^2}{r_0^2 + r^2}. \tag{4.12}$$

This profile has been selected with a number of physical constraints in mind.

1. At time $t = t_f$, the centre of the cloud ($r = 0$) should have a non-zero density.

2. At time $t = t_f$, the density profile should no longer be evolving in time, $\dot{\rho}_c(r,t) = 0$

3. At any time, the cloud density must be greater than zero everywhere: $\rho_c(r,t) > 0$ for $r \in [r_p, r_c]$.

We can show that each of these criteria are met with the profile given in equation 4.12.

1. At time $t = t_f$, $r_p = 0$ and at the centre of the cloud $r = 0$,

$$\begin{aligned} \rho_c(0,t_f) &= \epsilon\rho_p \frac{r_0^2 + 0}{r_0^2}, \\ &= \epsilon\rho_p. \end{aligned} \tag{4.13}$$

   which is a non-zero, positive number.

2. The requirement that the time derivative of the density profile at any arbitrary point

and time r and t can be easily evaluated,

$$\begin{aligned}\dot{\rho}_c(r,t) &= \frac{\mathrm{d}}{\mathrm{d}t}\left(\epsilon\rho_p\frac{r_0^2+r_p^2}{r_0^2+r^2}\right),\\ &= \epsilon\rho_p\frac{\mathrm{d}}{\mathrm{d}t}\left(\frac{r_0^2+r_p^2}{r_0^2+r^2}\right),\\ &= \epsilon\rho_p\frac{2r_p\dot{r}_p}{r_0^2+r^2}.\end{aligned} \tag{4.14}$$

Given that the ablation rate we selected in equation 4.5 goes to zero as r_p goes to 0, the desired result immediately follows.

3. This final property is easily satisfied by this choice of profile. The fraction term consists of squared, real numbers which are always positive. These terms are only ever summed meaning that the fraction is positive definite. Moreover, the coefficient to the fraction is also a positive, real number and so the function $\rho_c(r,t)$ is positive definite.

4.2 Developing the Model

At this stage the physics of the problem can now be explored. One of the assumptions of this model was the overall conservation of mass between two different media: the cloud and the pellet. This will be used by integrating the cloud density over the geometry of the cloud, which at all times should equal the mass lost by the pellet. To do this will require some information on the size of the cloud, r_c, but before that is calculated, let's first examine the conservation of mass,

$$\frac{4\pi}{3}\rho_p r_0^3 = 4\pi\rho_p r_p^3 + \frac{4\pi}{3}\int_{r_p}^{r_c}\rho_c(r,t)r^2\mathrm{d}r. \tag{4.15}$$

It is challenging to solve for r_c from this equation. Instead the rate at which mass changes state is a more helpful quantity to conserve. This is effectively achieved by differentiating equation 4.15 with respect to time and equates the mass lost by the pellet in a unit of time to the amount gained by the cloud in that same unit of time. This may be expressed as in equation 4.16.

$$-\dot{M}_p = \dot{M}_c, \tag{4.16}$$

$$-\rho_p r_p^2 \dot{r}_p = \frac{\mathrm{d}}{\mathrm{d}t}\int_{r_p}^{r_c} \rho_c(r,t) r^2 \mathrm{d}r. \tag{4.17}$$

On the right hand side it has now become necessary to differentiate the integrand to which Leibniz' rule can be applied. Leibniz' rule is given in equation 4.18 for some multi-variate function $f(x,t)$ due to be differentiated with respect to some variable t and integrated, between limits a and b that are dependent on t, with respect to some variable x,

$$\frac{\mathrm{d}}{\mathrm{d}t}\int_{a(t)}^{b(t)} f(x,t)\mathrm{d}x = f(b(t),t)\frac{\mathrm{d}}{\mathrm{d}t}b(t) - f(a(t),t)\frac{\mathrm{d}}{\mathrm{d}t}a(t) + \int_{a(t)}^{b(t)} \frac{\mathrm{d}}{\mathrm{d}t} f(x,t)\mathrm{d}x. \tag{4.18}$$

Applying this rule to equation 4.17 will yield a more mathematically tactile form of the expression which will allow for an analysis of r_c,

$$\begin{aligned} -\rho_p r_p^2 \dot{r}_p &= \frac{\mathrm{d}}{\mathrm{d}t}\int_{r_p}^{r_c} \rho_c(r,t) r^2 \mathrm{d}r, \\ -\rho_p r_p^2 \dot{r}_p &= \rho_c\Big(r_c(t),t\Big) r_c(t)^2 \dot{r}_c - \rho_c\Big(r_p(t),t\Big) r_p(t)^2 \dot{r}_p + \int_{r_p(t)}^{r_c(t)} \dot{\rho}_c\Big(r,t\Big) r^2 \mathrm{d}r. \end{aligned} \tag{4.19}$$

For now the discussion will consider only the remaining integral on the right-hand side of equation 4.19. Looking back to equation 4.12 it can be seen that this integral has an analytical solution. By means of a trigonometric substitution, $\frac{r}{r_0} = \tan(\theta)$, the integral can be solved to achieve an analytical result for further use in equation 4.19. The integral is

carried out in full below,

$$\begin{aligned}
\int_{r_p}^{r_c} \frac{r_p\dot{r}_p r^2}{r_0^2+r^2}\mathrm{d}r &= r_p\dot{r}_p\int_{r_p}^{r_c}\frac{r^2}{r_0^2+r^2}\mathrm{d}r,\\
&= r_p\dot{r}_p\int_{\theta_p}^{\theta_c}\frac{r_0^2\tan^2(\theta)r_0\sec^2(\theta)\mathrm{d}\theta}{r_0^2+r_0^2\tan^2(\theta)},\\
&= r_0r_p\dot{r}_p\int_{\theta_p}^{\theta_c}\frac{\tan^2(\theta)\sec^2(\theta)\mathrm{d}\theta}{1+\tan^2(\theta)},\\
&= r_0r_p\dot{r}_p\int_{\theta_p}^{\theta_c}\frac{\tan^2(\theta)\sec^2(\theta)\mathrm{d}\theta}{\sec^2(\theta)},\\
&= r_0r_p\dot{r}_p\int_{\theta_p}^{\theta_c}\tan^2(\theta)\mathrm{d}\theta,\\
&= r_0r_p\dot{r}_p\left(\int_{\theta_p}^{\theta_c}\sec^2\theta\mathrm{d}\theta-\int_{\theta_p}^{\theta_c}\mathrm{d}\theta\right),\\
&= r_0r_p\dot{r}_p\left(\tan\theta_c-\tan\theta_p-\Big(\theta_c-\theta_p\Big)\right),\\
&= r_0r_p\dot{r}_p\left[\frac{r_c}{r_0}-\frac{r_p}{r_0}+\tan^{-1}\left(\frac{r_p}{r_0}\right)-\tan^{-1}\left(\frac{r_c}{r_0}\right)\right].
\end{aligned} \tag{4.20}$$

With this new result, attention may be now directed towards equation 4.19. The equation may be rewritten with the final term on the right hand side and can be evaluated with this new result,

$$-\rho_p r_p^2\dot{r}_p=\rho_c\Big(r_c,t\Big)r_c^2\dot{r}_c-\rho_c\Big(r_p,t\Big)r_p^2\dot{r}_p+2\epsilon\rho_p r_p\dot{r}_p\left(r_c-r_p+r_0\tan^{-1}\left(\frac{r_p}{r_0}\right)-r_0\tan^{-1}\left(\frac{r_c}{r_0}\right)\right), \tag{4.21}$$

where the time-dependence of r_p and r_c is now implied. Equation 4.21 is an ordinary differential equation for r_c. The presence of the $r_p, \dot{r}_p$ and ρ_c terms and their (now implied) time-dependence inhibit any significant analytical advance towards an exact solution. However, late-time behaviour of the system can be studied and a numerical solution can deliver the temporal behaviour of the cloud size r_c, which in turn will give an outer limit for the cloud and permit an evaluation of the density for all times. This numerical solution can be supported by a comparison to the analytical result for late-time behaviour.

4.2.1 Solution by Numerical Method

Formulating the problem

Equation 4.21 describes the pellet-cloud system using continuous functions but the difficulty in determining an analytical solution encourages the use of numerical techniques. To arrive at a numerical solution, a continuous function must be discretised - that is, the value of the function must only be known at specified points over the range of the domain on grid points. If the grid begins at 0 and stops at N in integer steps, then at some point n the value of the function, $y(x)$ is approximated to $y_n(x_n)$ for some, now discretised, input x. The derivative of the function can be defined in a similar way which is a crucial step to take. Initial value problems are presented as the derivative of the desired quantity as a function of that quantity and the known input, all of which are now discretised. This is summarised in equations 4.22 - 4.24.

$$x \to x_n, \tag{4.22}$$

$$y(x) \to y_n(x_n), \tag{4.23}$$

$$f'(x,y) \to f'_n(x_n, y_n), \tag{4.24}$$

where $y(x) = f(x)$. Looking to equation 4.21 once more, we see that these analogous functions are present: r_c is the desired quantity with some input t and the derivative, $\dot{r}_c$. Re-arranging equation 4.21 so that $\dot{r}_c$ is the subject and highlighting time-dependent quantities,

$$\dot{r}_c = \frac{1}{r_c^2}\frac{r_0^2+r_c^2}{r_0^2+r_p^2}\left[r_p^2\dot{r}_p - 2r_p\dot{r}_p\left(r_c - r_p + r_0\tan^{-1}\left(\frac{r_p}{r_0}\right) - r_0\tan^{-1}\left(\frac{r_c}{r_0}\right)\right) - \frac{1}{\epsilon}r_p^2\dot{r}_p\right]. \tag{4.25}$$

This equation (4.25) is still not yet in a position to be effectively solved numerically. It remains to be discretised for use in a numerical scheme and also to be normalised by means of non-dimensional variables. Normalisation of quantities is a common technique used in numerical analysis for several reasons. It allows for the identification of common scale lengths or common derived quantities, such as velocities, which can simplify the appearance of these equations further. It maintains the significance of data during subtraction operations between two similar numbers, in calculating a derivative for example, whereby the most significant digits are cancelled by the subtraction leaving only the least significant digits

which could potentially be random due to machine error. These digits are raised in significance and negate any value the result previously held. Normalisation of variables inhibits this effect but does not guarantee its absence. For these reasons, equation 4.25 will be normalised by scaling all lengths in the system to that of the initial pellet radius. Normalised quantities are denoted by a tilde and shown below for the two quantities of relevance here in equations 4.26 and 4.27. Similarly for the time-dependent quantities, the scale-length of choice would be the lifetime of the pellet, defined previously as t_f,

$$\tilde{r}_p = \frac{r_p}{r_0}, \qquad \frac{\mathrm{d}\tilde{r}_p}{\mathrm{d}\tilde{t}} = \dot{\tilde{r}}_p = \frac{\dot{r}_p t_f}{r_0}, \tag{4.26}$$

$$\tilde{r}_c = \frac{r_c}{r_0}, \qquad \frac{\mathrm{d}\tilde{r}_c}{\mathrm{d}\tilde{t}} = \dot{\tilde{r}}_c = \frac{\dot{r}_c t_f}{r_0}. \tag{4.27}$$

It can be seen that in the inverse tangent functions of equation 4.25, this scale-length naturally occurs. This choice of normalisation therefore lends itself well to simplifying the appearance of this equation. With discretisation applied, where a subscript n denotes the grid point under examination, equation 4.28 defines the final discretised equation to be numerically solved,

$$\dot{\tilde{r}}_c = K \frac{1}{\tilde{r}_c^2} \frac{1+\tilde{r}_c^2}{1+\tilde{r}_p^2} \left[\tilde{r}_p^2 \dot{\tilde{r}}_p - 2\tilde{r}_p \dot{\tilde{r}}_p \left(\tilde{r}_c - \tilde{r}_p + \tan^{-1}\left(\tilde{r}_p\right) - \tan^{-1}\left(\tilde{r}_c\right) \right) - \frac{1}{\epsilon} \tilde{r}_p^2 \dot{\tilde{r}}_p \right]. \tag{4.28}$$

For the case of equation 4.28, the normalisation constant, K, is equal to 1.

Selecting a method

For an initial value problem such as equation 4.28, a wide variety of solving algorithms exist. The simplest of these is the Euler method,

$$y_{n+1} = y_n + h f'(x_n, y_n). \tag{4.29}$$

A common issue with a method as simple as the Euler method is that the accuracy of the solution is not satisfactory for a larger step size, h. Smaller step sizes are needed but this will incur additional computational expense which may not be desirable for the particular problem under investigation. The Euler method is also subject to instability much more easily than other methods. The problem with the Euler method lies in its simplicity. If additional, intermediate steps are introduced which evaluate y at a point

between n and $n+1$ and if a weighted average to the intermediate and final evaluations would result in a more accurate result for the $n+1$ step. One such family of solution methods that incorporates these calculations is the *Runge-Kutta methods*. The fourth-order method is generally considered the optimal Runge-Kutta integrator in these family of solutions. Lower order methods compromise on accuracy and higher order methods require an additional calculation for the order of the method applied and so the fourth-order method has naturally reigned dominant in the practise of solving ordinary differential equations. The solution is calculated by evaluating the derivative at 3 trial points and then aggregating the results of those steps to determine the next step. Suppose the value of a function at the nth point is known and the value for successive values $n+1$ through to N are desired. For the case of the fourth order method, the value y_{n+1} is determined as follows:

$$y_{n+1} = y_n + \frac{1}{6}\Big(k_1 + 2k_2 + 2k_3 + k_4\Big), \tag{4.30}$$

where k_{1-4} are defined as:

$$\begin{aligned}
k_1 &= hf'(x_n, y_n),\\
k_2 &= hf'(x_n + \frac{h}{2}, y_n + \frac{k_1}{2}),\\
k_3 &= hf'(x_n + \frac{h}{2}, y_n + \frac{k_2}{2}),\\
k_4 &= hf'(x_n + h, y_n + k_3).
\end{aligned}$$

For the initial value problem given in equation 4.28 the initial conditions are known. At the start the pellet has a radius $r_p = r_0$ at time $t = 0$ and at this same time the cloud has not formed. If a common coordinate system is used then the cloud radius at $t = 0$ is $r_c = r_0$ which acts as y_0 and the normalised input variable $\tilde{t}$ will range from 0 to 1.0. For a step size of $h = t_{n+1} - t_n$ this algorithm is used to determine the solution for r_c from the differential equation described by equation 4.28.

4.2.2 Late-time Analysis

It was stipulated in the criteria for the density profile that it would be necessary for it to have no further time-evolution at $t = t_f$ which is satisfied by the inverse-square function used. It can therefore be said that a terminal cloud size exists, r_{cf} at $t = t_f$, at the instant that ablation ceases as the cloud will continue to expand but with no addition of new

matter. At this time, the pellet is fully ablated and $r_p = 0$ and consequently all the mass in the system is in the cloud. In other words the fixed initial mass with constant density in the solid pellet has been converted to gas following a prescribed density profile. The integration of the density over the pellet size at the start yields the mass and the integration of the density profile across the cloud should yield the same number implying that there exists a fixed value, r_{cf}, that satisfies this equality. It is expected that at this stage in the system's evolution that the cloud will be much larger than the pellet's original size, $r_{cf} \gg r_0$. This approximation in conjunction with the terminal distribution of matter will allow for an examination of the late-time behaviour of the cloud size,

$$\begin{aligned}
M_0 &= M_c, \\
\frac{4\pi}{3}\rho_p r_0^3 &= 4\pi\epsilon\rho_p \int_0^{r_{cf}} \frac{r_0^2 + r_p^2(t_f)}{r_0^2 + r^2} r^2 \mathrm{d}r, \\
\frac{1}{3} r_0^3 &= \epsilon r_0^2 \int_0^{r_{cf}} \frac{r^2 \mathrm{d}r}{r_0^2 + r^2}, \\
\frac{r_0}{3} &= \epsilon \left(r_{cf} - r_0 \tan^{-1}\left(\frac{r_{cf}}{r_0}\right)\right), \\
&\approx \epsilon \left(r_{cf} - \frac{\pi}{2} r_0 \right), \\
r_{cf} &\approx r_0 \left(\frac{1}{3\epsilon} + \frac{\pi}{2} \right),
\end{aligned}$$

with a choice of $\epsilon = 0.01$ this expression evaluates to be ≈ 35. It will be essential for any cloud with this density profile to arrive at this terminal radius.

4.3 Calculated Cloud Properties

In the above calculations, the value of k_2 was open to selection, only affecting the rate at which the cloud expansion occurred. This value should be dynamically varied to represent the changing in ablation rate due to the shielding of the cloud but for the meantime a constant value of $k_2 = 10.0$ will be assumed unless otherwise stated.

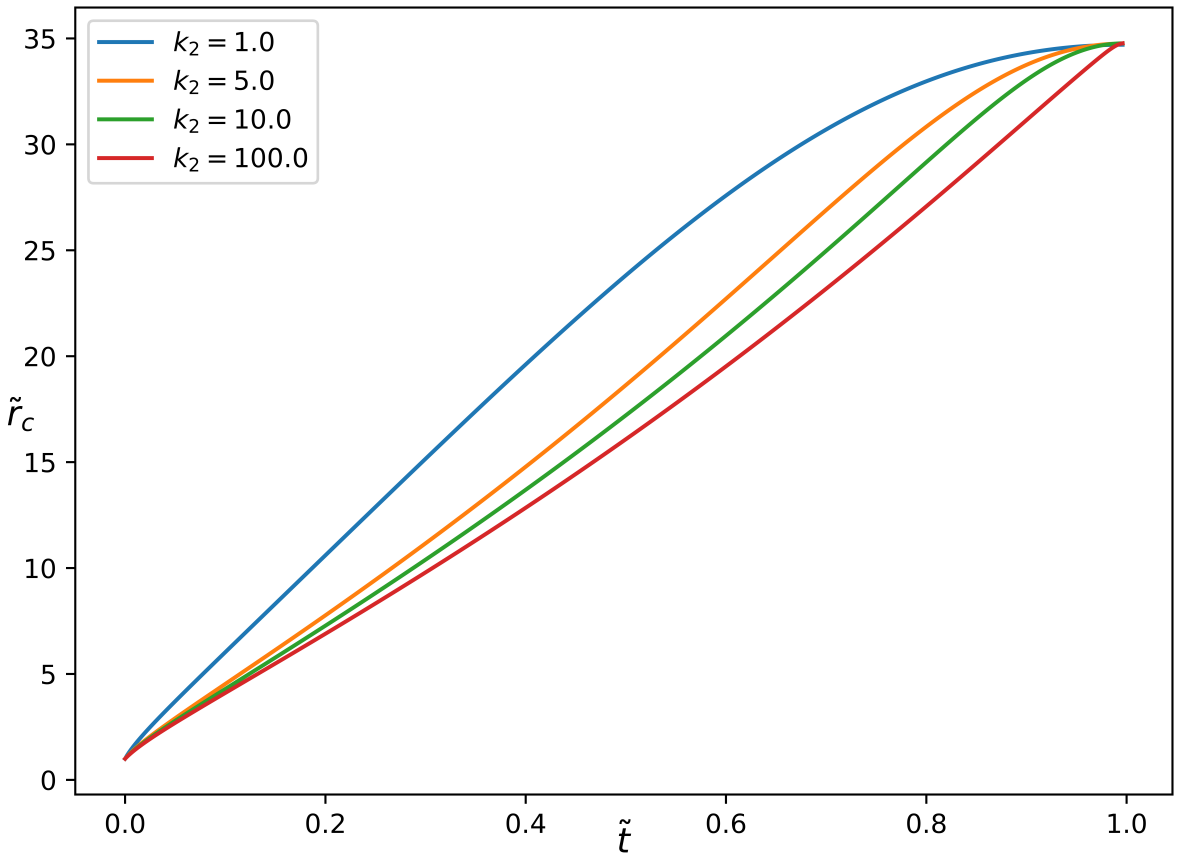

Figure 4.5: The numerical solution to equation 4.28 for several choices of the parameter k_2. This dependence is implicit in the r_p, $\dot{r}_p$ and r_c functions. Irrespective of the choice of k_2, the cloud always reaches a size ≈ 35 times larger than the initial radius.

4.3.1 The Cloud Radius, r_c

From figure 4.5 it is encouraging that the terminal size for any choice of k_2 yields the same result as for the analytical approximation. The solution to equation 4.28 is also monotonically increasing with no local maxima or minima which is to be expected for an ever-expanding cloud with the choice of k_2 affecting only the rate. A direct comparison to some observations is also necessary to examine not just the trends but also the absolute values the model predicts. Moderate agreement is found between the results here and the reports of cloud sizes of about 3cm which corresponds to $\approx 30 r_0$ for a pellet size of 1mm which is commonplace in the field as reported in Pégourié et al. (2005). This agreement is matched from much earlier observations of pellet injection into the ORMAK tokamak Foster

et al. (1977). Pellets of 200μm radius developed a maximal cloud size of ~ 0.5cm which is comfortably similar to predictions from the model. However, these kinds of comparisons are not trivial. Firstly, no consideration of ionisation of the cloud has been performed in this calculation which will certainly happen in a real system. Once that ionisation occurs, the strong magnetic field will elongate the cloud along that axis and inhibit cross-field motion. It is not widely recorded in the literature along what axis these measurements are made or at what stage in the pellet-cloud system evolution the measurement was made. Moreover, any material that was sourced from the pellet but is now fully ionised and in thermal equilibrium with the background plasma will be indistinguishable from particles that were there prior to the pellet's injection. It is therefore incredibly difficult for a simple model such as this to accurately replicate measurements from a complicated system such as this. The similarity, even at face value, of these results is enough to consider this a viable "toy" model.

4.3.2 The Cloud Density, ρ_c

The density of the neutral cloud is visualised in the symmetric 2D geometry in figure 4.7 and its comparison to observation sees the same success and suffers similar issues as with r_c. The density has a range of approximately $10^{-2}\rho_0 \mathrm{m}^{-3}$ to $\rho_0 10^{-5}\mathrm{m}^{-3}$. Based on initial densities of $0.086\mathrm{gcm}^{-3}$ which equates to approximately $2\times10^{28}\mathrm{m}^{-3}$, this corresponds to a range of around $2\times10^{26}\mathrm{m}^{-3}$ to $2\times10^{23}\mathrm{m}^{-3}$. Observed densities of $10^{24}\mathrm{m}^{-3}$ fall within this range but again there is little record of when in the evolution and where in the cloud this measurement was taken Pégourié et al. (2005). Figure 1 in Lengyel et al. (1991) presents data on the neutral density of the cloud of about $10^{25}\mathrm{m}^{-3}$ which is in agreement with the results presented here (with approximate agreement in terms of cloud size also). Similar results are presented in Senichenkov et al. (2006) and supporting numbers stated in Pégourié (2007) and Garzotti et al. (2010). The difficulty in comparing this model to real results lies in two camps: the simplicity of the model, and lack of spatially and temporally accurate data. The simplicity of the model was a specific aim of this research because it enables more mathematical work to be undertaken investigating other facets of the physics. In pursuing a more tactile model, essential physics has had to be ignored such as the thermodynamics within the pellet which may in fact differ significantly from evaporation physics and the hydrodynamics of an expanding cloud. However, a case has been made for pursuing a simple model such as this but the existence of temporally resolved measurements of cloud sizes and densities with spatial resolution that agree with results in

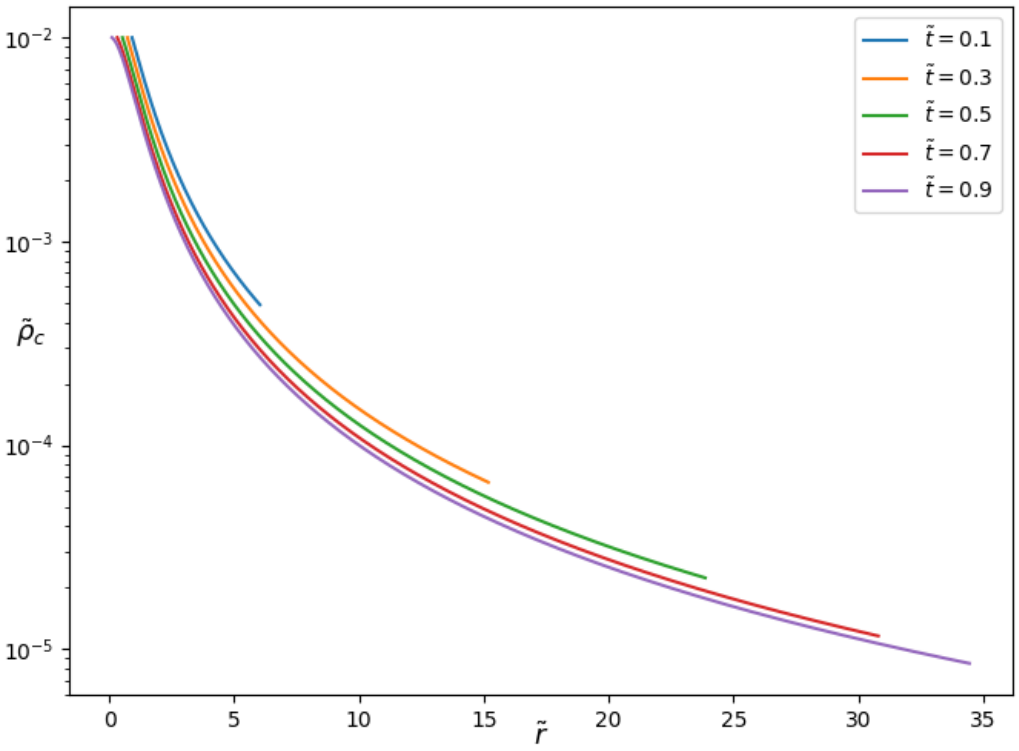

Figure 4.6: Density profiles for the neutral gas ablated from the pellet for various times.

this chapter would support the model as a valid description of the system.

4.4 Conclusion

The research presented in this chapter is novel in that it assumes a similarity in behaviour with evaporation of aerosol droplets, evading the need for a discussion of kinetic and thermodynamic phenomena. The mathematical law used has been adapted to avoid unphysical behaviour at lower pellet sizes which is a new piece of work that this thesis achieves. Using a combination of analytical and numerical techniques and by conserving mass, solutions for the cloud extent and density profile have been evaluated capture temporal and spatial variation. This is also an original effort which bears some agreement

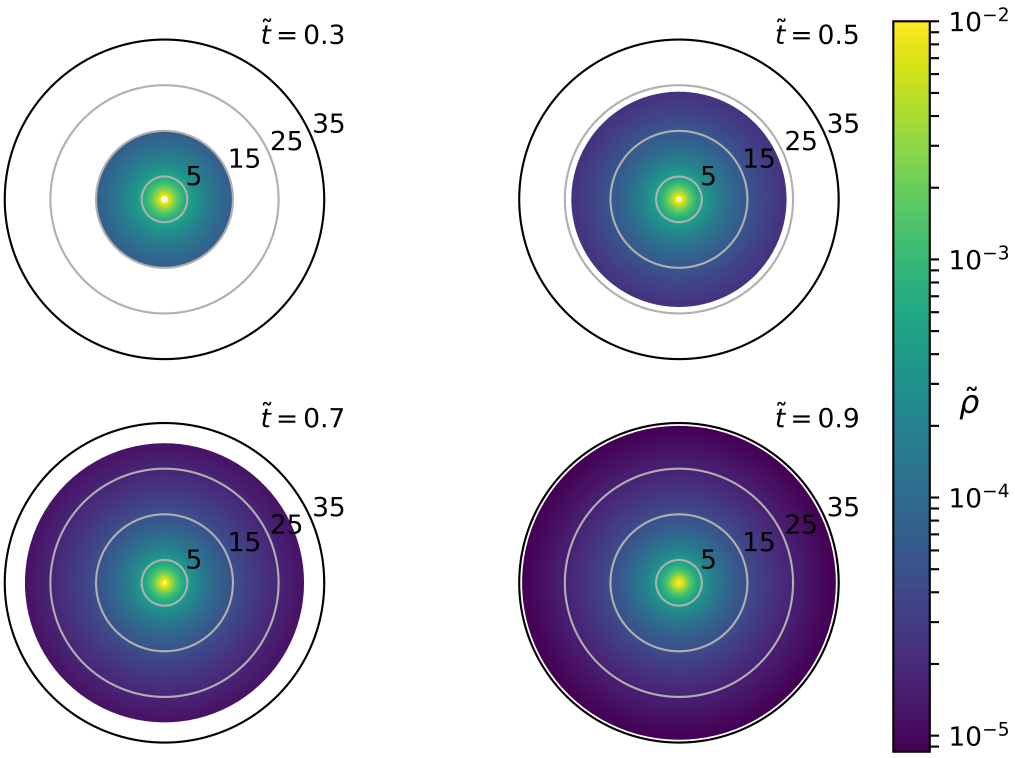

Figure 4.7: Two dimensional representations of the cloud with the density given by the colourbar on the right hand side. The cloud is shown to have expanded over the course of the pellet's lifetime and reaches a terminal size of $\approx 35 r_0$.

with observations but omits details which could close the gap on the discrepancy. With these physical quantities now known, attention can turn to the interaction of the background plasma with the cloud by means of the CSDA which will be explored in the following chapter.

Chapter 5

The Bethe Stopping Power Calculation in a Dense, Neutral H_2 Cloud

The model in chapter 4 has defined a temporal evolution to the cloud density with the expansion of the cloud front and recession of the pellet surface captured. However, the question still remains as to what species is causing this ablation. The evidence presented in chapter 2 indicates that electrons are performing the ablation and ions are far too collisional to make their way into the cloud. The arguments in chapter 3 have shown that for the typical parameters of these systems the CSDA is appropriate and these parameters have been recovered with the model in chapter 4. Attention may now be turned to the simulation that tackles the research problem in this thesis.

This chapter will use the formula given in Seltzer and Berger (1984) to evaluate how the energy from incident electrons is lost to the dense cloud. This calculation will allow for a determination on the spatial distribution of electrons throughout the cloud due to this interaction and a measure of the shielding effect the cloud has by considering the minimum energy needed to traverse the cloud. The evaporative model that has been developed also permits exploration of the variation of these quantities with time.

The CSDA which was previously discussed in chapter 3 will be employed in this chapter to evaluate energy losses and particle deposition in the dense cloud. The application of a stopping power calculation to a fusion environment has not been considered for plasma-cloud interactions in tokamaks but is usually reserved for studies on damage to

plasma-facing components and inertial confinement experiments as in Igitkhanov et al. (2011) and Deutsch (2019). This presents a new and undocumented approach to study the gas-plasma interaction that forms part of the elementary structure of this thesis. The following sections will detail the particulars of this application including a review of the assumptions, the criteria to be satisfied to use CSDA and the structure of the numerical simulation.

5.1 The Simulation Structure

The simulation outlined in this chapter is a one-dimensional kinetic problem modelling the slowing of electrons due to the CSDA in a dense, neutral hydrogen gas. Sufficiently energetic particles will traverse the entirety of the cloud and reach the solid pellet at which point any remaining energy is expended in the ablation and release of molecules that will add to the cloud structure. The density profile will suffer a perturbation which reaches a new equilibrium almost instantly and establishes the r^{-2} profile that was illustrated in chapter 4. Of course, any stopped electrons will then produce an electrostatic field which will then act to slow any additional incoming electrons after being advected a short distance due to the cloud's outflow. Those stopped electrons will have lost energy to neutrals throughout the cloud acting as a source of positive or negative ions or other more short-lived species.
The simulation's larger structure is outlined below and detailed graphically in figure 5.1.

1. Initial conditions of simulation are set up with an initial pellet and cloud size with the r^{-2} density profile.

2. The distribution of electrons is discretised into a histogram spanning an energy range with a number of bins with a given bin width. A test particle from each bin is taken to represent every electron in the distribution from that bin.

3. The Bethe equation is solved for each test particle. For particles that stop in the cloud, the fraction of the distribution occupied by the bin corresponds to the density of particles at that point and for particles that reach the pellet the bin size determines the energy flux and number flux delivered to the pellet's surface.

4. Energy and number fluxes at the pellet's surface are calculated.

5. The energy flux at the pellet determines the number of particles released by ablation in the timestep of size Δt which corresponds to a new pellet size if a constant solid state density is assumed.

6. The new pellet radius corresponds to a new cloud size and density profile. A check on the system parameters and whether they meet any termination criteria is performed and then either:

   - the pellet is deemed to be fully ablated and the simulation ceases.

   otherwise:

   - the simulation continues.

7. The system then transitions from one equilibrium state to another, transporting electrons from their deposited position to a new position farther from the pellet surface, moving with the flow of gas. This is because the electrons are expected to attach to the neutrals and therefore the electrons are transport as if they were neutrals. The electrostatic potential created by the distribution of electrons is calculated for their new positions using an iterative method. This potential will then additionally retard the next iteration of electrons to be injected into the system.

Each step in this process will be expanded upon further in the following subsections of the chapter.

5.1.1 Initial Conditions and Setup

The initial conditions for the simulation cannot simply be at $\tilde{t} = 0$ because at this time the sheath would be larger than cloud and a comparison between models will be more complicated. Instead, the simulation will begin at a time when the length of the cloud is equal to the length of the sheath. Once the cloud is larger than the sheath, and the floating potential at the pellet has been stabilised, then it can be safely assumed owing to the vastly greater volume of the plasma compared to the pellet that the plasma can comfortably zero any electrostatic perturbation at the cloud edge. Consequently, the electric potential boundary condition at $r = r_c$ is 0V and a parallel-plate capacitor has effectively formed inside the cloud with some charge distribution between them. The potential from the sheath field (illustrated in section 1.3) and the stopped electrons can then be added to produce the total potential.

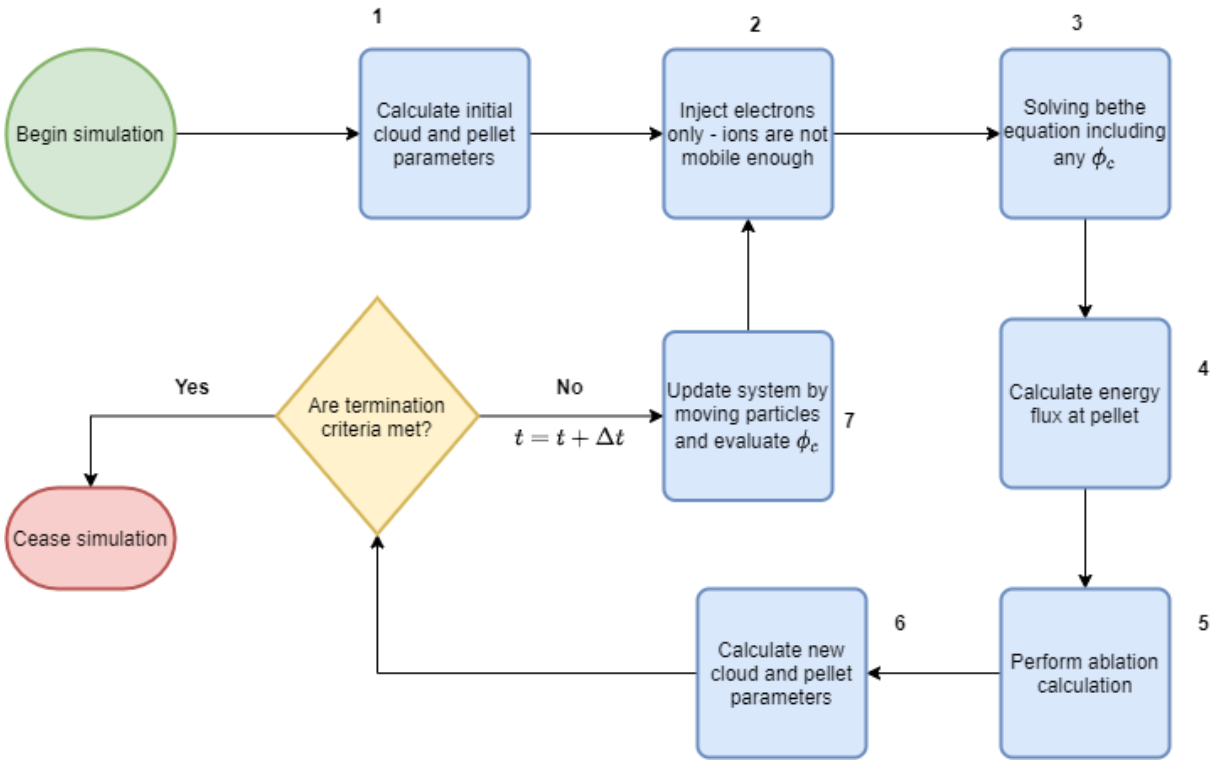

Figure 5.1: The flow diagram of processes and decisions in the simulation of the pellet ablation and evolution of the pellet-cloud system.

5.1.2 The Injected Electrons and their Distribution

For many practical fusion plasmas, the mean energy of electrons is typically 1keV. Equation 1.22 from section 1.2.2 calculates the distribution of energy across all available energy states. For the purposes of this simulation the distribution will be discretised with an appropriate bin size and the mid-point energy for each bin will represent every particle in that bin. For a distribution that ranges from 0eV to 7keV with bin sizes of 50eV the histogram in figure 5.2 is presented with the accompanying continuous distribution. The offset between mean energy and most common energy is clearly observed and the population of energy states quickly becomes small compared to the most populated state at an energy around $5\bar{E}$. As is expected from a Maxwell-Boltzmann distribution of energies, the majority of particles have energies lying between $[0, 4\bar{E}]$. This does not mean that higher energy particles are insignificant, but only that there are very few of them when considering the entire sample. Each bin in the discretised distribution in figure 5.2 will act as the input to the CSDA calculation discussed in the following section. The range of energies will need revision due

to limitations imposed by the mean excitation energy, I, from equation 3.2 and the high energy needed to fully penetrate and perform any ablation at all. Consequently, the range of energies will be from 125eV to 19.975 keV inclusive with 50eV bin size for the results in this chapter. This range has been chosen because it allows for the simulation to capture the lowest energies in the distribution and also energies significantly greater than the mean which are needed to fully traverse the cloud at later times.
The bins are calculated by means of a simple geometric argument on the electron energy distribution function (EEDF) which in this case is a Maxwellian. The trapezium rule has been applied to the normalised EEDF to determine the bin size for each energy such that the two sampled points, say $f_1 = f(E_1)$ and $f_2 = f(E_2)$, are represented by a single intermediate point defined by the average of the two energies, or equivalently the mid-point. This means that there are $N-1$ bins for N sampled points for the EEDF. The trapezium rule then applied to the EEDF between points 1 and N for an arbitrary point i is

$$\bar{f}_i = \frac{f_i + f_{i+1}}{2} E_b \tag{5.1}$$

where $\bar{f}_i$ is the value of the bin with a width E_b. This only works effectively when $\int_0^\infty f(E)\mathrm{d}E = 1$ which is given in Chapter 3 but because of the discretised nature of computational work there must be a minimum and maximum energy so that $\int_{E_{min}}^{E_{max}} f(E)\mathrm{d}E = 1$. The approximation to an integral by using the trapezium rule also means that

$$\sum_{i=0}^{N} \bar{f}_i = 1. \tag{5.2}$$

Determining the Resultant Density

Following a solution to the CSDA, the density profile may be calculated based on the stopping points of the energies associated with each bin. Supposing that the number of bins, and therefore initial energies, is 50 then there will be a density profile comprising, at most, 50 points. However, if the range of the cloud on the finite grid occupies 80 points then it will be necessary to estimate the density on those vacant 30 points. Interpolation is a perfectly fine method to use here because in a continuous distribution of charge a small bin with infinitessimal ΔE would stop at every point in the cloud. To interpolate to any missing points is acceptable as long as the sum of all the bins from pellet to cloud edge

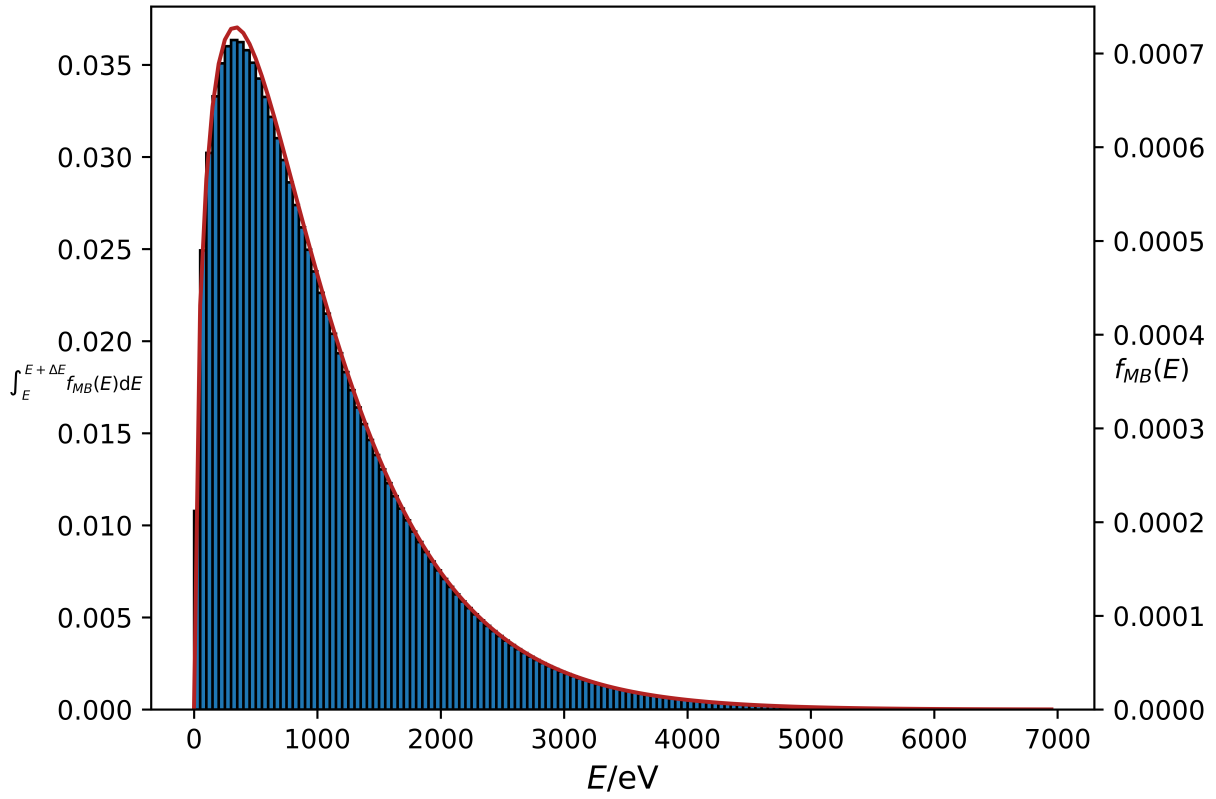

Figure 5.2: The Maxwell-Boltzmann distribution of energies for a 1keV mean energy. The blue histogram is associated with the left-hand axis and illustrates the fraction of the distribution lying within the 50eV bin centred on that energy. The distribution function (equation 1.22) given by the red line is associated with the right-hand axis.

returns 1 because (without ionisation) more charge can not be created in the cloud. The density may then need to be rescaled such that the charge is conserved and the extent of this rescaling will depend mostly on the number of points. In the equations below the term $\bar{f}(r)$ corresponds to the transformed density whereby the bin of the EEDF is transformed from energy space to real space to give a density profile, $n_e(r)$. This approach is outlined

in equations 5.3 and 5.4,

$$W = \sum_{i=0}^{N} \bar{f}_i, \tag{5.3}$$

$$n_e(r) = \frac{\bar{f}(r)}{W} n_0. \tag{5.4}$$

This means that for a larger number of grid points, the value W will be greater, because there are more points to be interpolated over and that the density at common points for a larger cloud will be lower than for a smaller cloud. This method allows for a small number of bins to be sampled from the distribution and scaled up to estimate how a more precisely divided distribution might behave.

5.1.3 The CSDA and its Solution

Data for the interaction of electrons with hydrogenic matter exists for equation 3.7 which will be solved (once normalised) for the case of electrons traversing the ablatant cloud which evolves as described in the previous chapter. A number of crucial differences need to be observed in the case of a deuterium pellet embedded in a deuterium plasma.

1. The r^{-2} profile - The density profile determined in the prior chapter will need to be used in place of the typically constant density ρ in equation 3.7. It is also essential to note that ρ_c is both a function of space and time. The equation will need to be solved across the domain of the cloud at each time of interest,

$$-\frac{1}{\rho_c(r,t)} \frac{\mathrm{d}E}{\mathrm{d}x} = \frac{c_1}{\beta^2} \frac{Z}{A} B(T). \tag{5.5}$$

2. Isotope approximation - The data provided is typically for mononucleonic hydrogen i.e. an atom with a single proton. As far as chemical behaviour is concerned, hydrogen is expected to have a similar set of interactions as deuterium. This means that values such as the mean ionisation energy, I, will be taken to be equivalent between isotopes. Data from NIST supports this assumption where the ionisation energy for H_2 is quoted as 15.4293 eV and D_2 as 15.46 eV which are comfortably close to equate and it is assumed that all analogous electronic transitions will be approximately similar also.

3. Similarity of state - Availability of data on solid hydrogen is difficult to acquire, especially for an instance as particular as this. As a consequence, data provided for liquid hydrogen in the Seltzer and Berger article will be used for this calculation. The value of I for liquid, molecular hydrogen is quoted as 22.3eV as in Seltzer and Berger (1984)

4. Z/A factor - One difference that does develop is the factor of Z/A, the ratio of atomic to mass number. A diatomic molecule of hydrogen possesses two protons and two electrons making this ratio equal to 1. However, a diatomic molecule of deuterium contains two protons, two electrons and *two neutrons*. The ratio of Z to A for deuterium is therefore 0.5. This will halve the stopping power at any given point and could have a significant effect on the fraction of electrons fully penetrating the cloud.

Normalisation and Integration Schemes

As before, any equation that is to be solved numerically must be appropriately discretised and normalised before the algorithm is applied. Normalisation constants for this system will be selected as the initial pellet radius r_0, the pellet density ρ_0 and the electron rest mass energy τ_e. Typical quantities are then normalised to the following:

$$\tilde{T} = \frac{T}{\tau_e}, \qquad \tilde{E} = \frac{E}{\tau_e}, \tag{5.6}$$

$$\tilde{\rho}_c = \frac{\rho_c}{\rho_0}, \qquad \tilde{x} = \frac{x}{r_0}. \tag{5.7}$$

This would create a normalised format of equation 5.5 given as,

$$\begin{aligned} \frac{1}{\tilde{\rho}_c}\frac{\mathrm{d}\tilde{E}}{\mathrm{d}\tilde{x}} &= \frac{\rho_0 r_0}{\tau_e}\frac{c_1}{2\tilde{T}}\frac{Z}{A}B(\tilde{T}), \\ \frac{\mathrm{d}\tilde{E}}{\mathrm{d}\tilde{x}} &= K\tilde{\rho}_c\frac{c_1}{2\tilde{T}}\frac{Z}{A}B(\tilde{T}), \end{aligned} \tag{5.8}$$

where $K = \frac{\rho_0 r_0}{\tau_e}$.This normalisation extends to the stopping function $B(T)$ and any quantities contained within it. Note that for our system, which is comfortably non-relativistic, the differences between E and T is negligible such that they can be equated in any further analysis. With a successful normalisation scheme chosen, solving this first order ODE can be done by means of the same scheme applied to solving equation 4.28 in section 4.2.1.

The fourth order Runge Kutta scheme demonstrated previously could be used to solve this initial value problem but it could be improved upon. That scheme used a fixed step dr to solve the discretised equation to an appropriate accuracy but where the function is practically unchanging across a step dr then a larger step could be taken that would also achieve the same accuracy but minimise the computational overhead.

The Runge-Kutta-Fehlberg Method

One such adaptive-step initial value problem (IVP) solver is the Runge-Kutta-Fehlberg Method. For a given function $f'(x, y_n)$ the method calculates y_{n+1} based on evaluations at both $x + \frac{h}{2}$ and $x + h$ (or any scaling of h) to fourth order and fifth order. If the two evaluations meet a certain accuracy requirement then the larger step size can be used and the process can be improved upon again to exam h and $2h$ to maximise the step that meets the error criterion. Of course, this process can be iterated over until the two evaluations are unsuitably different which allows for a window of accuracy that meets certain requirements in terms of errors and computational overhead. The evaluations are both based on Runge-Kutta methods with a series of k's given by

$$k_1 = f'\left(x, y\right), \tag{5.9}$$

$$k_2 = f'\left(x + \frac{1}{4}h, y + \frac{1}{4}hk_1\right), \tag{5.10}$$

$$k_3 = f'\left(x + \frac{3}{8}h, y + h\left(\frac{3}{32}k_1 + \frac{9}{32}k_2\right)\right), \tag{5.11}$$

$$k_4 = f'\left(x + \frac{12}{13}h, y + h\left(\frac{1932}{2197}k_1 - \frac{7200}{2197}k_2 + \frac{7296}{2197}k_3\right)\right), \tag{5.12}$$

$$k_5 = f'\left(x + h, y + h\left(\frac{43}{216}k_1 - 8k_2 + \frac{3680}{513}k_3 - \frac{845}{4104}k_4\right)\right), \tag{5.13}$$

$$k_6 = f'\left(x + \frac{1}{2}h, y + h\left(-\frac{8}{27}k_1 + 2k_2 - \frac{3544}{2565}k_3 + \frac{1859}{4104}k_4 - \frac{11}{40}k_5\right)\right). \tag{5.14}$$

The k_i's are defined in terms of k_j's for $j < i$ and the function to be integrated with fractional steps in the x coordinate. The large number of constants to track in these evaluations can be captured in a Butcher tableau (sometimes called a Butcher table). The

table can be interpreted as having a single column on the left hand side for coefficients on the step-size h to be added to the x coordinate in the evaluation of $f(x,y)$ with 5 columns on the right hand side corresponding to the coefficients on the various hk_i's to be added to y in the same evaluation. Beneath the 6 rows of these columns sits two more rows which define the sum of terms and their coefficients needed to evaluate to fourth and fifth order the solution. Explicitly these are given by

$$\begin{aligned} y^4_{n+1} &= y_n + h\left(\frac{16}{35}k1 + \frac{6656}{12825}k_3 + \frac{28561}{56430}k_4 - \frac{9}{55}k_5 + \frac{2}{55}k_6\right), \\ y^5_{n+1} &= y_n + h\left(\frac{25}{216}k_1 + \frac{1408}{2565}k_3 + \frac{2197}{4104}k_4 - \frac{1}{5}k_5\right), \end{aligned} \tag{5.15}$$

where $y^{4/5}_{n+1}$ refers to the $n+1$ solution to f and the superscript references the fourth or fifth order solution and is **not** an exponent.

Now, it could be argued that this method carries significantly more computational overhead and will therefore take longer to solve the same ODE but this is typically not the case. If the two solutions y^4 and y^5 are sufficiently similar, then the timestep can be increased (perhaps doubled) until in an ideal world the error criteria are *just* satisfied, then the solution can be arrived at with sufficient accuracy at a quicker rate than by taking much smaller steps. For a single energy or time, this is not necessarily useful, particularly if the timestep can be guessed to be correct and achieve an acceptable solution. For the problem in this thesis, there is a several order of magnitude spread in density and initial electron energy which presents a broad range of stopping power based on equation 5.8 and a single fixed step will not maximise efficiency. Allowing an algorithm to select the step to meet a defined error criteria could make the step ten times larger for a portion of the cloud where $\frac{\mathrm{d}\tilde{E}}{\mathrm{d}\tilde{x}}$ is particularly weak and correct it when it becomes stronger. The inclusion of an electric potential in the equation will make no difference to this calculation as the potential is precisely known at all points and only the losses due to electron-neutral collisions need the RKF method.

Adding an electric potential term to CSDA can be done in an ad-hoc way by looking at the units of $\frac{\mathrm{d}E}{\mathrm{d}x}$ which are J/m, which can be arrived at with electrostatic terms as $q\frac{\mathrm{d}\phi}{\mathrm{d}x}$. This is then approximated further over a small step h when calculated by the RKF algorithm such that

$$h\frac{\mathrm{d}\phi}{\mathrm{d}x} \approx \phi\big(x-h\big) - \phi\big(x\big). \tag{5.16}$$

0						
$\frac{1}{4}$	$\frac{1}{4}$					
$\frac{3}{8}$	$\frac{3}{32}$	$\frac{9}{32}$				
$\frac{12}{13}$	$\frac{1932}{2197}$	$-\frac{7200}{2197}$	$\frac{7296}{2197}$			
1	$\frac{43}{216}$	-8	$\frac{3680}{513}$	$-\frac{845}{4104}$		
$\frac{1}{2}$	$-\frac{8}{27}$	2	$-\frac{3544}{2565}$	$\frac{1859}{4104}$	$-\frac{11}{40}$	
	$\frac{16}{35}$	0	$\frac{6656}{12825}$	$\frac{28561}{56430}$	$-\frac{9}{55}$	$\frac{2}{55}$
	$\frac{25}{216}$	0	$\frac{1408}{2565}$	$\frac{2197}{4104}$	$-\frac{1}{5}$	0

Table 5.1: The Butcher table of the coefficients of the various iterations of the k's in the RKF solution. The value on the left side of the vertical line corresponds to the coefficient of h added to the x co-ordinate in the evaluation of f'. The ith number on the right hand side of the line is the coefficient of hk_i added to the y coordinate in that same evaluation. The jth row above the horizontal divider corresponds to the determination of k_j. Below the horizontal divider is the coefficients of the same k's as above of the fourth and then fifth order solution. This is perhaps more easily seen by comparison with equations 5.9 - 5.14.

Including the potential losses is done by adding the potential difference across the selected step size which approximates to $q\Delta\phi$ for a charge, q and a change in potential, $\Delta\phi$, which are presented in equation 5.19

$$\frac{\mathrm{d}\tilde{E}_i}{\mathrm{d}\tilde{x}_i} = K\tilde{\rho}_{c,i}\frac{c_1}{2\tilde{E}_i}\frac{Z}{A}B(\tilde{E}_i) \tag{5.17}$$

However, upon inspecting equation 3.7 it is possible that the stopping power term could potentially go positive if the $B(\tau)$ term is negative. This could happen at low energies due to the competing logarithm terms. Therefore, there must be a low energy limit to evaluating this equation, particularly within the context of a numerical solution. Looking

at equation 3.8 in the low energy limit it can be seen that

$$\begin{aligned}
B(\tau) &= B_0(T) - 2\ln\left(\frac{I}{m_e c^2}\right) - \delta, \\
B(\tau) &\approx B_0(\tau) - 2\ln\left(\frac{I}{m_e c^2}\right), \\
B_0(\tau) &= \ln\left(\frac{\tau^2(\tau+2)}{2}\right) + \frac{1}{(\tau+1)^2}\left(1 + \frac{\tau^2}{8} - (2\tau+1)\ln 2\right), \\
&\approx \ln\left(\tau^2\right) + 1 - \ln 2, \\
\implies \ln\left(\tau^2\right) + 1 - \ln 2 - 2\ln\left(2\tilde{I}\right) &> 0, \\
\ln\left(\tau^2\right) - \ln\left(2\tilde{I}^2\right) &> -1, \\
\ln\left(\frac{\tau^2}{2\tilde{I}^2}\right) &> -1, \\
\implies \tau &> \sqrt{\frac{2}{\mathrm{e}}}\tilde{I}.
\end{aligned} \tag{5.18}$$

The result in equation 5.18 acts as the truncation energy on any numerical solution to equation 5.5. If the value of τ is less than this limit, then $B(\tau)$ becomes less than 1 and then the stopping power becomes positive. This is unphysical and translates as the electron gaining energy by passing through the medium. Fortunately, for hydrogen gas I evaluates to ~ 19eV and any particles with approximately this energy will quickly lose this energy in a few mean free paths and it is acceptable to consider a particle with this energy as having stopped.

Including an Electrostatic Potential Term

Incorporating an additional energy cost due to any existing electrostatic potential within the cloud is rather easy to achieve in a crude way. In addition to the energy lost by collisions there is an additional loss (or gain, in some cases) due to the potential so a term can simply be added to the existing one to arrive at

$$-\frac{\mathrm{d}\tilde{E}}{\mathrm{d}\tilde{x}} = \tilde{q}\frac{\mathrm{d}\tilde{\phi}}{\mathrm{d}\tilde{x}} + K\tilde{\rho}_c\frac{c_1}{2\tilde{E}}\frac{Z}{A}B(\tilde{E}). \tag{5.19}$$

This is effectively what is done to achieve the results shown later in section 5.2. By solving the equation the difference in potential across the spatial step is solved for and the energy penalty (or boost) is applied to the particle over that step. However, in a later section it will be shown that the potential can be solved for through Poisson's equation using iterative methods which eliminates the need to solve the new term in equation 5.19. The potential will be solved across the entire domain at each grid point so the difference between one point and the next is

$$\Delta\tilde{\phi}_{i,i+1} = \tilde{\phi}_{i+1} - \tilde{\phi}_i. \tag{5.20}$$

This term can be added to the particle energy before undergoing the RKF solver on equation 5.17 for that step and the energy threshold criteria can be applied.

The CSDA Simulation Structure

The simulation proceeds as follows and is illustrated graphically in 5.3:

1. The Maxwell-Boltzmann distribution associated with the background plasma is divided into bins and a single particle (the energy of which is the midpoint of that bin) is simulated and accepted as being representative of the behaviour of every particle within that bin and the particle is injected at $r = r_c$.

2. The stopping power at the current point is calculated. If the stopping power is sufficient to lower the particle energy to less than the truncation energy (see equation 5.18), then the particle is said to have stopped. This condition is also extended to any of the intermediate steps at $x + k_{1-4}$ in the solver as the logarithm term to be evaluated in the stopping number will ultimately determine whether a particle has stopped.

3. If a particle's energy is less than the mean ionisation energy then

   - the particle is stopped and its position recorded.

   Otherwise

   - the particle proceeds a distance dr towards the pellet and steps 2 - 3 are repeated until the particle stops *or* until the particle reaches the pellet.

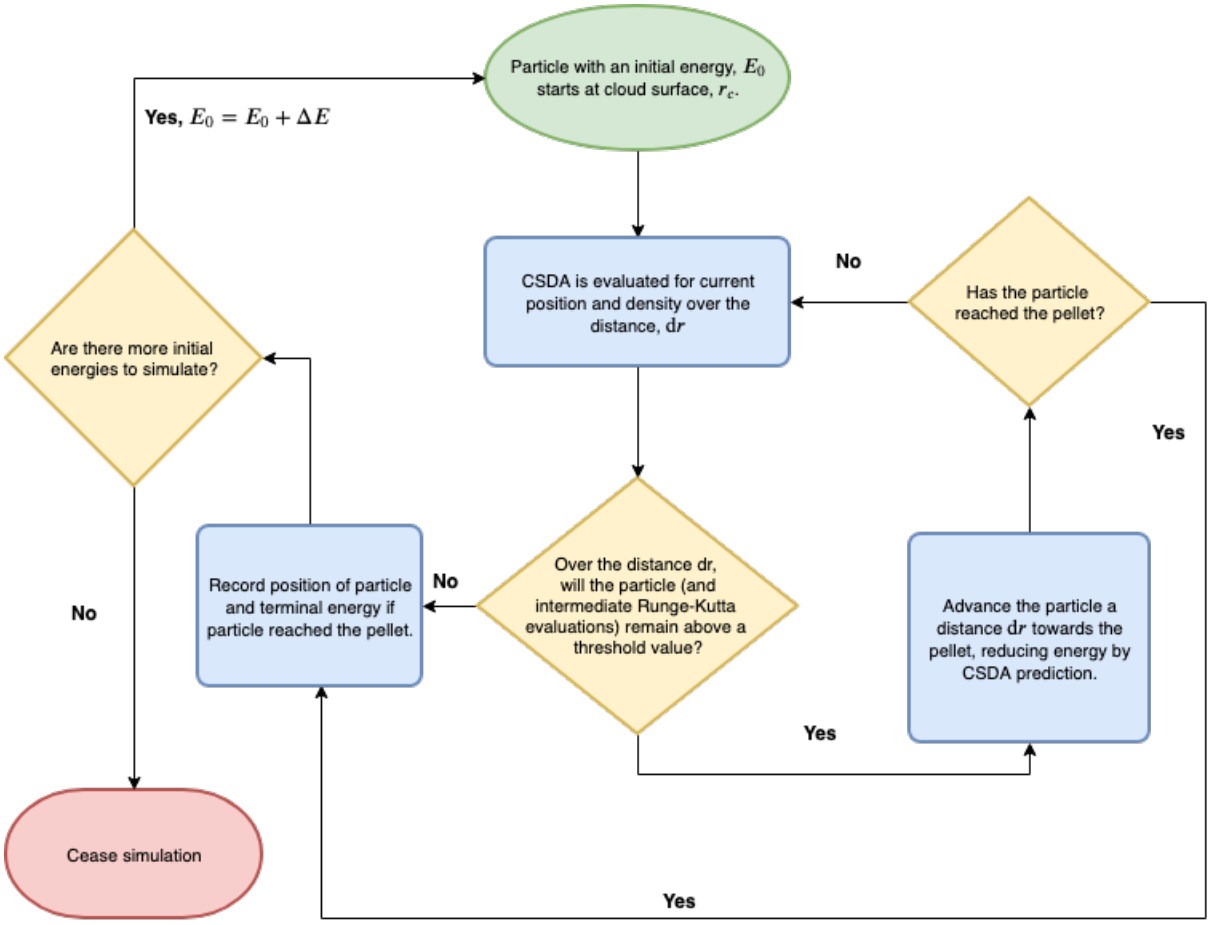

Figure 5.3: Simple flowchart to illustrate the simulation structure for the CSDA calculation.

4. Once a particle has stopped, at the pellet surface or otherwise, record the final energy above I and the final position.

5. If there are additional bins to be simulated then

   - Increase the initial energy to that associated with the mid-point of the next bin, inject the particle at $r = r_c$ and repeat steps 2 to 5.

   otherwise

   - Cease the simulation

The simulation was carried out for particles in the energy range 125eV to 19.975keV with bin sizes of 50eV. In this calculation it is assumed that all particles within that energy follow the same trajectory and kinetic behaviour so that it can be concluded that all particles

in that energy bin have stopped at that singular point. This allows for an interpretation of the density of stopped charge which will be crucial in the following chapter. Another quantity of interest includes the minimum energy required to traverse the cloud at any time. This will be used to comment on how the neutral shielding, based on this model, should evolve in time. Some additional results that follow from further calculation include the number and energy flux at the pellet surface and the expected remaining lifetime of the pellet.

Results

A number of key results can be drawn from the results of these calculations. In particular the minimum energy needed to cross the cloud, hereafter called the minimum traversal energy, and the density profile of deposited electrons are of immediate relevance to the research aims of this chapter. Results which follow from that such as expected lifetime will be discussed here to demonstrate the challenges overlooked by this simple approach which will be addressed in chapter 6.

The minimum initial energy required to fully traverse the cloud at any given time is presented in figure 5.4 and denoted by ϑ. The figure clearly shows that generally speaking the shielding of the cloud improves over the course of its lifetime. A case can be made to support this result by looking at the neutral density profiles from figure 4.6. The cloud subscribes to a r^{-2} but there is a significant overlap of profiles closer to the pellet in that up to a distance of $\sim 10r_0$ where the density always has a value of 10^{-2} to 10^{-3} $\tilde{\rho}_c$. Consequently, there will always be an (almost) base level of shielding the plasma will have to suffer. It is suspected that this arises due to the competition between the expanding cloud and the decreasing step-jump in density at $r = r_c$. The interplay between the greater distance to travel and the monotonically decreasing density at all points allows for ϑ to remain constant for the intermediate times in the pellet's lifetime. The increase seen at the end of the pellet's lifetime is perhaps due to the more significant expansion of the more dense section of the pellet outwards i.e. the injected electrons have a larger distance to cover in the more dense section of the cloud owing to the necessary minimum initial traversal energy. Of course, with more material to be traversed, it should only make sense that the amount of energy needed to move across the cloud would increase. This is particularly apparent when one recalls that the solution to the CSDA problem requires integrating a density over a length and because it is known that the mass in the cloud is always increasing then the total amount of stopping should also increase. Any variations on the trend can

be put down to integral difficulties with solving such a dynamically ranged problem with an adaptive step solver. The energy range under investigation needs to be several orders of magnitude, the density itself varies by a simiilar amount and the product of each in any permutation will span an even greater range. This makes it incredibly challenging to provide a general set of error criteria, even in non-dimensional and normalised variables, that can be reliably used to determine the appropriate step for the solver. The most consistent method would be a fixed step common to each time and energy for all cloud configurations however this becomes incredibly impractical when considering the spatial variation in the cloud at time $\tilde{t} = 0.1$ and $\tilde{t} = 0.9$. Consequently the occasional error on ϑ may be observed between one time and the next when considering large spans in $\tilde{t}$. This reinforces the statement made previously that the trend is what is being investigated here, not the accuracy of every single data point in the plot. At this point a new parameter η can be introduced, which represents the fraction of the background distribution of particles that have reached the pellet surface.

$$\eta = f_{passes} = \int_{\vartheta}^{\infty} f_{MB} \mathrm{d}E. \tag{5.21}$$

This new parameter will be called the *shielding efficiency*. Additionally, $1 - \eta$ represents the fraction of particles that have been stopped by the cloud. The minimum transmission energy over the pellet's lifetime is presented in figure 5.4.

Following from the outputs of the simulation, namely the deposition point of all electrons from a given bin, the density profile of the deposited electrons can be seen. Based on the assumption that all electrons in a given bin would interact in an identical way and thus stop at the same point (within, suppose, a mean free path), then the fraction of the background distribution would correspond to the fraction of the electrons that entered at that instant. Additionally, because the stopping power calculation for any instant in the evolution depends exclusively on the particle energy (and the range depends only on the initial energy for a given system) then the density profile should resemble the initial energy distributions. This can be seen most clearly in figure 5.5 at the earlier stages in the system's evolution. The peak seen, for example, for the line at $\tilde{t} = 0.1$ effectively corresponds to the fraction of the distribution associated with the energy bin closest to the most common energy. The exponential decrease in populated energy states for higher energies is seen in the density at points closer to the pellet's surface which is a hallmark indicator of a Maxwell-Boltzmann distribution. As the stopping decreases at later times the higher energy particles are stopped farther into the cloud and are spread out further,

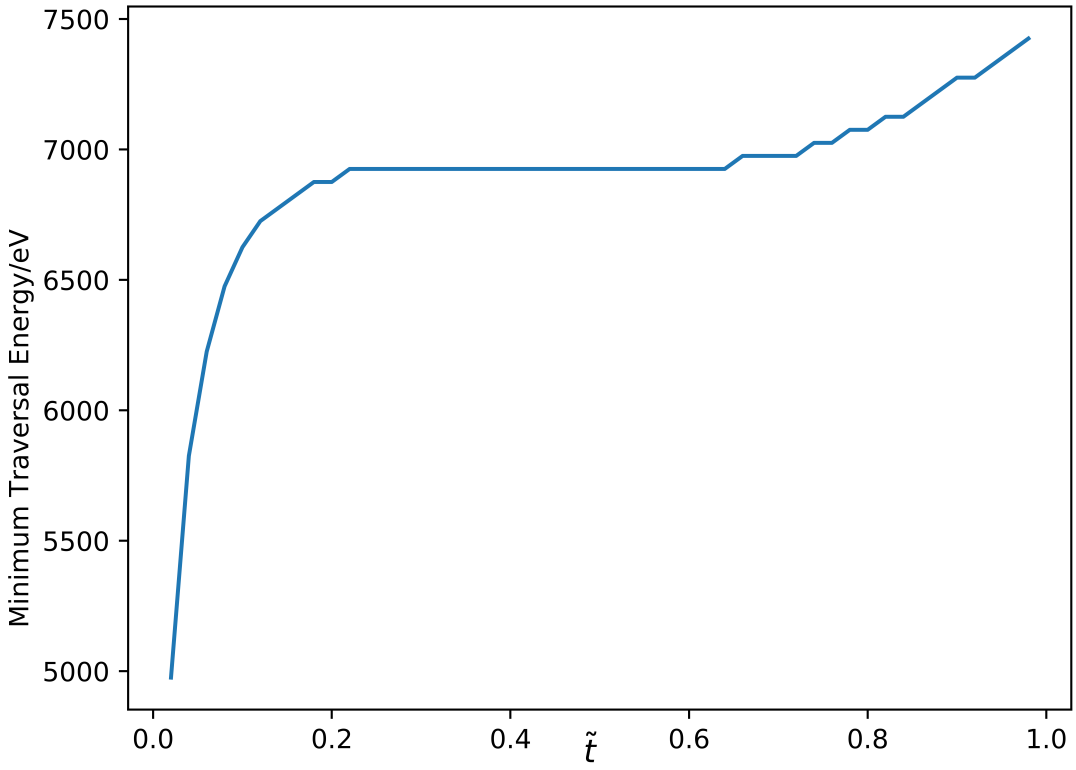

Figure 5.4: The minimum initial energy needed for electrons to fully traverse the cloud as a function of time.

resulting in a more flat profile across the cloud and the absence of the tightly peaked structure seen in the $\tilde{t} = 0.1$ profile.

It is important to note that the points on these profiles represent the fraction of the particles that have deposited at that associated point because the simulation stems from a distribution of particles. The conservation of mass here is now done by summing the points along the line to find $\sum \tilde{n}_e = 1$. This naturally diminishes the value of the density at any given point as the cloud expands because there are more points to cover across the domain of the cloud.

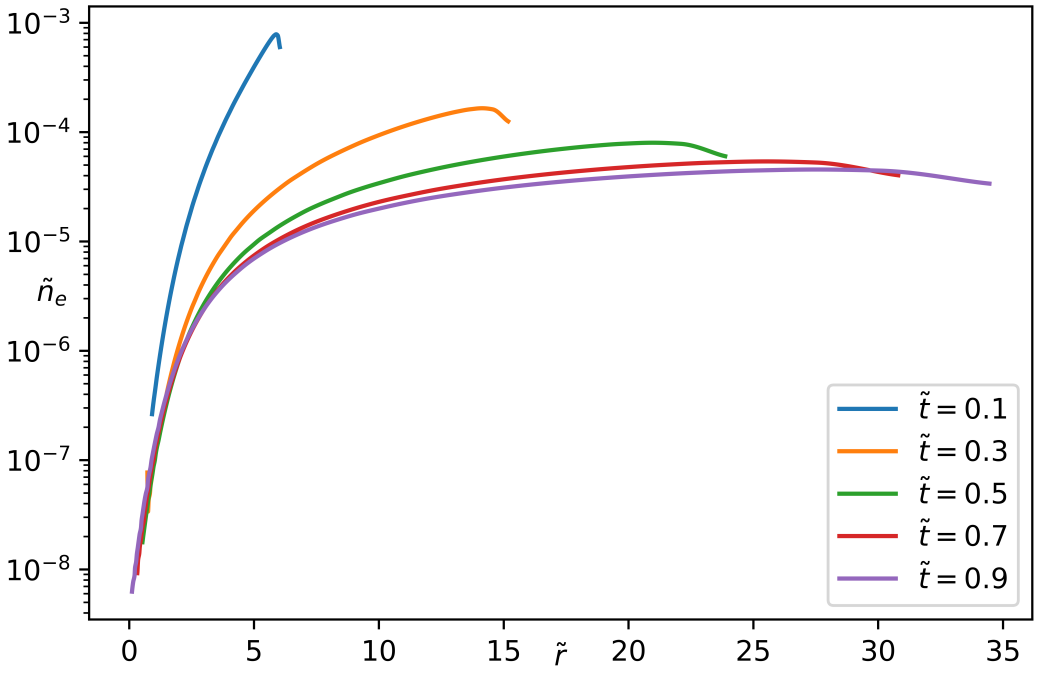

Figure 5.5: The normalised density of electrons after an instantaneous injection of particles from the background distribution for a series of stages in the temporal evolution of the system. The bins selected for the simulation had a $\Delta E = 50\text{eV}$ but the profile is interpolated to the grid points on the finite difference grid and rescaled such that the sum of the bins equals 1 . The right-hand edge of the line begins farther to the right as $\tilde{t}$ increases which captures the expanding front of the cloud.

5.1.4 Imposed Arbitrary Potential

The results given in the previous section demonstrate the transmission and distribution of stopped electrons in a perfectly neutral D_2 cloud. However, the stopped electrons will create a potential field for the following iteration of injected electrons which can be found by solving Poisson's equations. This work is developed in a later section but at the moment it is relevant to illustrate that a simple addition of a potential term to equation 5.8 will achieve this. The CSDA can be used to model the loss of energy across a distance but by incorporating a potential the energy lost due to electrostatic interactions can also be accounted for. Therefore, if the arbitrarily imposed potential is evaluated on each of those common grid points then the difference $\Delta\phi = \phi_2 - \phi_1$ can be evaluated and added to the

CSDA expression before evaluation via RKF. The CSDA_ϕ is therefore defined as

$$\frac{\mathrm{d}\tilde{E}}{\mathrm{d}\tilde{x}} = \tilde{q}\frac{\mathrm{d}\tilde{\phi}}{\mathrm{d}\tilde{x}} + K\tilde{\rho}_c\frac{c_1}{2\tilde{E}}\frac{Z}{A}B(\tilde{E}). \tag{5.22}$$

The normalisation of the potential here is in line with the constant chosen for the kinetic energy and particle energy,

$$\tilde{\phi} = \frac{\phi}{\tau_e}. \tag{5.23}$$

Understanding how an electric potential creates a departure from the charge-neutral CSDA will be important for understanding how valuing the significance of any seeded potential in any self-consistent simulation. This will be explored in section 5.2 later in the chapter. For now the energy flux calculation and its relation to ablation will be presented.

5.1.5 Arriving Energy Flux and Number Flux

Predictions may now be made on the remaining lifetime of the pellet. The qualifying word here is "remaining" because for the system to exist in its current state some time must have passed. In particular this is the time taken for the cloud to be as large as the sheath ($r_c = s$) but it would also correspond to any point after the starting point in a self-consistent simulation that evolves in time. Knowing now what fraction of the distribution of electrons has been stopped by the cloud, calculations on the number flux of particles striking the pellet, and also the imparted energy, may be performed. This is carried out by using the directed flux across an arbitrary surface which is done by considering the number of particles in the Maxwell-Boltzmann distribution in phase-space that have positive velocities along on axis. This is then scaled by any azimuthal and polar variation. The result can be found on page 37 of Lieberman and Lichtenberg (2005). Using the directed flux towards a surface (presented again in equation 5.24) and scaling by the fraction of particles that make it to the pellet, the impacting number flux is evaluated as,

$$\Gamma_N = \frac{1}{4}n_0\bar{v}_{RMS}, \tag{5.24}$$

$$\Gamma_\eta = \eta\frac{1}{4}n_0\bar{v}_{RMS}. \tag{5.25}$$

This is an appropriate calculation for determining the number of particles arriving at the pellet surface but the quantity that determines ablation is the energy flux, Γ_E, not the

number flux. This quantity is determined by summing the energy contribution from each energy bin that arrives at the pellet surface over all energies,

$$\Gamma_E = \sum_{j=0}^{N} E_i \bar{f}_j \frac{1}{4} n_0 \bar{v}_{RMS}, \tag{5.26}$$

where E_j is the energy of the particle at the pellet's surface and $\bar{f}_j$ is the fraction of the distribution associated with that energy. This quantity is significant in calculating the ablation of the surface.

5.1.6 Calculation of Resultant Ablation

The quantity previously calculated was a flux density with units of $\mathrm{eVm}^{-2}\mathrm{s}^{-1}$. To calculate the energy arriving at the pellet's surface will require a time interval and an area which will be the timestep associated with the simulation and the projection of the surface area of the pellet at the current time. The energy imparted to the pellet by the transmitted electrons is given in equation 5.27:

$$E_p = \Gamma_E 4\pi r_p^2 \Delta t. \tag{5.27}$$

Ablation of the solid pellet will result in the release of molecules of deuterium from the solid structure. The energy needed to release a single molecule can be calculated from the addition of the enthalpy of fusion and vaporisation which is $\Theta = 5.27\mathrm{meV}$. The number of particles released can then be calculated by simply taking the ratio of these quantities (as in equation 5.28) and the ablation rate approximated using equation 5.29,

$$N_A = \frac{E_p}{\Theta}, \tag{5.28}$$

$$\dot{N} = \frac{N_A}{\Delta t}. \tag{5.29}$$

Equations 5.28 and 5.29 define the number of particles released in a time Δt and the number of particles released per second respectively. These equations are just definitions but can be compared to results of models such as the NGS model (Parks and Turnbull (1977)) and other experiments. This is how this thesis will determine the key quantity in

pellet-injection experiments.

5.1.7 Calculation of System Parameters for Next Iteration

If a constant density is assumed for the solid state, which is normal, then a loss of particles can be readily and easily equated to a smaller pellet size. In the following equations the superscripts on the N terms relate to pre- and post-ablation for a single iteration of the scheme outlined in section 5.1. Similarly, the subscript i on the r_p refers to the value for the current iteration of the scheme.

$$N_i^{\text{pre}} = \frac{4}{3}\pi\rho_0 r_{p,i}^3, \tag{5.30}$$

$$N_{i+1}^{\text{post}} = N_i^{\text{pre}} - N_A, \tag{5.31}$$

$$r_{p,i+1} = \left(\frac{3}{4\pi\rho_0} N_{i+1}^{\text{post}}\right)^{\frac{1}{3}}. \tag{5.32}$$

This new r_p will correspond to a new r_c and a density profile can be established for the new parameters. Of course, if r_p is small enough, then the simulation will stop as the pellet will be effectively fully ablated. Otherwise the new set of parameters will form the quasi-equilibrium state for the next iteration of injected electrons but some additional physics must be addressed to form a more self-consistent and robust experiment. Following this step, the total lifetime of the pellet in real units advances by the Δt associated with the incoming flux of particles. This is one of the key quantities to be investigated in this experiment. Non-dimensionally, this system of equations may be expressed as:

$$\tilde{\Gamma}_\eta = \eta\tilde{n} \tag{5.33}$$

$$\tilde{\Gamma}_E = \sum_{i=0}^{N} k_i \tilde{E}_i \tilde{n} \tag{5.34}$$

$$\tilde{E} = \tilde{\Gamma}\tilde{r}_p^2 \Delta\tilde{t} \tag{5.35}$$

$$\tilde{N}_A = \tilde{E} \tag{5.36}$$

$$\tilde{N}^{\text{post}} = \tilde{N}^{\text{pre}} - \tilde{N}_A \tag{5.37}$$

$$\tilde{r}_p = \left(\tilde{N}^{\text{post}}\right)^{\frac{1}{3}} \tag{5.38}$$

where the scaling quantities are defined as: [1]

$$\hat{\Gamma}_\eta = \frac{1}{4} n_0 v_{th}, \tag{5.39}$$

$$\hat{\Gamma}_E = \hat{\Gamma} \tau_e, \tag{5.40}$$

$$\hat{E} = \hat{\Gamma}_E 4\pi r_0^2 t_f, \tag{5.41}$$

$$\hat{N}_A = \frac{\hat{E}}{\theta}, \qquad \dagger \tag{5.42}$$

$$N_0 = \frac{4}{3}\pi \rho_0 r_0^3, \qquad \ddagger \tag{5.43}$$

$$r_0 = \left(\frac{3\rho_0 N_0}{4\pi} \right)^{\frac{1}{3}}, \tag{5.44}$$

for the bond energy of H_2, θ, and rest mass energy of the electron, τ_e. These quantities combine in such a way that,

$$A = \hat{A}\tilde{A}, \tag{5.45}$$

or

$$A = A_0 \tilde{A}, \tag{5.46}$$

for a dimensional quantity A, non-dimensional quantity $\tilde{A}$ and a dimensional scaling quantity $\hat{A}$ or A_0.

5.1.8 Transport

The previous work in this chapter has illustrated the method used to stop electrons in a single timestep but this is a time-dependent system and will evolve. As has been made clear in chapter 4 the pellet radius, cloud radius, and density profile will evolve in time and they are known analytically at each point in space and time. These can be used to track the flow of material between timesteps and to allow an examination of the time-evolution of certain quantities such as the electron density, n_e, and the electric potential, ϕ, by

[1] The two symbols † and ‡ correspond to the two diffferent scalings for particle numbers here. The † symbol relates to the number of particles arriving at the pellet based on its initial size which scales the ablation. ‡ is the scaling according to the number of particles in the pellet at time $t = 0$ and creates an intuitive relationship between the number of particles released in a wave of ablation and the size of the pellet. $\tilde{N}_A$ will be scaled, initially, by $\hat{N}_A$ as is natural given the preceding equations but will be then multiplied by $\frac{\hat{N}_A}{N_0}$ to arrive in a set of non-dimensional variables that are both common and natural for the remaining terms.

understanding the velocity profile, $u(r,t)$ of the neutrals in the cloud. This is done by examining the first of Euler's equations:

$$\dot{\rho} + \nabla \cdot (\rho u) = \alpha(r,t), \tag{5.47}$$

for a source term, $\alpha(r,t)$. Generally speaking, this equation can be integrated indefinitely in space but within r_p and r_c where it is defined to yield an equation for the velocity profile and the discussion is now restricted to one-dimensional variation in the quantities,

$$\rho u = \int \Big(\alpha(r,t) - \dot{\rho}\Big) \mathrm{d}r. \tag{5.48}$$

Before considering what the limits on the integral should be, the form of α should be better understood. This is a source function for particles in the cloud of which there is only one - the pellet. Assuming only a uniformly distributed amount of mass is lost from the pellet, it can be said that all matter released is sourced from $r = r_p$ and $\alpha(r \neq r_p, t) = 0$ otherwise. This is a delta function centred on $r = r_p(t)$ with some multiplicative factor to scale the ablation in time. With this established, it is useful to capture this source of material in the integral but also to develop a general formula for $u(,r,t)$. Therefore a lower limit of $r = r_p$ is chosen with an upper limit of r. Equation 5.48 then becomes

$$\rho u = \int_{r_p}^{r} \Big(\alpha_0(t)\delta(r - r_p) - \dot{\rho}\Big) \mathrm{d}r. \tag{5.49}$$

The source term here has been replaced by a scaled delta function,

$$\alpha(r,t) = \alpha_0(t)\delta\Big(r - r_p\Big), \tag{5.50}$$

which is non-zero at precisely one point because the only source of material in this system is at the pellet's surface. Returning to equation 5.49, the integration of the source term is trivial but the density term requires some more work before the integral may be evaluated. Recall, the density profile provided in chapter 4 is

$$\rho(r,t) = \epsilon \frac{1 + r_p^2(t)}{1 + r^2}. \tag{5.51}$$

The time derivative is therefore

$$\dot{\rho} = \frac{2\epsilon \dot{r}_p r_p}{1 + r^2}, \tag{5.52}$$

and the indefinite integral over r is

$$\int \dot{\rho} \mathrm{d}r = 2\epsilon \dot{r}_p r_p \tan^{-1}(r). \tag{5.53}$$

The evaluation of the integral in equation 5.49 is

$$\rho(r,t)u(r,t) = \alpha_0(t) - 2\epsilon \dot{r}_p r_p \left(\tan^{-1}\left(r\right) - \tan^{-1}\left(r_p\right) \right). \tag{5.54}$$

This is a perfectly valid evaluation of the integral. However, the evaporative model informs all of the key quantities in time and space where it is relevant. Therefore we could comfortably substitute in values for $r = r_c$ and $u(r_c,t) = \dot{r}_c$ into equation 5.54 to obtain an expression for $\tan^{-1}(r_p)$,

$$\begin{aligned} \rho(r_c,t)\dot{r}_c(t) &= \alpha_0 - 2\epsilon \dot{r}_p r_p \left(\tan^{-1}\left(r_c\right) - \tan\left(r_p\right) \right), \\ \implies \tan^{-1}\left(r_p\right) &= \frac{\rho(r_c,t)\dot{r}_c - \alpha_0(t)}{2\epsilon \dot{r}_p r_p} - \tan^{-1}\left(r_c\right). \end{aligned} \tag{5.55}$$

Substituting equation 5.55 into equation 5.54 yields equation 5.56,

$$\rho(r,t)u(r,t) = \rho(r_c,t)u(r_c,t) - 2\epsilon \dot{r}_p r_p \left(\tan^{-1}\left(r\right) + \tan^{-1}\left(r_c\right) \right). \tag{5.56}$$

Equation 5.56 captures the change in neutral particle velocity with space and time over the whole spatial range of the cloud. Therefore, if a point in the cloud r is transported over a time Δt then its new coordinate is,

$$r(t_2) = r(t_1) + u(r,t_1)\Delta t. \tag{5.57}$$

This has been graphically represented in figure 5.6.

The question of how the mass becomes redistributed due to this transport is a separate issue but upon looking at the nature of the density profile a path to a solution can be found. From figure 4.6 it can be seen that for points common to two distinct times t_1 and t_2, that the density profiles is monotonically decreasing. An interesting question to ask is how much of that density remains and how much is lost to some other point. If two

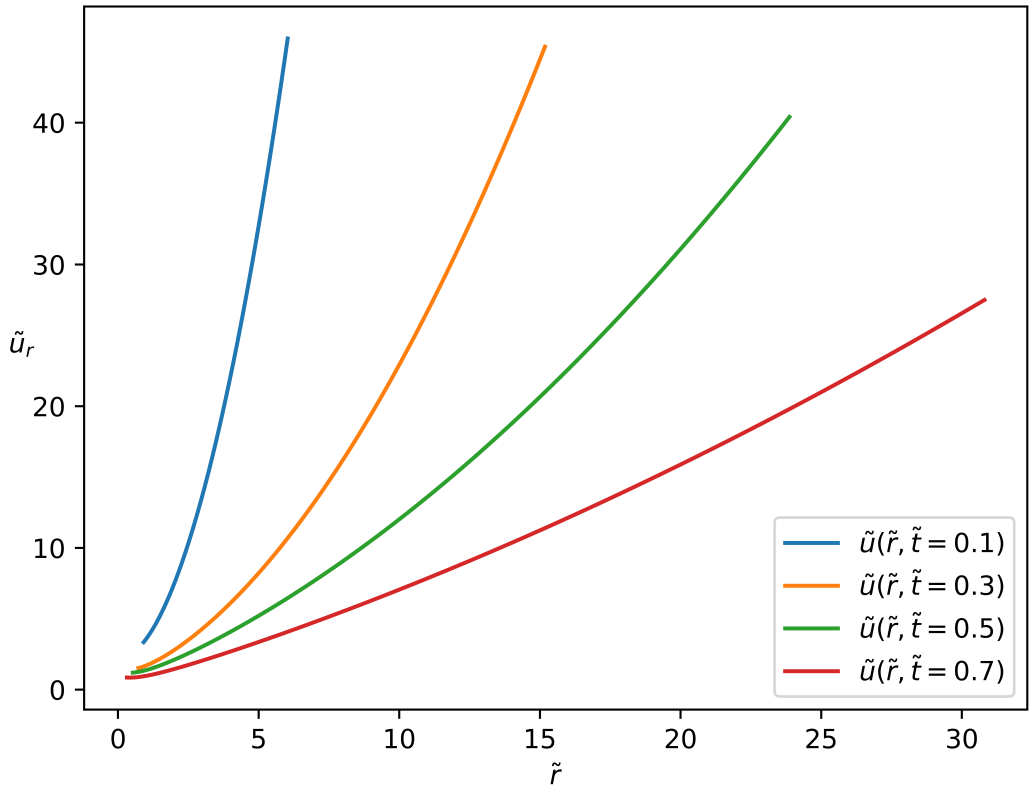

Figure 5.6: The velocity profile, $u(r)$, illustrated for various times determined by solving equation 5.56.

density profiles evaluated at the same spatial point r for those two distinct times, their ratio may be expressed as,

$$\begin{aligned} \frac{\rho(r,t_2)}{\rho(r,t_1)} &= \frac{\epsilon\frac{1+r^2(t_2)}{1+r^2}}{\epsilon\frac{1+r_p^2(t_1)}{1+r^2}}, \\ &= \frac{1+r_p^2(t_2)}{1+r_p^2(t_1)}, \end{aligned} \tag{5.58}$$

which is a number always less than 1 because $r_p(t_2) < r_p(t_1)$ if $t_1 < t_2$. Therefore the fraction of particles that remain at a point r across a timestep $\Delta t = t_2 - t_1$ is given by this ratio. The fraction of particles that remain at r, f_r and that are lost from r, f_l, are given

as

$$f_r = \frac{1+r_p^2(t_2)}{1+r_p^2(t_1)}, \tag{5.59}$$

$$\begin{aligned} f_l &= 1 - f_r, \\ &= \frac{r_p^2(t_2)}{1+r_p^2(t_1)}. \end{aligned} \tag{5.60}$$

These fractional terms relate only to the set of points in r that is common to both clouds at times t_1 and t_2 which includes the values of r in $r_p(t_1) + u(r_p, t_1)\Delta t < r < r_c(t_1)$. Outside these boundaries the cloud either only loses or gains material as there are no common points for the competition of losses and gains to take place.

$$\begin{aligned} \rho_{1\to2}(r, t_{1\to2}) &= f_r \rho(r, t_1) && r < r_p(t_1) + u\Big(r_p(t_1)\Big)\Delta t \\ \rho_{1\to2}(r, t_{1\to2}) &= f_r \rho(r, t_1) + f_l \rho(r_1, t_1) && r_p(t_1) + u\Big(r_p(t_1)\Big)\Delta t < r < r_c(t_1) \\ \rho_{1\to2}(r, t_{1\to2}) &= f_l \rho(r, t_1) && r_c(t_1) < r < r_c(t_2) \end{aligned}$$

Figure 5.7 presents some initial confusion but can be understood by first examining the fractional terms f_r and f_l. For any reasonably sized time-step, $\Delta\tilde{t} \ll 1$, the remaining fraction will always be much larger than the loss fraction, $f_r \gg f_l$. The neutral profile is monotonically decreasing for varying t and constant r and varying r with a constant t,

$$\rho(r, t_1) > \rho(r, t_2) \text{ for } t_1 < t_2, \tag{5.61}$$

$$\rho(r_1, t) > \rho(r_2, t) \text{ for} r_p < r_1 < r_2 \text{ and } r_1 < r_2 < r_c. \tag{5.62}$$

This means that from a point r_1 at time t_1 there is more material transported to a point r_2 at time t_2 than is lost from point r_2 in that same interval. This gives the illusion that the density profile is continuously increasing with time but this is not true because the transport model outlined above only considers the motion of matter already in the cloud. It does not include the transport of matter released from the pellet corresponding to the change in radius $r_p(t_1)$ to $r_p(t_2)$ and the perturbation the release of material at a density 100 times larger than the neighbouring media. Additionally, the changes in the system will be much smaller in the self-consistent simulation than here where the change was selected to be visible. The staggered nature of the transported electron line, which sits under the original electron density line, is due to the pushing of the transported fraction of electrons

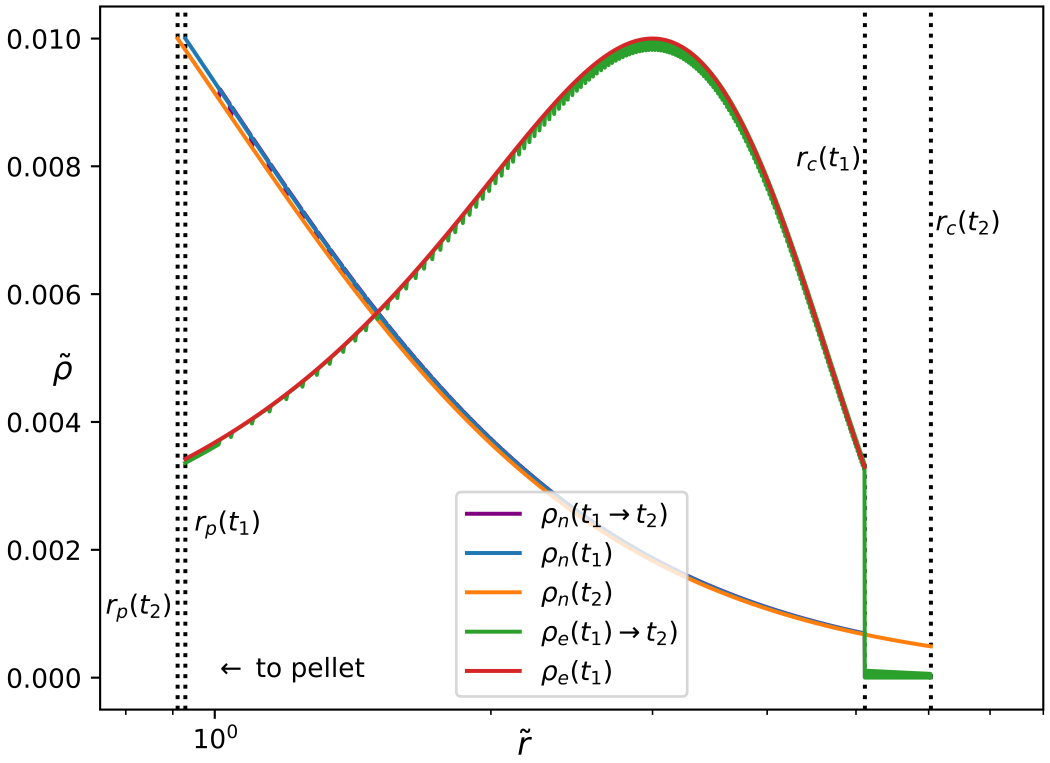

Figure 5.7: The transport of neutrals and an arbitrary distribution compared. The blue and orange lines show the equilibrium densities of neutrals at times t_1 and t_2 with the purple line showing the transport of $\rho_n(t_1)$ to the positions according to the transport model in the correct proportions defined by f_r and f_l. The red line shows the initial density distribution of charge and the green line shows the transport to t_2 according to the same model that was used to calculate the transported neutral profile (purple line). The dotted lines denote the positions of the pellet and cloud edge at times t_1 and t_2.

onto the same points as the remaining fraction of electrons. This effect would also be smaller with a smaller change in t_1 and t_2.

5.1.9 Trapped Electrons and their Potential, ϕ_c

Poisson's Equation

To determine the potential field over a space due to a known charge distribution requires the solution of Poisson's equation,

$$\nabla^2\phi = -\frac{n_c}{\epsilon_0}, \tag{5.63}$$

where n_c is the charge density, ϵ_0 is the permittivity of free space and ϕ is the potential. Equation 5.63 describes the connection of the electrostatic potential to the charge density distribution creating that potential but this can easily be reduced to a one dimensional case from the three dimensional one described,

$$\frac{\partial^2\phi}{\partial x^2} = -\frac{n_c}{\epsilon_0}. \tag{5.64}$$

This equation can be non-dimensionalised in the following way,

$$\frac{\mathrm{d}^2\tilde{\phi}}{\mathrm{d}\tilde{x}^2} = -\psi\tilde{n}, \tag{5.65}$$

where the quantities are connected by,

$$x = r_0\tilde{x} \qquad \phi = \phi_0\tilde{\phi} \tag{5.66}$$

$$q = e\tilde{q} \qquad n = n_0\tilde{n} \tag{5.67}$$

$$\psi = \frac{r_0^2 e n_0}{\epsilon_0\phi_0} \tag{5.68}$$

From the density of stopped charge calculated in the previous chapter a calculation can be carried out to identify the potential distribution throughout the cloud. However, there is no analytical form for the stopped charge, only numerical values at the associated grid-points. To solve this numerically will necessitate discretisation of this differential equation.

Discretising Poisson's Equation

The study of numerical solutions to differential equations done by approximating the differential equation using a difference formula with a difference between the two adjacent

points of h. Methods that use a constant difference, h, are called finite difference methods and can be defined in several ways, two of which are the forward difference and the backward difference,

$$y'_n \approx \frac{y_{n+1} - y_n}{h}, \tag{5.69}$$

$$y'_n \approx \frac{y_n - y_{n-1}}{h}. \tag{5.70}$$

Neither the forward difference (equation 5.69) or the backward difference (equation 5.70) are symmetric. The derivative is determined based entirely on a point in front or behind the point of interest. However, performing a similar approach for the second derivative but with two backward difference formulae applied to the first derivative, the following result is obtained,

$$y''_n = \frac{y_{n+1} - 2y_n + y_{n-1}}{h^2}, \tag{5.71}$$

which can be readily applied to any internal grid point. This also means that a matrix equation can be formed that describes the behaviour of these internal points using a so-called "stencil" formed by this discretised differential operator. For a system of N points there will be $N-2$ internal points by which an $N-2 \times N-2$ matrix can be constructed. The equation outlined in equation 5.64, now presented as matrices, is

$$\mathbf{A} \cdot \mathbf{X} = \mathbf{D}, \tag{5.72}$$

where $\mathbf{A}$ is the discretisation matrix, $\mathbf{X}$ is the array of quantities to be solved for and $\mathbf{D}$ is an array of all the known quantity needed to solve for $\mathbf{X}$. The discretisation matrix itself uses a 3-point stencil repeated across each row to arrive at a numerical approximation to the derivative as described by equation 5.71. The 3-point stencil is given by $\{1-21\}$ which acts only on the point n and the two adjacent points in one dimension. For the case of the matrix $\mathbf{A}$ this looks like:

$$\mathbf{A} = \begin{bmatrix} -2 & 1 & 0 & \cdots \\ 1 & \ddots & \ddots & \ddots \\ 0 & \ddots & \ddots & 1 \\ \vdots & \ddots & 1 & -2 \end{bmatrix} \tag{5.73}$$

With this in mind, it is possible now to write the matrix equations which describes a discretised Poisson equation which can be readily integrated numerically.

$$\begin{bmatrix} -2 & 1 & 0 & \cdots \\ 1 & \ddots & \ddots & \ddots \\ 0 & \ddots & \ddots & 1 \\ \vdots & \ddots & 1 & -2 \end{bmatrix} \cdot \begin{bmatrix} \phi_1 \\ \phi_2 \\ \vdots \\ \phi_{N-1} \end{bmatrix} = \frac{1}{\epsilon_0} \begin{bmatrix} n_1 \\ n_2 \\ \vdots \\ n_{N-1} \end{bmatrix} \tag{5.74}$$

Fundamentally, the calculation here is to find the inverse of the matrix **A**, multiply on the left by it and right hand side of equation 5.72 yields the array of quantities to be solved for. For small grid separations, the matrices can have very large sizes which makes the task unwieldy analytically and a common inversion algorithms available as a standard in most programming languages become significantly slower than alternative methods when systems of multiple dimensions are simulated. In solving an equation such as equation 5.72 there are a number of methods that can be used to solve such an equation but iterative methods are simple ones. Iterative methods are easily implemented but come with the time-consuming iterative corrections that give them their name.

Iterative methods

The algorithm operates as follows.

1. An initial guess is made for each interior point not defined by the boundary conditions, often a simple guess such as $x_i = 0$.

2. The matrix equation as defined by equation 5.74 is solved line by line by considering the first interior grid point.

3. The initial guess is then corrected by re-arranging one of the linear algebraic equations for x_i. This correction improves the accuracy of the solution.

4. The solver proceeds to the adjacent point moving across the grid and the same process is applied, correcting the solution to the next point and so on across the entire domain.

5. After an initial pass of the domain, the solver verifies that the correction applied meets an error criterion specified by the user. If the correction is too large, another pass is made to improve the result further.

6. Iterations continue until the error criterion is satisfied.

For a general system as described by equation 5.72, this can be represented more explicitly as:

$$\begin{aligned} a_{11}x_1 + a_{12}x_2 + a_{13}x_3 + \ldots a_{1N-1}x_{N-1} &= d_1, \\ a_{21}x_1 + a_{22}x_2 + a_{23}x_3 + \ldots a_{2N-1}x_{N-1} &= d_2, \\ &\vdots \\ a_{N-11}x_1 + a_{N-12}x_2 + a_{N-13}x_3 + \ldots a_{N-1N-1}x_{N-1} &= d_{N-1}. \end{aligned}$$

Supposing the iterative method described above is applied here for the jth term for an iteration number k,

$$x_j^{k+1} = \frac{1}{a_{jj}}\left(d_j - \sum_{i=1}^{N-1} a_{ji}x_i + a_{jj}x_j^k\right). \tag{5.75}$$

The initial guess for all x_i can be substituted into the right hand side for the $k = 0$ iteration. Equation 5.75 makes it easier to see that the iterative method finds the correct solution by subtracting the guessed solution from the actual solution and using that difference to correct the approximation. Corrections become smaller as the iteration number k increases until a prescribed point whereupon the corrected solutions are sufficiently close to the actual solution. These methods are time-consuming due to the large number of iterations needed for an acceptable solution however, for differential equations the matrix $\mathbf{A}$ is sparsely populated with non-zero entries. This can make the calculation less computationally intensive for an intelligently designed solver. The method described in equation 5.75 is the *Jacobi* method. There is a simple improvement to be made to this method. Instead of completing an entire iteration over all x_i before updating the values, the values can be updated within an iteration to improve the results of later x_i. This is called the *Gauss-Seidel* method and the x_i's are evaluated as in equation 5.76,

$$x_j^{k+1} = \frac{1}{a_{jj}}\left(d_j - \sum_{i=1}^{j-1} a_{ji}x_i^{k+1} - \sum_{i=j+1}^{N-1} a_{ji}x_i^k\right). \tag{5.76}$$

This is faster than the Jacobi method but can improved even more by means of a *relaxation parameter* which can accelerate or decelerate the convergence of the x_i's to the solution. The relaxation parameter, ω, has a range of values between 0 and 2. When $\omega = 1$ the method returns to Gauss-Seidel but for $1 < \omega < 2$ the solution is arrived at more quickly. However, there are two caveats to this improvement. For $\omega > 2$ the method is unstable and the solution will oscillate about the true solution, continually overstepping the desired value. Additionally, for some problems this upper limit on ω may be less than 2 and care must be taken to guarantee that the solution achieved is correct. When a relaxation parameter is used with a value greater than but not equal to 1 then the method is termed *successive over-relaxation* or SOR. This method is illustrated for a single x_j in equation 5.77,

$$x_j^{k+1} = (1-\omega)x_j^k + \frac{\omega}{a_{jj}}\left(d_j - \sum_{i=1}^{j-1} a_{ji}x_i^{k+1} - \sum_{i=j+1}^{N-1} a_{ji}x_i^k\right). \tag{5.77}$$

Validation of solver

To verify the efficacy of the solver, a variety of test cases were used, some of which are collectively presented in figure 5.8 where $\tilde{\rho}_c = \tilde{q}\tilde{n}$. These test cases are all analytically soluble yielding the potential profiles,

$$\tilde{\phi} = \tilde{x}, \tag{5.78}$$

$$\tilde{\phi} = \frac{\tilde{x}}{2}\left(1-\tilde{x}\right), \tag{5.79}$$

$$\tilde{\phi} = -\frac{\tilde{x}^4}{4} + \frac{\tilde{x}^3}{3} - \frac{\tilde{x}}{12}, \tag{5.80}$$

$$\tilde{\phi} = 1 - \mathrm{e}^{\tilde{x}}\left(\frac{10-9\mathrm{e}}{10\mathrm{e}}\right)\tilde{x}, \tag{5.81}$$

when moving clockwise from the top-left panel. This SOR method will be applied to the system to determine the potential field inside the cloud based on the distribution of charge due to the stopping and the differential motion of the cloud expansion. Incorporating the electron potential into the calculation is now possible but the expected deviations from the purely neutral CSDA results should be understood before undertaking any self-consistent simulations. It is important to note there that this is a 1-D solution to the problem and neglects the radial contribution to the potential arising from any radial variation in the

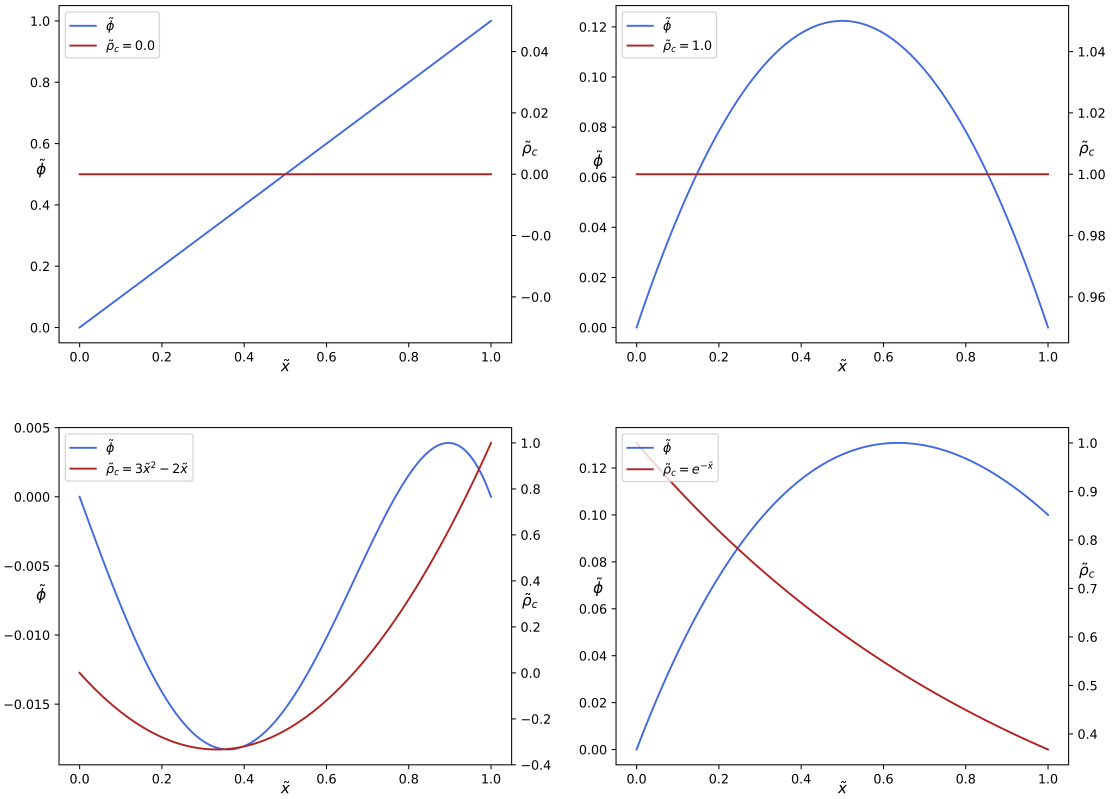

Figure 5.8: A series of iterative solutions to Poisson's equation for a variety of test charge distributions using the SOR algorithm designed for the pellet simulation. Top left: no charge density, with fixed potential difference at the domain edges. Top right: Constant charge density with no potential difference at the domain edges. Bottom left: Polynomial charge density with a potential difference at the domain edges. Bottom right:Exponentially decaying charge density with a potential difference at the domain edges.

CSDA implementation. This 1-D solution is justified by the strong magnetic field that rigidly aligns the electrons to that axis but to truly capture the interplay of the different spatial dimensions will require a more thorough approach.

5.2 The Influence of a Potential from Trapped Electrons

In order to assess the difference that the electrostatic potential will bring to the problem a few test cases with a variety of known potential profiles should be produced. While it

would be almost impossible to discern the unique influence that the electrostatic potential has over the distribution of particles due to the intertwined nature of electrostatic losses and the growing dominance of CSDA it may be possible to pick out particular features and explain them in a general manner. The profile is expected to be peaked (perhaps multiply-peaked) and fixed at boundaries so a similar approach will be taken in the tests with a gaussian potential and variety of peak potentials and standard deviations on the width, centred on the centre of the cloud. This leads to a number of different parameters to work through to examine their effects: namely the standard deviation, σ; the strength of the test potential, ϕ_t; and the centre of the gaussian, x_0. Before we turn to examining the effects of these parameters in turn, a prediction should be made on these things based on what is already known about the influence of a potential on a charged particle. The simplest statement to make is that the absolute value of the potential will not affect the output but the potential difference across any two points will. So if an electron moves from one point to another and encounters a potential difference of, say, -10V then its energy will *fall* by 10eV. For a gaussian distribution of negative potential centred on the centre of the cloud this is how electrons will be affected initially. However, this is only half the story. For particles that are energetic enough to withstand the losses due to the potential and its combination with CSDA they will find that the potential difference across that same step (mirrored along the centre of the cloud) will be $+10$V and its energy will *increase* by 10eV. These electrostatic losses and gains must be coupled with the effects of CSDA which become more influential as the particle traverses the cloud which becomes more dense owing to the density profile defined in chapter 4 and also as the particle loses energy. This means that a change of 10eV in particle energy will have a more significant effect on a 5keV electron at the pellet-cloud interface than at the cloud-plasma interface. Similarly, any change in electron energy due to the potential will have a greater effect on a 50eV particle than a 5keV particle. To make this clearer, please refer to the results contained in chapter 3.1.1. This information is vital to interpreting the figures that follow.

A Linear Potential

The effects of this potential on the stopping of electrons are illustrated in figures 5.9 and 5.10. The density of the electrons increases as the retarding potential increases which is what would be expected - the energy threshold for each step is effectively raised and so more electrons will fail to meet this threshold. Consequently more electrons are stopped

at earlier points and the density profile becomes more peaked as is observed in figure 5.9. The minimum initial energy required to fully traverse the cloud is also shown to increase readily with an increase in retarding potential. Notably, a potential of 1keV raises the threshold by about 1keV and similarly so for 2keV and 3keV. The staggered nature to the line in figure 5.10 is due to the potential resolution which if increased capture the stopping more precisely. Despite the discrete sctructure of the plot, it is clear that increasing the retarding potential also increases the minimum energy required to traverse the cloud.
An important comment to make is that the variation in stopping potential is not precisely reflected in the change in ϑ. For example, with infinitely precise energy bins, a linear potential of 100V should stop an additional 100eV of charge as would also be expected for 2kV and 2keV of charge. This is not observed from figure 5.4 and it is due to the unique interplay of CSDA and the particle energy. The minimum traversal energy at a given time with no linear retarding potential, ϑ_0, will be the minimum possible traversal energy and will only increase for an increasing retarding potential, ϑ_ϕ. If this retarding potential is 2kV, for example, then it would be expected that $\vartheta_\phi = \vartheta_0 + 2\text{keV}$. However, because the particle energy of interest is now 2keV greater, CSDA is now weaker and consequently the particle retains more of its energy on its way across the cloud. There is therefore an opportunity now for a particle sitting in the energy range $\vartheta_0 < \vartheta_\phi < \vartheta_0 + 2\text{keV}$ to be the actual minimum traversal energy for the particular configuration. This inequality is always satisfied upon looking at figure 5.10.

5.2.1 A Gaussian Potential

A more interesting potential to consider is a curve with a defined peak - notably a gaussian profile,

$$\phi = \phi_0 \exp\left(- \frac{(x - x_0)^2}{2\sigma^2} \right). \tag{5.82}$$

Testing this profile yields a number of more interesting results which should bear more relevance to a profile determined by the stopped electrons. The influence over the CSDA solution is shown through the stopped densities of electrons in the cloud in figures 5.11 - 5.16 and summarised in figure 5.17. It is important to remember before reading further that for this particular problem the CSDA is not solely a function of particle energy but also of the target density ρ.

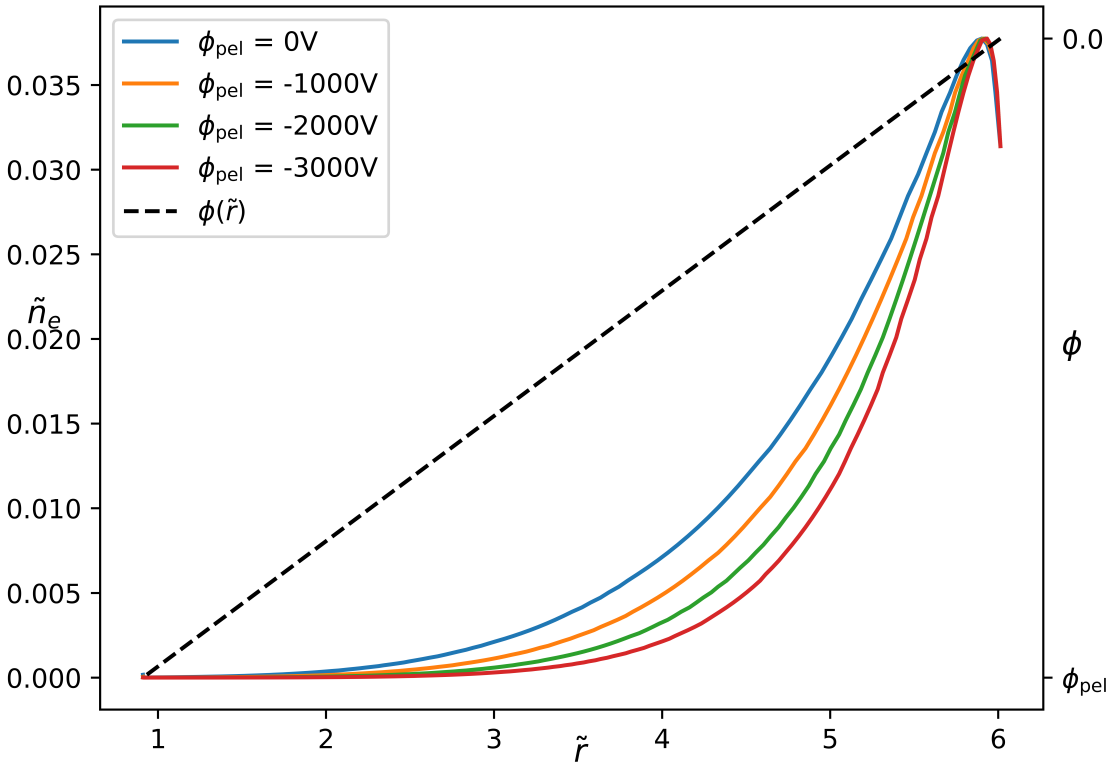

Figure 5.9: The density of the stopped electrons across the cloud for several different potentials on the pellet surface at time $\tilde{t} = 0.16$ which linearly increase from the value in the legend at $\tilde{r}_p \approx 0$ to 0V at $\tilde{r}_p \approx 8$.

Effect of Varying the Depth of the Potential

The most obvious parameter to vary is the magnitude of the potential loss, or the height of the gaussian that represents a potential profile denoted by ϕ_t. The effect on the distribution of bins (as a proxy for density) has been presented in figure 5.11. Looking at the cloud-plasma interface we see that the least energetic particles suffer small changes to the purely CSDA calculation with particles only stopping marginally sooner than without the potential. It is comforting to note that as the potential increases particles do stop sooner i.e. that a greater potential penalty corresponds to a lower energy of particles. In fact, any particle should see a greater energy loss across a given step than without the potential and so stop "sooner". This effect is most pronounced in the region surrounding

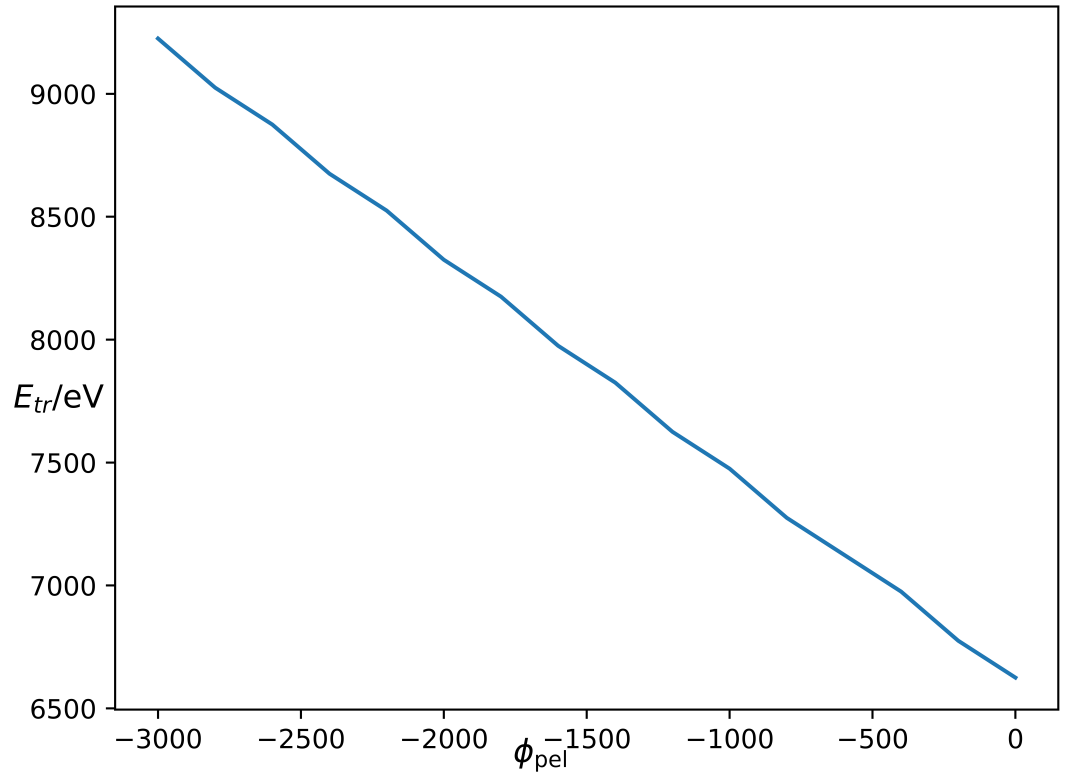

Figure 5.10: The minimum initial energy required to fully traverse the cloud at time $\tilde{t} = 0.16$ as a function of the potential on the pellet's surface which increases in a linear fashion to 0V at r_c. The effect of CSDA is now masked by the increasing potential which has a more pronounced effect but can be identified by the absence of a $1:1$ dependance of the minimum traversal energy on the retarding potential. The CSDA here is weaker at greater particle energies and will slow those particles less efficiently.

the peak of the potential where the maximal energy penalty has been applied and CSDA will have a its greatest enhancement due to the potential. Of course, the combination of these effects is cumulative and particles that *would* stop at the potential peak stop *before* they have reached it. This creates the largest disparity between the purely CSDA simulation and the combined CSDA and electrostatic simulation.

Finally, there are the particles that pass through the potential peak and receive an energy boost. One might expect the particle to recover its trajectory however the magnified energy losses due to CSDA are not regained. Instead, they have undergone greater CSDA losses after the ϕ_teV penalty from the potential which can not be reclaimed by the subsequent

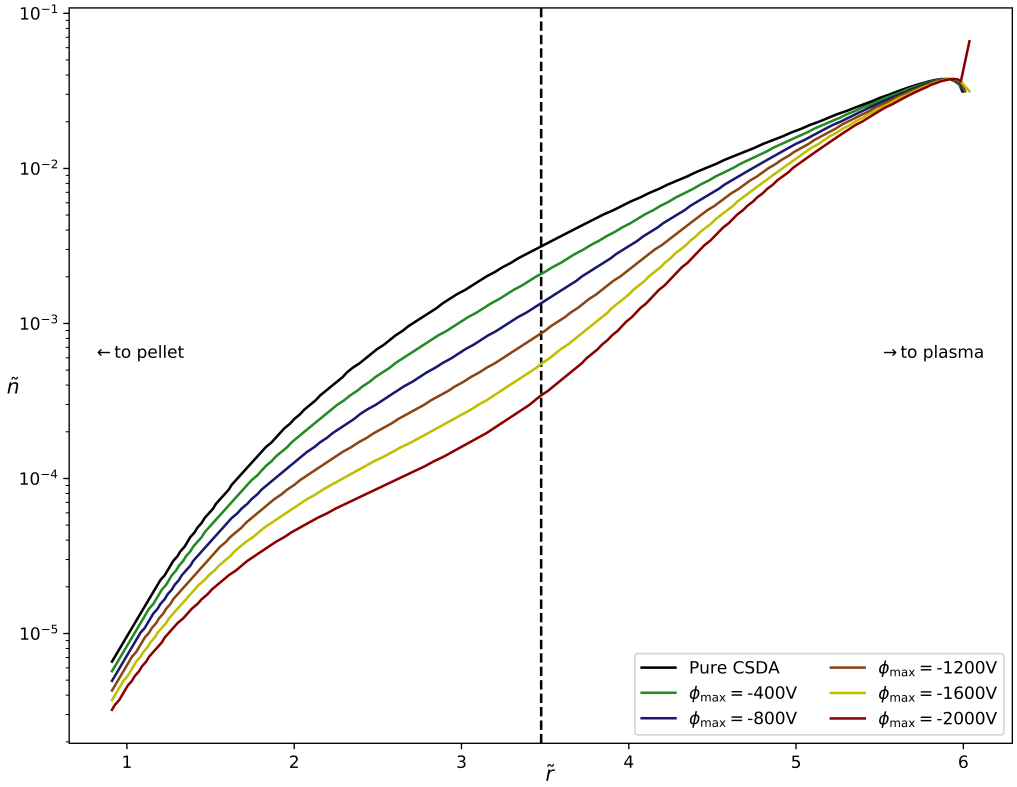

Figure 5.11: The EEDF bin varying with position in the cloud for a variety of peak stopping potentials with a standard deviation of $\tilde{\sigma} = 1$. The dashed vertical line in the figure indicates the position of the gaussian centre.

energy enhancement. This creates a permanent separation from the pure CSDA calculation and ultimately a lower energy flux at the pellet surface. The energy flux may be recovered should there be a net positive potential region just before the pellet but for a gaussian case this will not happen and there is no guarantee that the spatial distribution of electrons could be recovered. This is a common thread through all the presented lines excluding the one diversion from this in the -2000V potential at the cloud-plasma interface but this can be explained. What is happening here is that the two least energetic bins are in fact stopping at the same point and therefore their bins are added at that spatial coordinate, creating the apparently anomalous result.

Figure 5.12 presents the initial electron energy on the y-axis against the point at which

it stops on the x-axis. The purely CSDA line (given in black) shows that as the energy increases, the electrons get farther into the cloud. Once the minimum traversal energy is reached all electrons of greater energy also reach the pellet - this is represented by the vertical lines at $\tilde{r} = 0$. Considering the other lines in the figure it can be seen that initially (at $\tilde{r} \approx 6$) the trajectory is relatively unaffected but as the minimum in the potential is approached the trajectories separate. Once the energy enhancement gets significantly small in the wings of the gaussian potential the lines become closer but never become cospatial with the lines corresponding to a lower minimum potential sitting higher on the y-axis. At this end of the x-axis the cumulative effect of the shielding can be seen with the ultimate influence of the potential on the flux seen here in the minimum traversal energy.

Effect of Varying the Width of the Potential

The effect of a varying standard deviation is perhaps more nuanced. For a given test potential and an increasing standard deviation on the profile the potential "spreads out" farther and affects the particles at the extremities of the domain. However, the potential difference (due to the finite limit on the potential) across each space-step is smaller and thus has a smaller effect on the stopping of the particle. The cummulative effect is more important here because a loss, even small, at an earlier stage in a particle's path will cause greater losses at later points because of the increasing effect of CSDA with decreasing energy meaning it begins a compounding effect for the particle. This combination is seen in figure 5.13 where the lines corresponding to the broader gaussians sit below the narrower gaussian lines (noticeably at $\tilde{r} \approx 5$) and always remain in that configuration because even if energy is recovered on the far side of the gaussian peak, the losses from CSDA are permanent. It can also be seen from figure 5.13 that as the profile becomes more peaked (σ gets smaller) there is a more abrupt departure from the pure CSDA profile. As the potential gets broader, the influence commences earlier so that the curvature of the gaussian becomes less noticeable and a constant potential difference across a space-step is approximated in the wings. Based on the lines in figure 5.13 the effect of increasing the standard deviation appears to tend towards a limit quickly, implying that the effect of the standard deviation is not as severe as the minimum potential. Of course, there is an argument to be made that a broad enough range of values have not been tested but this is limited at each extreme. First of all, decreasing the standard deviation would begin to approximate a delta function which is neither physical nor likely to be relevant to the studies of this thesis and increasing the standard deviation is limited so as to not produce a step potential at either interface

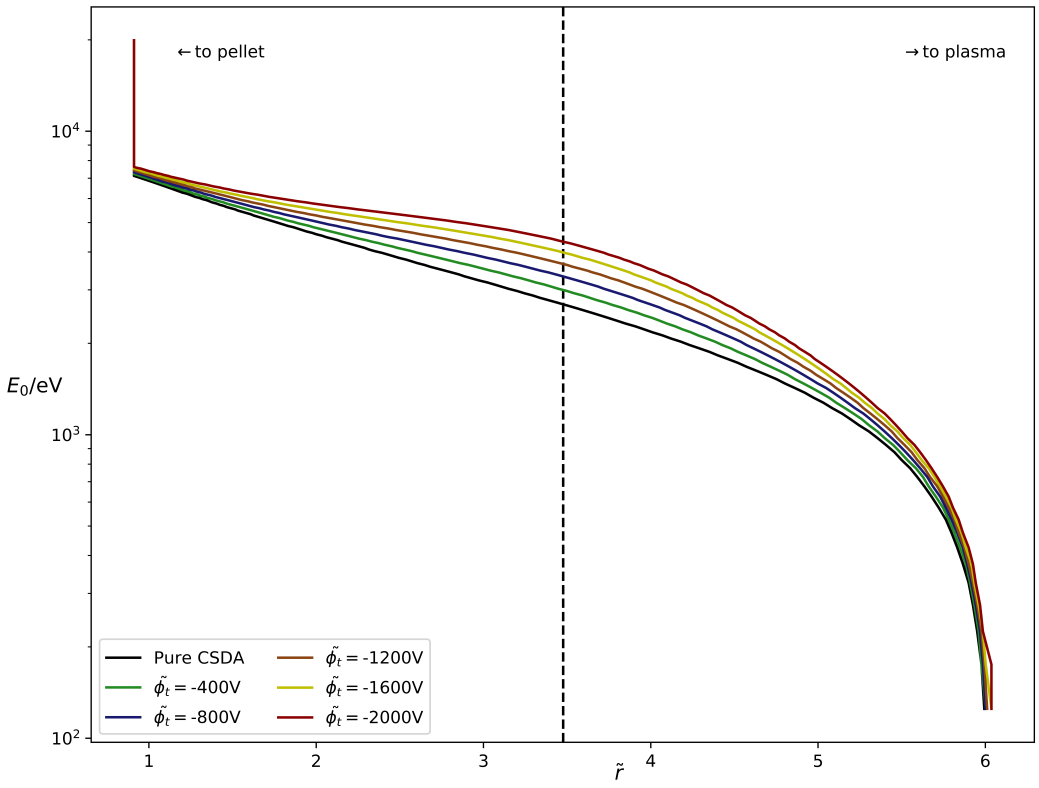

Figure 5.12: The stopping point of electrons in the cloud modelled by CSDA with a gaussian potential characterised by the initial electron energy on the y-axis and its associated stopping point on the x-axis. Each line corresponds to a different minimum potential on the gaussian aside from the black line which corresponds to a CSDA simulation with no potential. The position of the minimum potential is given by the dashed black line and its standard deviation is $\tilde{\sigma} = 1$.

which would compromise prescribed boundary conditions for the problem. It is because of these reasons that this particular parameter range has been selected and investigated for testing. The effect on the stopping point is demonstrated in figure 5.14. As with the change in potential there appears to be little divergence from the CSDA case until the minimum of the potential is approached which sees the trajectory tend towards a limiting trajectory when the standard deviation is increased. The lines then approach each other after passing the minimum value but a discernible difference remains which embodies itself

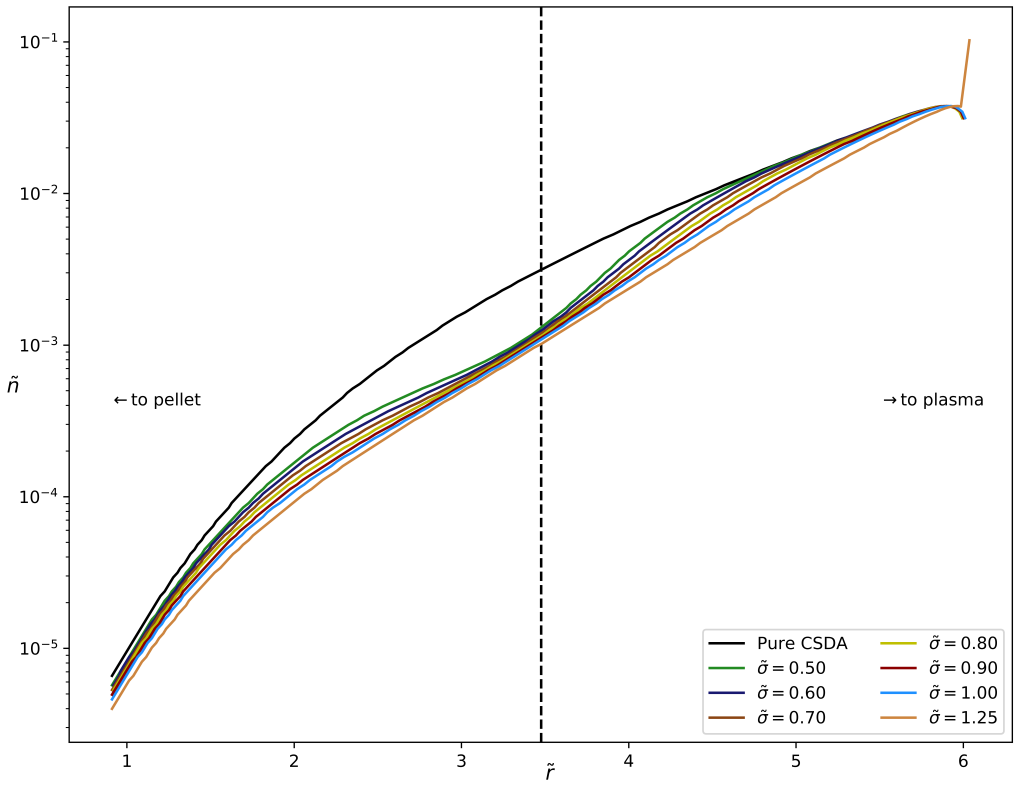

Figure 5.13: The EEDF bin as a function of position within the cloud for a variety of standard deviations on an imposed gaussian retarding potential with a minimum value of $\phi_t = -1000$V. The dashed vertical line in the figure indicates the position of the gaussian centre.

in a greater minimum traversal energy for a broader potential profile. It appears here that increasing the standard deviation infinitely would only cause the particles to stop at points which are limited by the potential which if increased infinitely would see more particles stopping near the minimum of potential.

Effect of Varying the Centre of the Potential

The position of the centre of the gaussian, and indeed the potential difference between space-steps is tremendously important. The density profile proposed in chapter 4 presents

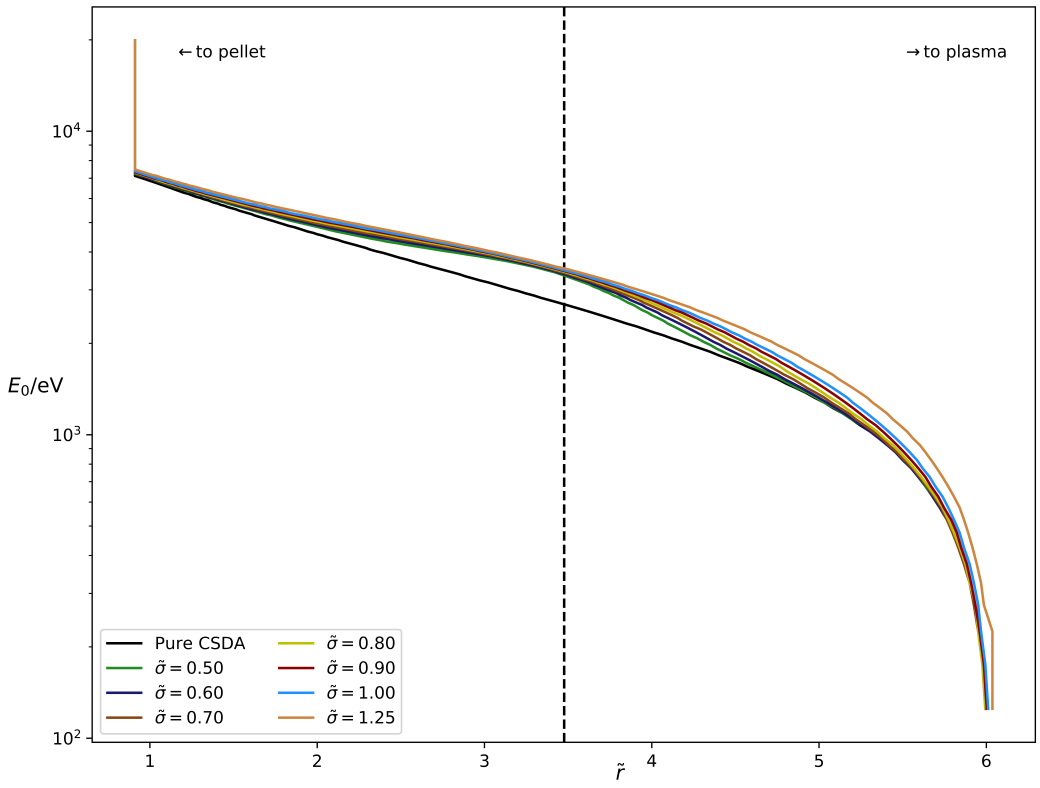

Figure 5.14: The stopping point of electrons in the cloud modelled by CSDA with a gaussian potential characterised by the initial electron energy on the y-axis and its associated stopping point on the x-axis. Each line corresponds to a different standard deviation on the gaussian aside from the black line which corresponds to a CSDA simulation with no potential. The position of the minimum potential is given by the dashed black line and its minimum value is -1000V.

orders of magnitude variation in density across the range of the cloud and therefore an order of magnitude range in the importance of CSDA. Losing 30eV in energy at the most dense portion of the cloud will cause greater slowing due to collisions than losing it in the least dense region. This is where the interplay of the energy dependence and density dependence on CSDA become connected. The significantly greater density at $r \approx r_p$ will amplify the collisional losses by at least one order of magnitude compared to a collisional loss at $r \approx r_c$. The positioning of the potential profile, therefore, bears great significance on

the final distribution of charge and is investigated in this subsection with the expectation that where the steeper region of the potential gradient is co-spacial with the more dense region of the cloud, there is to be a greater accumulation of charge due to CSDA.
From figure 5.15 we can see this expectation play out although it may be hard to discern. In a general sense, the departure from the charge-neutral CSDA simulation is greatest in the region surrounding the centre of the gaussian and tends towards that curve at distances significantly far from the centre, $\sim 2r_0$. This is what would be expected: that at the point where the energy loss due to potential is greatest would see the greatest increase in the effect of CSDA. Specifically, the curve corresponding to $\tilde{x}_0 = 1.82$ sees a significant difference between itself and the neutral CSDA curve between $\tilde{r} = 1 - 2$ and approximates the neutral case towards the plasma. Conversely, the curve corresponding to $\tilde{x}_0 = 5.23$ sees great similarity with the neutral case close to the pellet but presentes notable differences close to the plasma. The reasoning here is two-fold: the effect of the potential minimises the particle energy and then CSDA can stop more particles due to its energy-dependance but also because the maximum of the Maxwell-Boltzmann distribution is at a comparatively low energy and the effect of CSDA is strong enough to compound particle bins cospacially. This causes the straight line feature close to the plasma and accentuates the difference here.

Determining if the location of the potential stopped more particles if it is centred in the high-density region compared to what it stopped when centred in the low-density region is easier to determine by looking at the stopping point of particles as in figure 5.16. This figure indicates the stopping point of a particle based on its initial energy which makes clearer the conclusion from figure 5.15. Looking at the plasma end of the figure, it is clear with the minimum in potential closer to this edge that more particles are stopped. This is determined by how high a curve sits on the axis in this region - notably the dark red and gold lines sit higher than the others with the brown line rising above the blue and green lines looking farther left towards the centre of its associated gaussian potential. Looking now at the far left, at the pellet edge, we can see that the shielding of the pellet improves for any potential in the cloud, irrespective of its location but is greatest for a peak closer to the pellet. This rings true with the expectation that departure from the neutral CSDA model is greatest nearest the minimum in the potential but it also shows that an energy penalty close to the pellet sees CSDA become most influential in a region where the density is highest, thereby compounding its effect. This sees a significant increase in the minimum traversal energy needed to reach the pellet across the entire cloud. In the middle of the cloud, it becomes hard to discern any common behaviour. In this section of the cloud the

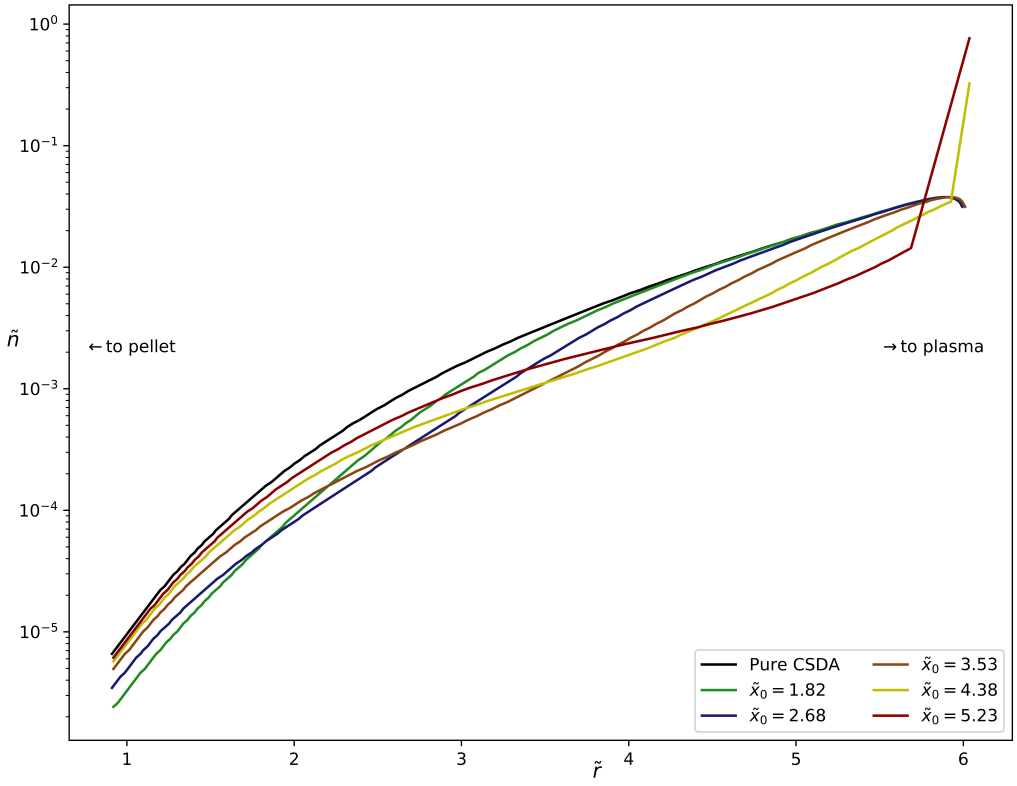

Figure 5.15: The EEDF bins as a function of position within the cloud for a variety of centre points for an imposed gaussian retarding potential with a minimum value of $\phi_t = -1000$V and standard deviation $\tilde{\sigma} = 1$.

non-linear nature of CSDA becomes apparent with many lines crossing over each other based on the location of the potential and the particle's initial energy. When coupled with the energy penalty from the electrostatic potential it becomes difficult to separate the influence of each.

Given the size of the dense region of the cloud there is a limitation on the standard deviation that can be used to investigate variation in the centre point. Consequently it becomes difficult to consider so many of these parameters together however, considering only how the deposition of charge varies with σ and ϕ_t figure 5.17 can be produced.

The take-home conclusions from these experiments can be succinctly stated as this: If the potential does not or just reaches its turning point, then the energy loss of the electrons

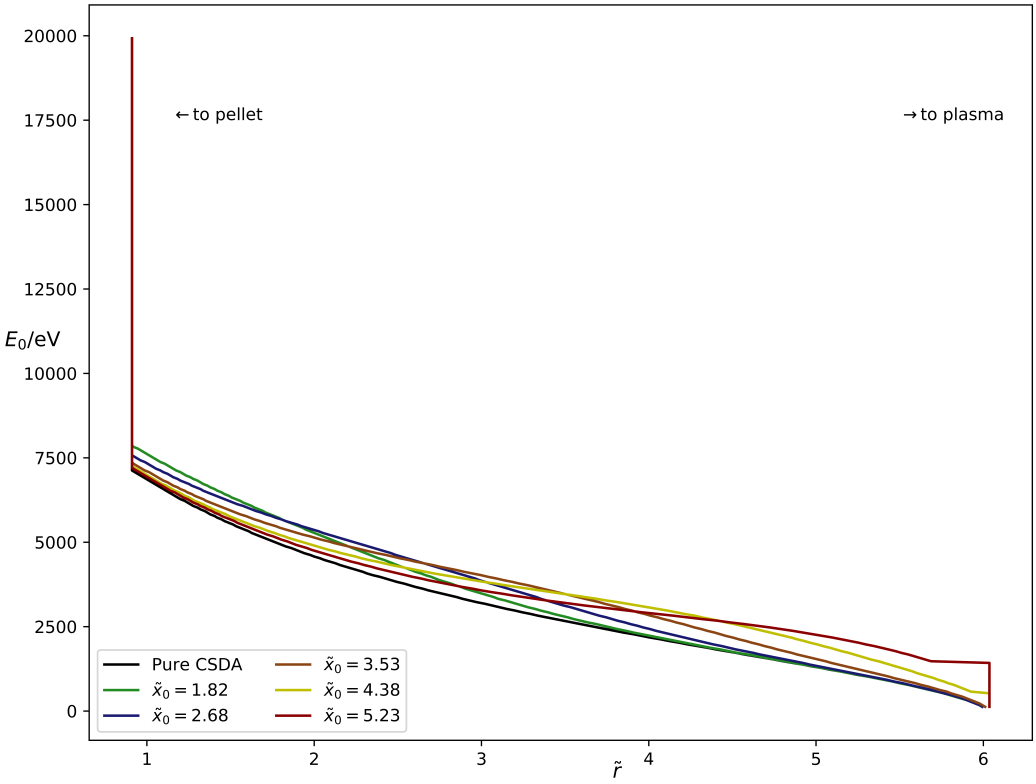

Figure 5.16: The stopping point of electrons in the cloud modelled by CSDA with a gaussian potential characterised by the initial electron energy on the y-axis and its associated stopping point on the x-axis. Each line corresponds to a different centre point of the gaussian aside from the black ine which corresponds to a CSDA simulation with no potential. The minimum value of the potential is -1000V and its standard deviation is $\tilde{\sigma} = 1$

is equal to the potential encountered but if the turning point is reached then the effect is more complicated. The general message to take from these peaked potentials is that if the potential losses occur closer to r_p then the variation between the electron density or stopping point and the pure CSDA result is greater. If the potential loss is also greater then that variation is also greater. This is because the density near r_p is greater which is where the stopping power is greatest for any given energy. Lower energy particles are more readily stopped by the neutral gas (greater stopping power) although this is naturally captured in the CSDA but when both operate in tandem, variations in the density profile

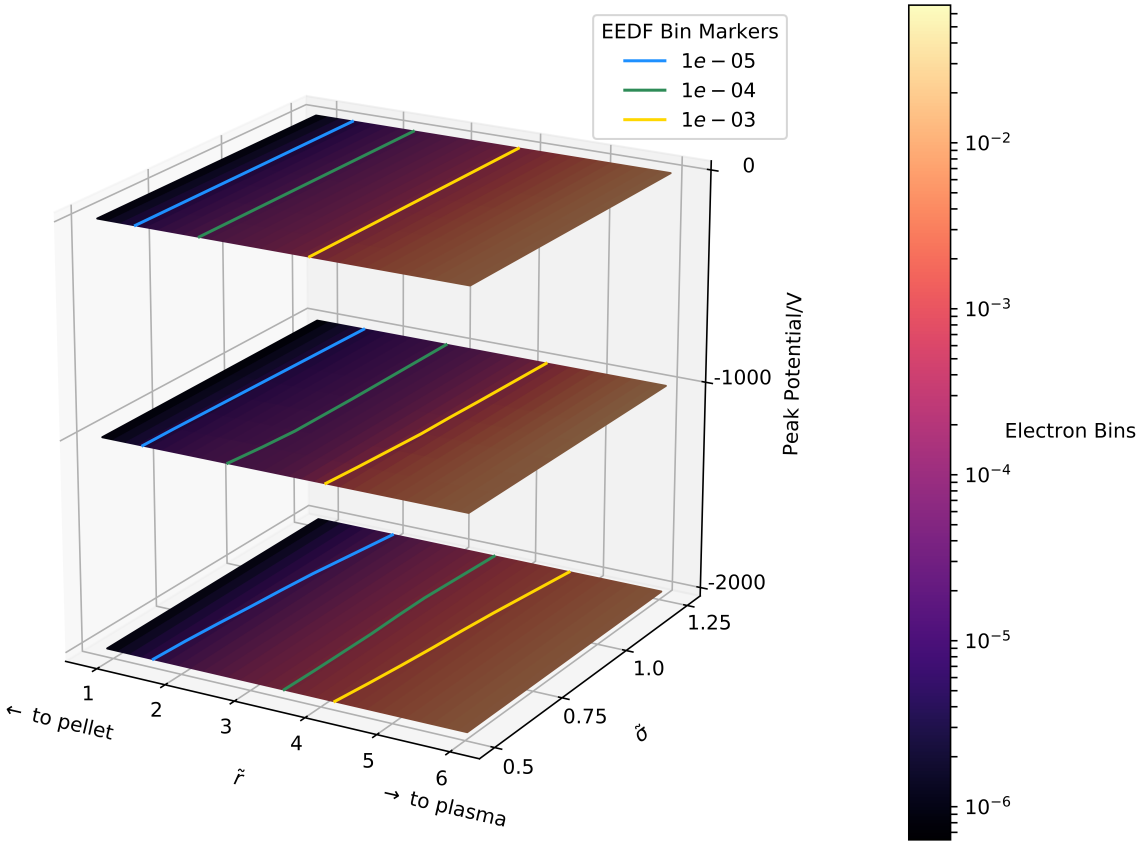

Figure 5.17: A layered image plot capturing the effect of minimum value and standard deviation of the gaussian potential on the density of stopped charge using the EEDF bins as a proxy. The coloured lines defined in the key correspond to equidense contours to aid the reader in interpreting the figure.

and minimum traversal energy are identified. These results will be useful for drawing comparisons between figures in the next chapter.

5.3 Additional Phenomena

5.3.1 Ion Ablation

In quantifying the ablation as performed by ions, a model that incorporates elements of diffusion and the energy captured by a sheath must be developed. The diffusion of ions

generated by ionising interactions must be accounted for as this will transport additional material from outside the sheath into the sheath where the ions will be accellerated by the field and impart energy to the pellet.

Diffusion

The phenomenon of diffusion is modelled via the diffusion equation,

$$\frac{\partial n}{\partial t} = D\frac{\partial^2 n}{\partial x^2}, \tag{5.83}$$

known as Fick's Second Law. The density of ions initially can be determined from the product of cross section ratios as in chapter 3 but the time evolution of the density will be prescribed by the solution to this equation. Applying Fick's second law means having some understanding of the diffusion coefficient. A simple form for the diffusion coefficient for a particle moving through a background gas exists as,

$$D = \frac{\lambda_{mfp}^2}{\tau}. \tag{5.84}$$

The mean free path and mean free time can be calculated from the neutral density, mean speed and effective cross-section for the species involved,

$$\begin{aligned} D &= \frac{\lambda_{mfp}^2}{\tau} \\ D &= \lambda_{mfp} v_{th} \\ D &= \frac{v_{th}}{n\sigma}, \end{aligned} \tag{5.85}$$

but it is known that the neutral density of this system is not a constant which means the diffusion coefficient isn't either. To understand the impact of this variation, first look at Fick's first law which states that the diffusive flux is proportional to the density gradient,

$$\Gamma = -D(r)\frac{\partial n}{\partial r} \tag{5.86}$$

for a diffusion constant, D, that is a function of position, r. Using this equation to conserve mass arrives at the general form for Fick's Second law,

$$\dot{n} = -\frac{\partial}{\partial r}\left(D(r)\frac{\partial n}{\partial r}\right). \tag{5.87}$$

Applying the product rule here produces two competing terms: one in which the diffusion coefficient is constant and one in which it is differentiated.

$$\dot{n} = -\left(D\frac{\partial^2 n}{\partial r^2} + \frac{\partial D}{\partial r}\frac{\partial n}{\partial r}\right) \tag{5.88}$$

Typically, where D is a constant, finite difference methods can be applied to solve for the density at every point on the grid r at the next time increment. The same method can be exercised here either before or after the second derivative in Fick's Second Law is applied. Consider the following: the density at a time indexed by i and spacial point indexed by j is given by n_j^i. Similarly, the diffusion coefficient can be indexed in the same way. Defining the derivative can be done in an explicit forward differencing in time and central differencing in space method.

$$\frac{\partial n}{\partial t} = \frac{n_j^{i+1} - n_j^i}{\Delta t}, \tag{5.89}$$

$$\frac{\partial n}{\partial r} = \frac{n_{j+1}^i - n_{j-1}^i}{2h}, \tag{5.90}$$

$$\frac{\partial^2 n}{\partial r^2} = \frac{n_{j+1}^i + n_{j-1}^i - 2n_j^i}{4h^2}. \tag{5.91}$$

Incorporating these definitions into Fick's Second Law gets an explicit expression for the density at all j's at the $i+1$ time.

$$n_j^{i+1} = n_j^i + \frac{\Delta t D_j^i}{4h^2}\left(n_{j+1}^i + n_{j-1}^i - 2n_j^i\right) + \frac{\Delta t}{4h^2}\left(D_{j+1}^i - D_{j-1}^i\right)\left(n_{j+1}^i - n_{j-1}^i\right) \tag{5.92}$$

For the purposes of this thesis, this solution is acceptable for the diffusion of protons in the cloud and can be iterated over diffusion timescales, Δt_D, defined as some fraction of

the electron timescale that calculates ablation due to electrons,

$$\Delta t_D = \frac{\Delta t}{R}, \tag{5.93}$$

where R is some number defining the ratio of the two timescales such that $\Delta t_D < \Delta t$.

Ablation

The ions will gain energy by converting potential energy from the sheath into kinetic energy and imparting that energy to the molecules in the pellet. The ablation calculation itself is identical to the case for electrons with the exception that the ions will all gain the same amount of energy over the last mean free path before contact with the pellet. Until then, any energy gained by the ions will be lost over the previous mean free paths to inelastic collisions with neutrals meaning that the potential across the final mean free path is the only energy delivered to the ions that counts towards ablation. Therefore,

$$E_{ion} = \phi\Big(r_p + \lambda\Big) - \phi\Big(r_p\Big). \tag{5.94}$$

This accounts for the energy gained and delivered to the pellet but not the amount of particles affected by the sheath. The sheath will capture any ions within it and draw them towards the pellet eventually, but within the time Δt only a portion of them can accellerate across the many mean free paths between their initial position and the pellet in that time. The ion density will be evaluated via the finite difference method outlined above on the grid points separated by an amount h. The time taken to cross a mean free path at a point r assuming a constant acceleration across λ is given by,

$$t = \frac{v - u}{a}. \tag{5.95}$$

The acceleration is determined by evaluating Newton's second law,

$$a = \frac{e\Big(\phi(r_p + \lambda) - \phi(r_p)\Big)}{\lambda m_e}. \tag{5.96}$$

The time taken to cross that grid point can then be evaluated simply as,

$$t_h = \frac{h}{\lambda}, \tag{5.97}$$

assuming that a, λ and $\Delta\phi$ remain approximately constant over the distance h. The same calculation can be repeated until the total time to cross a distance is greater than the diffusive timescale,

$$\Delta t_D < \sum t_h. \tag{5.98}$$

This would correspond to a special point in the sheath r_s enclosed within which all ions will be captured by the sheath in a diffusive timestep and will ablate molecules. The ion densities within these enclosed grid points are summed and applied to an adapted form of the ablation calculation with a constant E.

5.4 Conclusion

This chapter has applied a logical structure to the ablation problem using the CSDA and simple thermodynamic arguments in unison with the evaporative model presented in the previous chapter. The set of equations that must be solved are summarised below:

$$\frac{\mathrm{d}\tilde{E}}{\mathrm{d}\tilde{x}} = K\frac{\tilde{\rho}}{\tilde{E}}\frac{Z}{A}B\big(\tilde{E}\big) \tag{5.99}$$

$$\frac{\mathrm{d}\tilde{\phi}}{\mathrm{d}\tilde{x}} = \psi\tilde{n} \tag{5.100}$$

$$\tilde{\Gamma}_E = \sum \eta_i \tilde{E} \tag{5.101}$$

$$\tilde{E}_p = \tilde{\Gamma}_E \tilde{r}_p^2 \Delta\tilde{t} \tag{5.102}$$

$$\tilde{N}_{loss} = \frac{\hat{N}}{N_0}\tilde{E}_p \tag{5.103}$$

$$\tilde{r}_p = N^{\frac{1}{3}} \tag{5.104}$$

It has also establised patterns and expectations of the influence of the seeded potential on successive iterations of electrons entering the cloud which has been compared to the case of CSDA acting alone. The results of these simulated environments could be useful to interpretting the results of the iterative simulations to be run in the following chapter, particularly where varying shapes to the potential field is considered. Additionally a model for the diffusion of ions has been developed using the drift-diffusion model as a means to evaluate the diffusion coefficient for ions. This step is essential to the greater goal of the thesis in examining what role ions may play in the ablation problem and not considering electrons as the species exclusively performing ablation.

The content of this chapter is essential to understanding the evolution of the system through the simulation described earlier and the consequences for the lifetime of the pellet within the plasma environment. This is the ultimate goal of this thesis which this chapter has made significant strides in approaching and which the following chapter arrives at.

Chapter 6

Temporal Evolution of the Pellet-Cloud System

Following from the results of the last chapter which act to identify charge stopping for a single instance in time, this chapter will expand on this idea by incorporating time evolution to the problem with a variety of scenarios investigated. This is a more realistic treatment of the system but presents additional challenges not tackled in chapter 5 such as the inclusion of transport between various times and the self-consistent cloud. Managing these problems will enable for a discussion on how, based on the model from chapters 4 and 5, the presence of electrons previously stopped in the cloud will affect the next stream of electrons to enter the cloud. The new physics established in this chapter will be the impact of a temporal evolution of the cloud with a self-consistent ablation. Some key parameters to be calculated following the research in this section are the ablation rate and the pelllet's lifetime and the dependence on time can be compared to results from Parks and Turnbull (1977). The chapter will set out the initial conditions and define the various phenomena that will be included to build up a more realistic vision of the physics at work in this system. Quantities such as electron density, electron potential, ablation rate and projected lifetime will be presented and compared (where possible) to existing data and established theoretical frameworks.

6.1 Simulation Conditions

6.1.1 Boundary Conditions

For any boundary value problem the conditions are of the utmost importance in defining the behaviour within the domain and this problem is no exception. For a 1D problem there are only two conditions that need to be defined and satisfied: ϕ_0 and ϕ_N. More specifically, these respectively correspond to ϕ_{r_p} and ϕ_{r_c}. The condition at $x = r_c$ is rather straight-forward to define. The large volume of plasma in the vessel compared to the relatively small volume of the cloud allows a definition of the ϕ_{r_c} condition to be 0V. The large body of plasma outwith the cloud structure will react to accommodate a small body of charge within it so as to neutralise its effect and effectively set it to 0V. The condition at the pellet surface requires a more mathematical reasoning, as has been discussed in section 1.3. The formation of a floating sheath is expected to occur on a timescale of the order a few nanoseconds with a steady-state floating potential determined according to equation 1.45. This is evaluated for a deuterium plasma to be ~ -3184V using equation 1.45. Of course, this value is predicated on a continuing flux of ions at the wall which equates the electron flux. This is in fact contrary to the assumptions made in chapter 3 but will be justified by observing that the high collisionality of the cloud for electrons at the pellet surface will mean that electrons can not escape the vicinity of the pellet surface and will remain close enough to its surface so as to maintain that potential.

6.1.2 Initial Conditions

The starting state of the system for continuous evolution will have an already established cloud and a floating sheath. The connection between these two is that the depth of the cloud will be equal to the sheath length. This lengthscale has been chosen so that the different models may be compared to each other and this can only be done confidently if all other parameters are equal. Because two of the models incorporate a floating sheath that has been previosuly established a natural time to start is at such a time when the width of the cloud is equal to that of the sheath itself. The sheath should develop and achieve the dynamic equilibrium in a few nanoseconds and the cloud should establish on a timescale longer than that. Starting the simulation at a time at which the size of the sheath, s, is equal to $r_c - r_p$ will permit a simple continuing evolution of the system with the electrostatic potential evolving in a simple and self-consistent way.

Defining the value of s now requires a solution to equation 1.41. The Runge-Kutta algorithm used before will be sufficient to appropriately solve the equation however the size of the sheath is an unknown but the boundary values in the potential are known including a pre-sheath. With the sheath potential offset by the pre-sheath amount the equation is solved numerically and the solution is approached step-wise for as long as the potential is lower than the pre-sheath value. The sheath size is then the value of x where the potential is 0V. For a plasma temperature of 1keV the sheathsize is 6.055×10^{-4}m which means the pellet has been in the plasma for approximately 8.54μs. The pellet has currently been injected for less than $10^{-2}\tau_p$ which means that a negligible amount of time has passed since injection. It is implicitly assumed here that the trend for the ablation rate follows the evaporative model strictly and that at the starting time the system will exist in the pre-defined configuration. This time will act as the initial starting time for a nano-second evolution of the system with the following conditions tested and compared.

6.2 The Simulation Scenarios

It is important to note a variety of conditions that can be turned on or off for these simulations to assess the effect they may have on the evolution of the system. Obvious effects such as the need to consider the potential due to stopped charge and the effect of the sheath can be readily turned on or off but nuanced phenomena such as the release of electrons from an ever-shrinking pellet (to preserve the floating potential on a smaller surface) are more subtle and may have a weaker impact. These differences are included below.

- Entirely Neutral Cloud - The electrons traverse the cloud and are stopped with a solution to Poisson's equation calculated but not applied to the next iteration. Additionally, the consideration of a sheath field is not needed and the diffusion of ions is ignored. This is the simplest possible scenario.
- Charged Cloud - Electrons traverse the cloud and are stopped with a self-consistent solution to Poisson's equation calculated. Boundary conditions on the pellet and cloud edge are both 0V, effectively ignoring the sheath potential and excluding the diffusion of ions.
- Charged Cloud with a floating sheath - Electrons traverse the cloud and are stopped with a self-consistent solution to Poisson's equation calculated. In this instance the

Quantity	Value
Δt	50ns
Δt_i	5ns
t_f	1ms
$\bar{E}$	1keV
E_{low}	100eV
E_{upper}	20keV
ΔE	500eV

Table 6.1: The simulation parameters used throughout this chapter.

boundary conditions are the same as before but with a solution to Poisson's equation for a Debye sheath incorporated too. The two potentials are added to create the total potential encountered by the incoming electrons.

- All effects considered - Electrons traverse the cloud and are stopped with a self-consistent solution to Poisson's equation and boundary conditions as described in the previous point. Ions are created in situ through ionisation processes and diffuse through the cloud until they diffuse into the sheath at which point they contribute to the ablation process by the energy gained in a single mean free path. This is the most inclusive scenario.

The simulation parameters are outlined in table 6.1. The main results from these experiments are the potential in the cloud, the electron density and the instantaneous ablation rate.

6.3 Results

As explained earlier, the most essential quantities that determine how the ablation rate will develop are the electron density and its associated potential. This determines the ablation rate and how it evolves in time which will be essential for comparing to other published studies and is discussed in section 6.3.5.

6.3.1 Neutral Cloud

Electron Density

The density profiles given in figure 6.1 show the cumulative effect of the CSDA in the neutral model. Most notably, the shape of the profile is a constant, preserving the shape of the EEDF in space following the transform due to the CSDA. With more iterations, the total entrapped density increases, the size of the peak increases with time and, because of the greatest ablation relative to the other models tested, the cloud radius, r_c, increases the most. The apparently discrete peak on the left hand side of the plot in fact shows the density of deposited charge on the pellet and the finite width corresponds to the depth of the pellet that is lost. So, while this appears to be a numerical artifact it is just a consequence of the greater fraction of particles striking the pellet over a sustained period and the finite radius of the pellet that has receeded.
The absence of any influence of a potential in the development of the system means that the fraction of particles hitting the pellet is determined exclusively by the CSDA. The profile, as stated earlier, is just an upscaling of the initial neutral profile excepting small changes due to the expanding cloud and the restructuring of the neutral density profile to accommodate new spatial limits. The restructuring of the neutral density at $r \approx r_c$ accounts for the more gradual rise to the peak of the profile. The largest changes are observed to occur at these points as this is where the lower energy particles in the distribution are expected to stop which occupy the largest portion of the EEDF for the spatial bin size. This model is expected to produce the greatest ablation and thus the largest cloud. The following models (save for the diffusive case) will, for all $\tilde{t}$, produce greater shielding of particles and thus weaker ablation. The system should evolve more slowly for these cases.

Electric Potential

The electric potential will always reflect the charge distribution which evolves in a simple way in this model. From figure 6.1 it is clear that the charge distribution grows in all places over time and the potential similarly grows in all places as presented in figure 6.2. In this model the potential does not influence the evolution of the system, these potentials are calculated to compare to the other models. In particular regard to the Fully Neutral model the potentials are much larger than will be found in the later models most likely because the domain itself is larger here. This allows for the potential to grow more in the middle

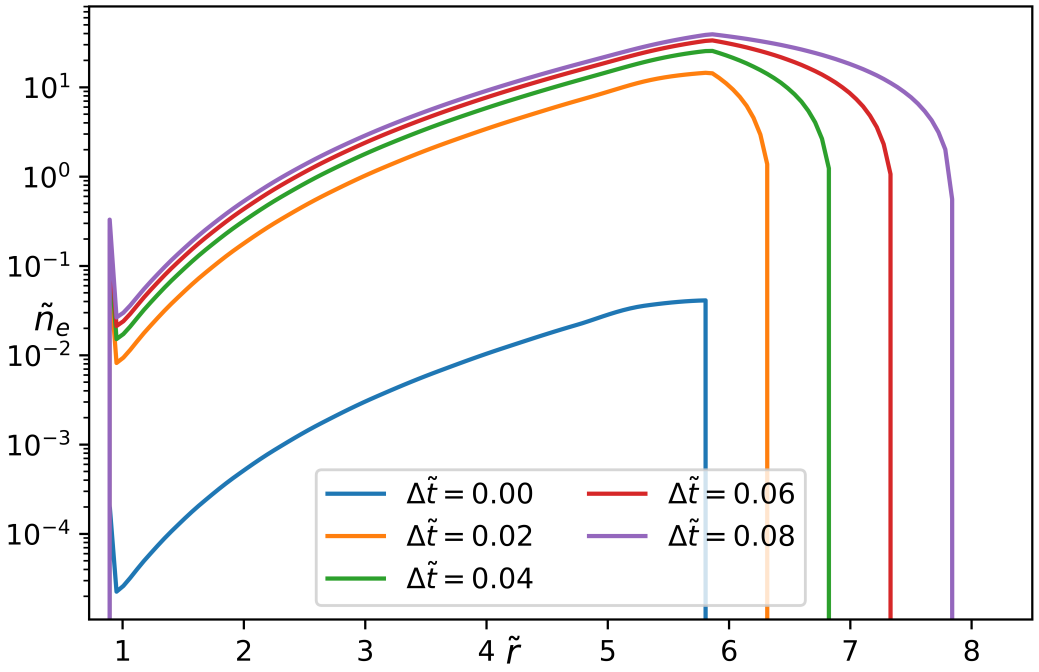

Figure 6.1: The accumulated density of electrons after successive iterations of the Fully Neutral model corresponding to a non-dimensional total advanced time given in the legend. The kink from the first iteration at $r \approx 6$ persists despite the ongoing transport because the amount of material transported is so small that the addition of more material from the next iteration is significantly greater than the material lost during transport.

of the domain before the boundary condition at the edges must be satisfied which acts to return the potential to 0V. However, it is not so concerning that the potentials in the cloud are so large as to be unsustainable because the model excludes several phenomena that are essential for modelling this system, most notably the impact of potential on the stopping of charge.

6.3.2 Charged Cloud

Electron Density

The profile of accumulated charge is given in figure 6.3 for a selection of times, common to figure 6.1. The most obvious difference is the departure from the general shape of the

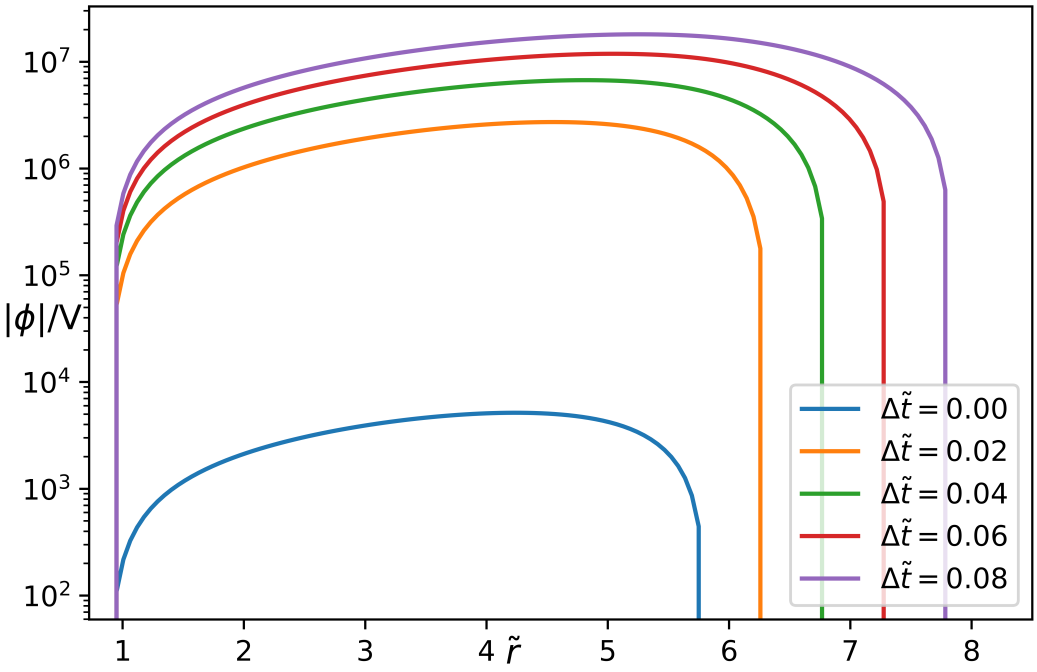

Figure 6.2: The potential due to the accumulated density of electrons after successive iterations of the Fully Neutral model corresponding to a total advances time given in the legend. The potential field is negative but the absolute value of that potential is taken here so as to use a logarithmic scale for the vertical axis. The sharp drop at the right hand side of each line corresponds to $\tilde{r}_c$ for the cloud in its existing configuration.

profile after the initial input of electrons corresponding to $\Delta\tilde{t} = 0.00$. The profile now shows a minimal increase in the size of r_c, a significant increase in the density co-spatial with the initial peak, with minimal increase in the central region and some increase closer to r_p. The marginal increase in r_p is to be put down to the additional shielding from the previously stopped electrons which are mostly sitting at the initial peak which sees a positive feedback system developing: as more electrons stop there, the potential increases, which causes more electrons to stop there and so on and so forth. However, only the lower energy electrons in the EEDF will stop there as more energetic particles will slow, but fully traverse the point where the potential is lowest and will then see a boost to their kinetic energy as they leave the potential well. This is what causes the increases, albeit gradual, of electron density closer to r_p. This is because only the most energetic electrons can traverse the cloud owing to the retarding potential and the neutral stopping from CSDA and these

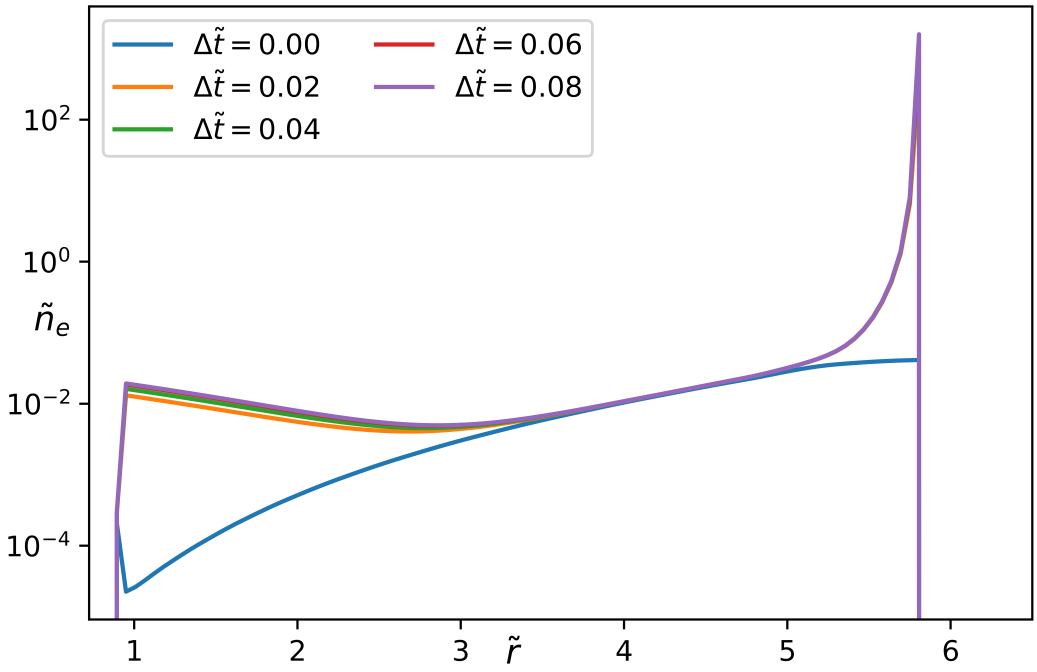

Figure 6.3: The accumulated density of electrons after successive iterations of the Charged Cloud model corresponding to a non-dimensional total advance in time given in the legend. The $\Delta\tilde{t} = 0.0$ line is identical to the same line in figure 6.1 because there is no prior charge to slow the first iteration of particles.

electrons reside in the tail of the EEDF and therefore make diminishing contributions to the density in this region.

This diminishing increase in density local to $r = r_p$ implies that the ablation rate should reduce. As was illustrated in the previous chapter, this is because the particles lose the maximum possible amount of energy at the lowest point of the potential and then slowly recover it but all the while the CSDA has a more profound influence as it more adversely affects lower energy particles. So not only will the fraction of impacting particles reduce, but the energy with which they strike the pellet is also lowered.

Electric Potential

The charge density in this model is notably different from the previous one and so it is to be expected that differences should be apparent. In particular, the potential is much weaker at its peak than in the neutral model and also much closer to the r_c. This highlights the feedback of the potential on to the ablation. The potential acts on the incoming particles, reducing their energy and causing them to stop at a point closer to r_c than if the potential was ignored. This achieves two things: it lowers the energy of particles impacting the pellet and it also causes more particles to accumulate near r_c which should cause the potential to spike there but because the boundary condition forces the potential to smoothly reach 0V at $r = r_c$ it is not as severe as initially thought. To compound this effect, the weaker ablation moves r_c forward by only a small amount meaning that the distance between the peak of charge density and r_c is approximately constant and small such that the boundary condition can greatly hinder the growth of the potential at this point. This explains why the potential never reaches the strengths seen in the neutral model previously and also why the cloud does not expand at the same rate. Consequently, even at this stage, it can be said that the self-consistent potential allows for a significantly different evolution of the system to manifest as compared to when it is ignored.

6.3.3 Charged Cloud with a Sheath

Electron Density

The profiles in figure 6.5 build upon the structures presented in figure 6.3 by incorporating a sheath field. The notable changes between this figure and figure 6.3 are the more muted growth of r_c, the initially weaker density near r_p and its slower growth over the course of the simulation. The initially lower density in the region of the pellet can be attributed to the sheath which immediately adds an additional $\sim$3kV potential for particles to overcome and increases the minimum traversal energy by 3keV stopping a greater fraction of the EEDF. This explains why the density builds at a greater rate than compared with the Charged Cloud simulation described previously. Consequently, the number flux and energy flux delivered to the pellet at all times is reduced lowering the ablation rate and the subsequent growth of the r_c.

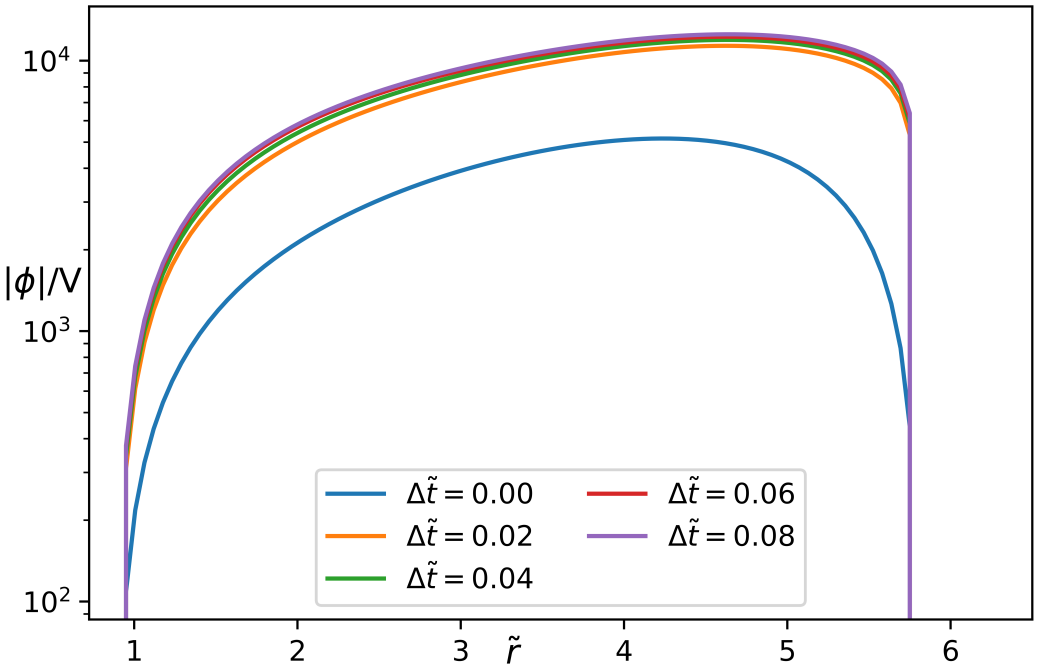

Figure 6.4: The potential due to the accumulated density of electrons at the same times as presented in figure 6.3 in the Charged Cloud model. The potential field is negative but the absolute value of that potential is taken here so as to use a logarithmic scale for the vertical axis. As with the neutral density, the $\Delta\tilde{t} = 0.0$ line is also identical to the same line in figure 6.2 because the density profiles are identical in the first iteration.

Electric Potential

The electric potential develops in much the same way as the Charged Cloud case with the added complication of the floating sheath at the pellet. The combination of the sheath with the potential from the free charge is presented in figure 6.6 and it is clear that near r_p the sheath dominates the potential profile. This shows itself in the potential profile at a discontinuity at around $\tilde{r} = 1.4$ where the sheath begins and also in the density profile in the same region where the charge accummulates much more slowly there. Whilst it is hard to see on these graphs, it is expected that charge will collect at a quicker rate somewhere between the peak and this region where the sheath begins. This is due to the peak of charge behind the particles near r_c, which, once passed, will donate energy to the particles but a portion of electrons will not have the energy to traverse this peak and the sheath and

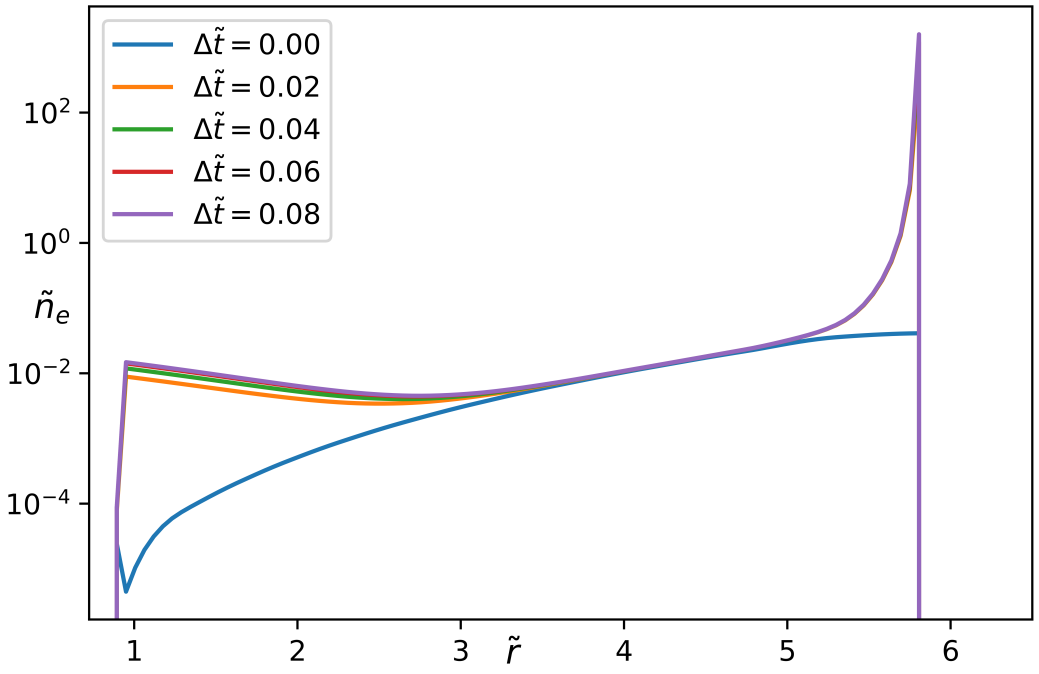

Figure 6.5: The accumulated density of electrons after successive iterations of the Sheath model corresponding to a non-dimensional total advance in time given in the legend.

thus will stop somewhere in between. The magnitude of the potential here will increase and act to further this effect over time. Consequently, as with the Charged Cloud model, the energy impacting on the pellet reduces and the ablation rate decreases. This can be seen, albeit with some difficulty, in the separation of the vertical lines in figures 6.5 and 6.6 near $\tilde{r} \approx 6$.

6.3.4 Charged Cloud with a Sheath and Ion Diffusion

Electron Density

Figure 6.7 bears almost no differences to figure 6.5. This highlights the almost negligible influence that the presence of ions have over the ensuing dynamics as the profiles remain almost identical at all points. This can be inferred by observing that as the ion density increases by an amount $\sigma_i n_0$ so too does the electron density therefore preserving the

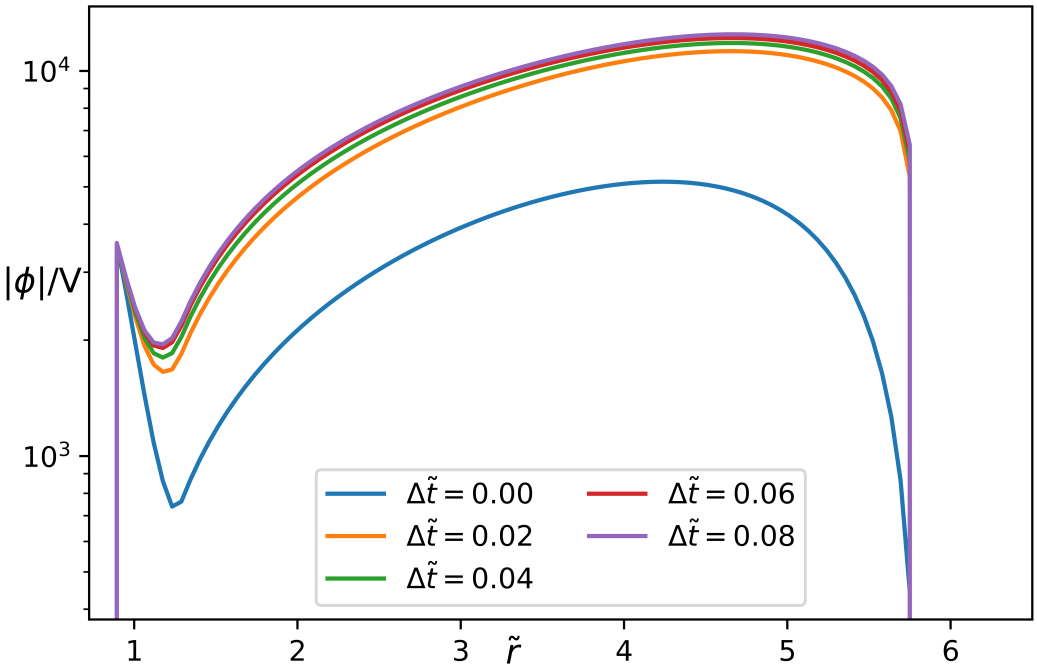

Figure 6.6: The potential due to the accumulated density of electrons at the same times as presented in figure 6.5 in the Sheath model. The potential field is negative but the absolute value of that potential is taken here so as to use a logarithmic scale for the vertical axis.

overall charge density. The potential profile should therefore remain unchanged and the ablation rate due to electrons identical to that for the sheath case.

Ion Density

The ion density reflects the electron density save for two notable features. The obvious feature is the absence of any ions near the pellet but this is due to the immediate loss of particles inside a space that can be crossed by collisional ions in an ion timestep Δt_i. This space is vacated of positive charge as it is drawn abruptly towards the pellet and causes supplementary ablation. The second is due to the interplay of ion generation due to increased electron stopping near the pellet due to the sheath and the diffusion of material from that point. This creates a minimum of ion density in the middle of the cloud and it peaks towards the boundaries where maximal charge deposition occurs. One key feature

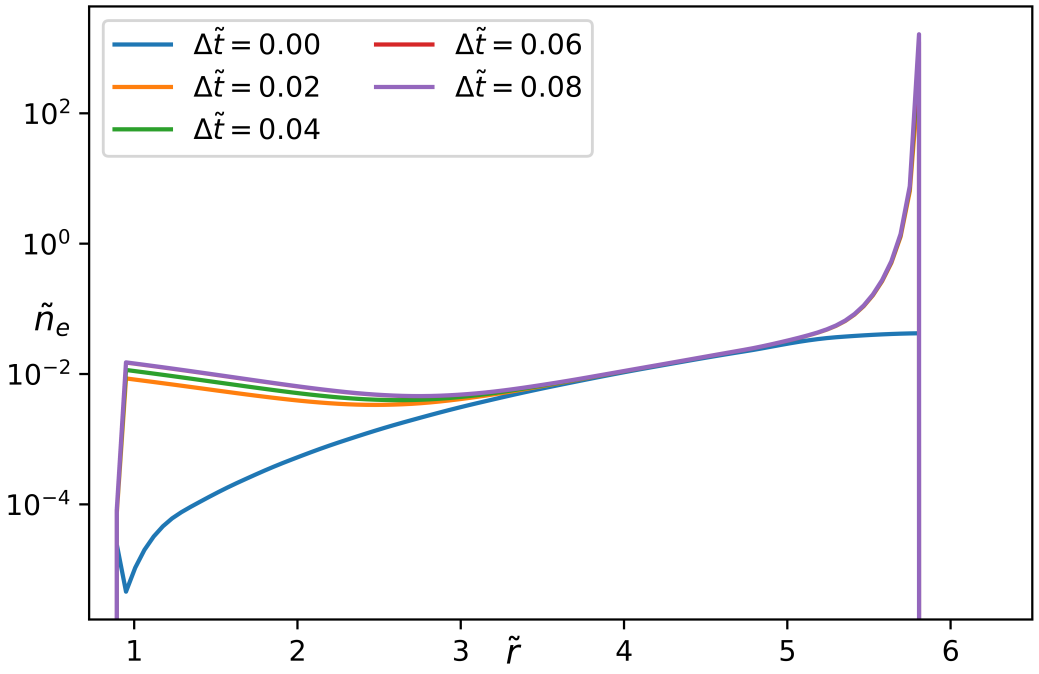

Figure 6.7: The accumulated density of electrons after successive iterations of the Diffusive Ion model corresponding to a non-dimensional total advance in time given in the legend.

that should be distinguishable between figures 6.5 and 6.7 is that with the ionisation of the neutrals the electron density should increase at all points by $\frac{\sigma_i}{\sigma_T}$. This ratio is better understood when considering cross-sections as likelihoods of interactions occuring. With that in mind, this ratio is the likelihood of an ionisation process (given by σ_i) occuring given that an interaction of any sort (given by σ_T) occurs. For the times illustrated in the figures in this chapter the ratio of the electron densities in the Sheath model and Diffusive Ion model, notated by n_e^{S} and n_e^{I}, is given by,

$$R = \frac{n_e^{\mathrm{S}}}{n_e^{\mathrm{I}}}. \tag{6.1}$$

This ratio is plotted across the domain in figure 6.9a and the value at $\tilde{r} \approx 1$ is plotted in figure 6.9b for the duration of the simulation. From figure 6.9a it is clear that except for the $\Delta\tilde{t} = 0.0$ line, the quantity R is not equal to $1 + \frac{\sigma_i}{\sigma_T}$ for $\frac{\sigma_i}{\sigma_T} \approx 0.02$. The complicated evolution of the system over many iterations makes it difficult to understand exactly what

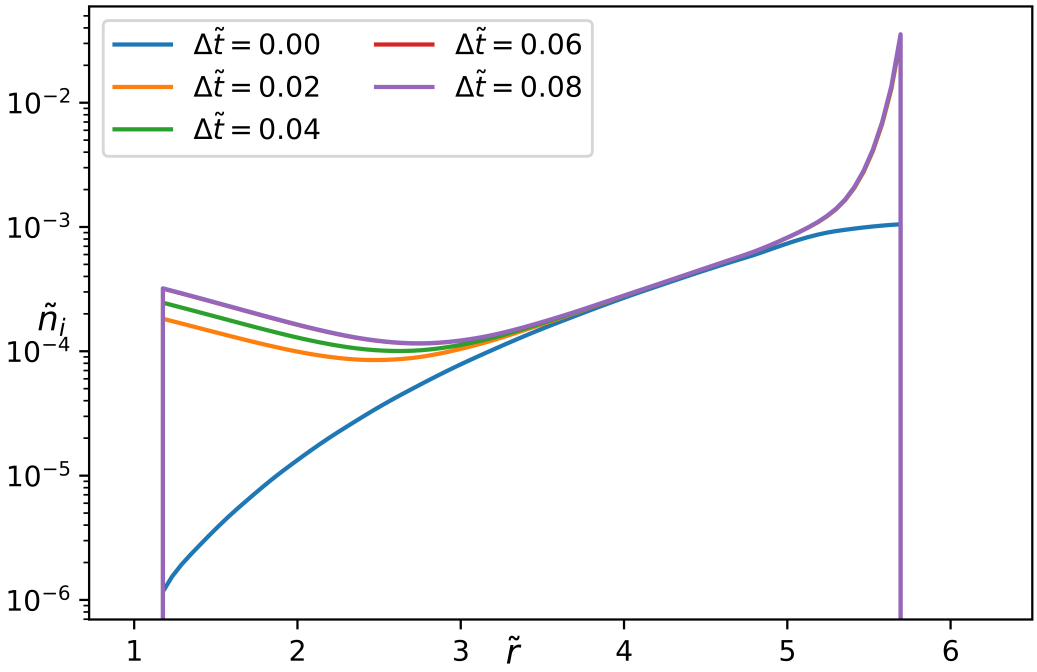

Figure 6.8: The accumulated density of ions after successive iterations of the Diffusive Ion model corresponding to a non-dimensional total advance in time given in the legend. These ions have been generated in situ by the stopped electrons in proportion with the ionisation cross-section relative to the total cross-section, $\frac{\sigma_i}{\sigma_T}$.

the cause of these deviations from $R = 1.02$ is. The key takeaway from this figure is that the electron density does differ between the Sheath and Diffusive Ion models but it is imperceptible on the logarithmic scales in figures 6.5 and 6.7.

It might be suspicious that an apparent trend in the evolution of R develops and that the $\Delta\tilde{t} = 0.06$ line breaks this pattern but this is explained by looking at figure 6.9b. At the point $\tilde{r} \approx 1$ the value of R has been calculated and plotted against the non-dimensional time. Clearly it is oscillatory with no clear period but in figure 6.13 it is discernible that it is coincident with abrupt changes to the ablation rate for the diffusive ion model. It is therefore a consequence of the choice of $\Delta\tilde{t}$ that some lines sit above and below each other. If the lines were sampled differently the pattern may not obviously emerge.

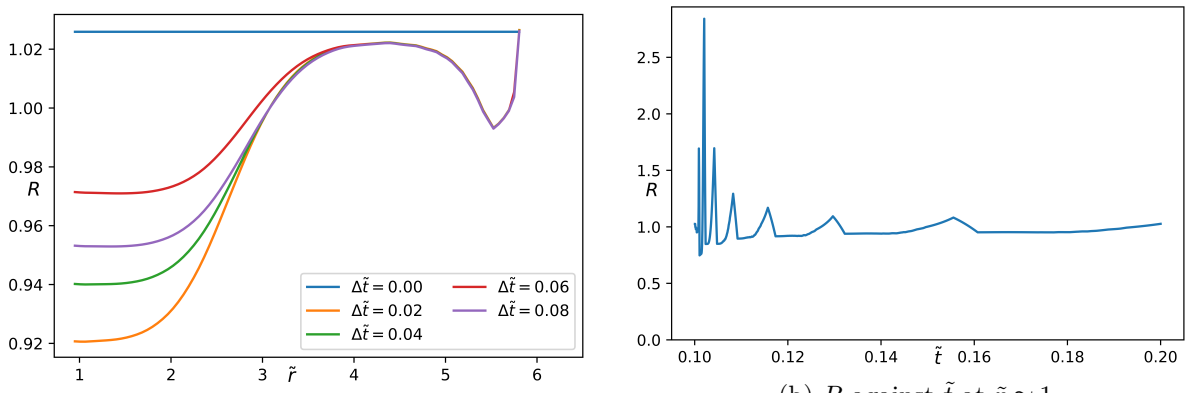

(a) R against $\tilde{r}$

(b) R against $\tilde{t}$ at $\tilde{r} \approx 1$

Figure 6.9: Panel a) presents the change in R for each point on the grid at various times defined in the legend. Panel b) presents the change in R at $\tilde{r} \approx 1$ over the duration of the simulation.

Electric Potential

The potential reflects the sum of these two densities when the relevant charge is assigned but retains many of the features of the Sheath model potential. The charge separation achieved by ionisation ultimately yields very little change to the potential profile, if any.

6.3.5 Ablation Rate

The ablation rate is the crucial quantity to be understood in any pellet study and is measured in Parks and Turnbull (1977) through $\dot{r}_p$. In this thesis comparisons will be drawn between the trend in $\dot{r}_p$ from NGS and the models used here. The real value of the recession speed is not under examination here but the observed trend is. Before investigating the results of these simulations it is important to understand that the energy imparted to the pellet is dependent on the number of particles striking the pellet and the energy of those particles. The value of $\dot{r}_p$ as a function of $\tilde{t}$ is given in figure 6.11 for all the models considered and both the NGS model from Parks and Turnbull (1977) and the freely developing evaporative model as outlined in chapter 4 of this thesis.

The purely neutral run neglects the effects of the potential and therefore the neutral CSDA is the only process slowing the electrons and because the cloud structures (r_c and $\rho(r,t)$) do not change much, neither does the stopping point or minimum traversal energy for the

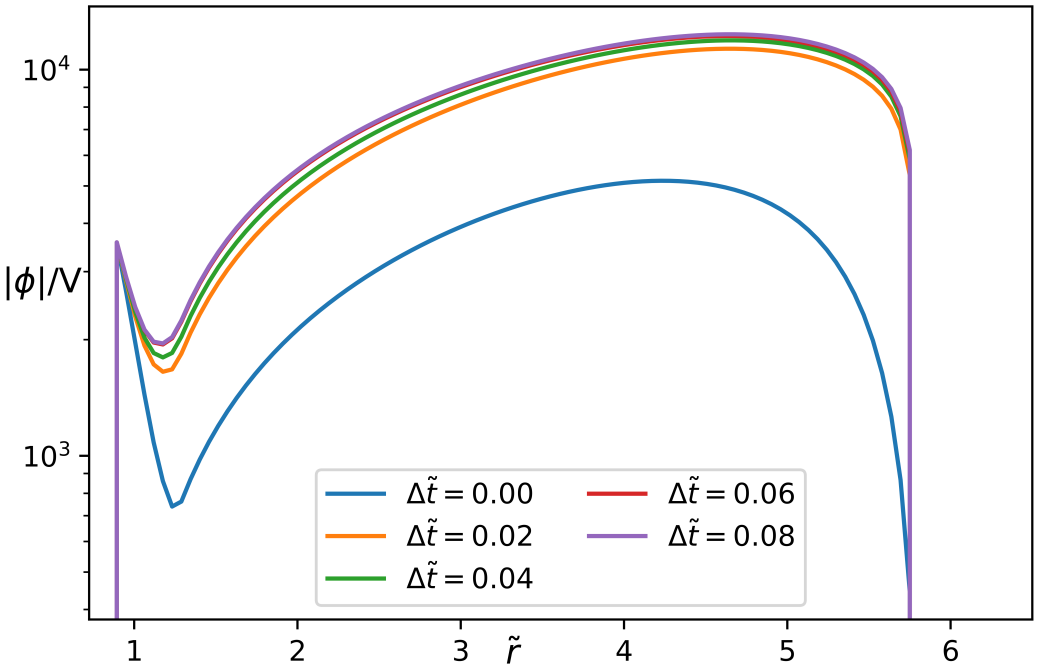

Figure 6.10: The potential due to the accumulated density of electrons and ions at the same times as presented in figure 6.5 in the Diffusive Ion model. The potential field is negative but the absolute value of that potential is taken here so as to use a logarithmic scale for the vertical axis.

electrons. Consequently the ablation rate is approximately constant over the period of the simulation. The explanation has so far ignored the sharp oscillations and discrete jumps occuring later in the simulation. The oscillations are due to the least energetic single bin striking the pellet in one cycle and then stopping in the next run. In turn this can be attributed to the choice of error criterion in the adaptive step solution to the stopping power equation. As the cloud expands, the stopping power decreases at r_c and consequently the particle can take a larger step and still satisfy the error criterion but as the ablation continues the cloud also gets larger meaning the particle has greater distance to travel. Eventually the cloud expands to such an extent that the particle will always stop. This numerical artefact could be removed by selecting a different set of error criteria for the RKF method but it does not exclude the possibility that a similar artefact would arise in the other models. This is dramatically different to the profile calculated from the NGS model

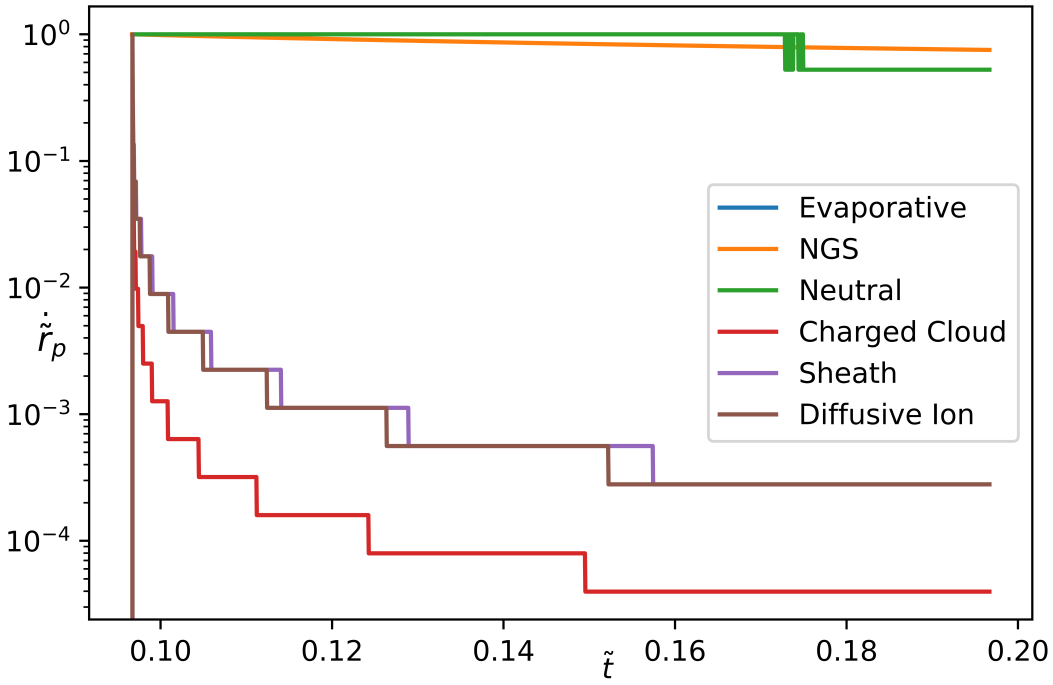

Figure 6.11: The recession speed of the pellet surface, $\dot{r}_p$ compared for the models in this simulation along with the NGS recession speed and the evaporative model. The evaporative model shown here is taken from 4.10 and is not informed by the ablation of particles in these simulations. Each line is normalised to its maximal value. The Evaporative model and NGS model lines overlap on this scale.

but it is also the simplest model investigated here with the crucially important absence of electrostatic effects, the inclusion of which produces a profile that varies significantly more in time. The Charged Cloud model considers the effect of CSDA and the electric potential and sees a noticeably declining ablation rate. This decrease in $\dot{r}_p$ is entirely due to the electric potential because it is shown to reduce the impacting energy flux of particles which will lower the ablation rate and therefore the effect of CSDA should be approximately constant, moreso than in the neutral case described above. More generally speaking the stopping power of the cloud due to charge is dramatically increased and sees a growth in time due to the increased quantity of charge in the cloud. It should therefore be a natural conclusion that the ablation rate should decrease in time when the potential is accounted for.

A similar trend is observed in the Sheath model but with the additional effect of the

floating potenial on the pellet that further slows the rate of ablation. The asymptotic trend returns which is attributed to the electrostatic potential but the vertical translation and scaling of the line is due to the sheath potential which adds an additional barrier for the electrons to overcome to reach the pellet. Even if the particles reach the pellet, their energy is further minimised by ϕ_s which may mean that the electron fraction that hits the pellet is preserved or approximately similar but the energy with which it impacts is lowered. It is, in a way, a more exaggerated form of the Charged Cloud model with the ablation rate decreasing more rapidly.

The influence of the creation and diffusion of ions is markedly similar to the sheath case in terms of its relative change over the simulation. The immediate conclusion to draw is that the effect of ions on the ablation rate is ultimately negligible. The ion density is always lower than the electron density because the likelihood of an ionising reaction occuring is strictly less than 1. It might be expected that the diffusion of ions towards the pellet would account for this contrast in charge density but the large neutral density inhibits ion motion and prevents any significant number of particles entering the capture region of the pellet. In addition to this, the energy gained by an ion across a mean free path at $r \approx r_p$ is so small ($\sim$ 1eV) that the combination of low number flux and minuscule energy maintains a very low energy flux. In saying that, the fall in $\dot{r}_p$ for the Diffusive Ion model always occurs before the equivalent change in for the Sheath model. This indicates that the ions do make a differenc ecompared to the Sheath model but not enough to eliminate the effect of the sheath on stopping additional electrons. Consequently it could be argued that the supplementary ablation from the ions is so low as to be safely ignored.

It is also worth commenting now that if the ablation rate is low enough then almost no new material is being injected into the cloud. This implies that the configuration of the system should not change much which is what has been done in these simulations. Realistically, of course, the cloud should continue to expand at the speed $\dot{r}_c$ and the interior points at their own evaluated $\dot{r}$. This method has been applied to the electrons, which are attached to neutrals, but the neutrals themselves in instances of low ablation should evolve in a similar way. This development in the cloud has been neglected so far but could be an important and relevant change to implement in further studies. One would expect this change in the density profile and size of the cloud to change the energy flux striking the pellet but this isn't the case. The linear dependance of $\frac{\mathrm{d}E}{\mathrm{d}x}$ on both the density and the cloud size (through the number of dr steps to be taken) the changes in r_c and $\rho(r,t)$ will negate each other. This can be seen more fundamentally by recalling that the solution to $\frac{\mathrm{d}E}{\mathrm{d}x}$ is to integrate over the path length which encompasses the mass encountered along the path

length which would be conserved for no change in r_p.

The main feature to consider when comparing the three models in which the charging of the cloud has been considered is the points at which the ablation rate drops. The ablation rate, which scales with $\dot{r}_p$ in this model is directly attached to the current pellet radius and so when the ablation rate drops the pellet has become smaller. Looking at figure 6.11, $\dot{r}_p$ for the Charged Cloud model drops first indicating that the ablation rate is greatest here which aligns with the expectation that the impacting energy is the greatest for all the charged cloud models. The Sheath model should ablate slower than the Charged Cloud model which is seen in figure 6.11 which is expected with the extra potential barrier the sheath creates at the pellet surface. However, incorporating the ions in the Diffusive Ion model causes $\dot{r}_p$ to decrease before the Sheath model but is still quick to decrease as in the Charged Cloud model. It can therefore be said that ions do make some contribution to the ablation process but not enough to negate the effect of the potential on the incoming electrons and restore an ablation rate consistent with a neutral model.

Figure 6.13 demonstrates the vast difference in the importance of the electron ablation compared to the ion ablation. Clearly, the ion ablation is many orders of magnitude lower than the electron ablation and both, on average, decrease with time. The ion ablation profile exhibits some unexpected behaviour which is challenging to unpack and confidently explain. It is possible that these periodic envelopes are caused by an increase in the local ion density due to many successive rounds of ionisation and the immediate drop in the ablation rate is coincident with the change in the pellet size. The discrete and seemingly random changes in the ablation rate within these envelopes is much harder to understand but it is likely that this is evidence of the ebb and flow of the diffusion of ions from outside $r > r_s$ to $r < r_s$, the generation of ions due to local electron deposition and the increasing influence of the potential on the stopping of the electrons as described above. When the non-dimensionalisation is removed from figure 6.11 a version of the graph can be produced that enables a simple comparison with observations and other simulations. Figure 6.12 presents the actual values of the ablation in terms of particles released per second, $\dot{N}$. It is possible to look at values for other studies. A wide range of parameters exist for these kinds of experiments and simulations but in most cases the ablation rate is of the order $10^{23} - 10^{25}\mathrm{s}^{-1}$ as in Senichenkov et al. (2006); Gál et al. (2008); Baylor et al. (1992). The models produced in this thesis all fall short of these desired rates. The neutral model comes close and does maintain an approximately constant ablation rate but the lack of any consideration of the effects of charge implies that charge would need to evacuate the cloud at the rate it is injected in order to meet this charge neutrality. The other models fall short

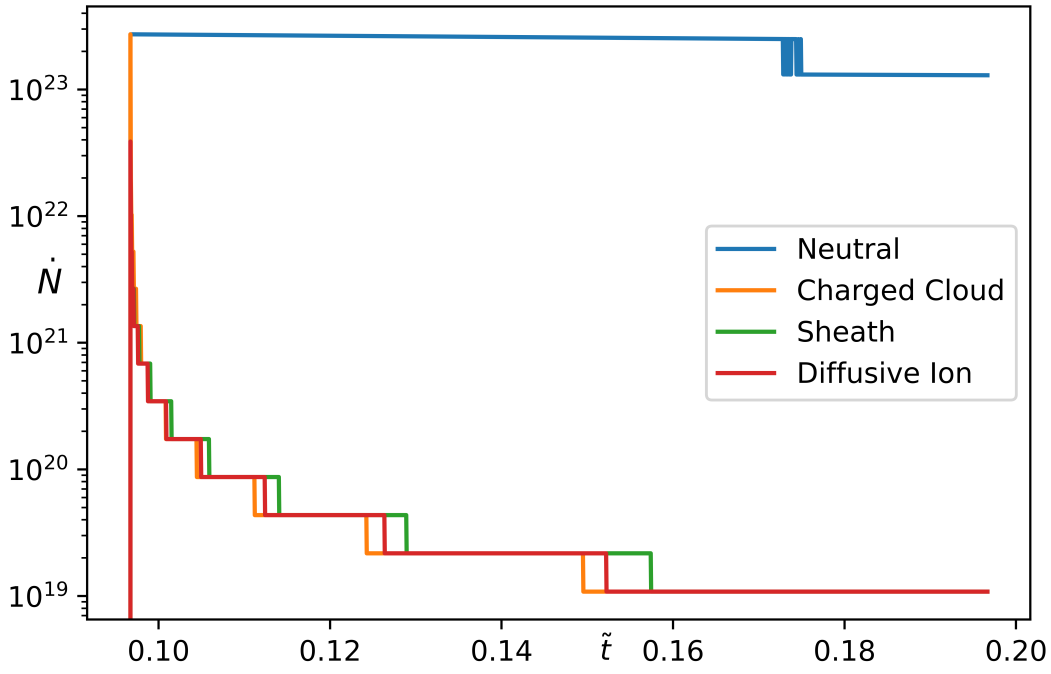

Figure 6.12: The ablation rates for the models tested in this thesis in real units.

by many orders of magnitude. This implies that the overwhelming potential within the cloud inhibits any significant ablation from occuring and greatly mitigates the evolution of the system.

It would be expected that if the ablation rate falls the expanding cloud would reduce the density in such a way that the total stopping of a single particle across the cloud would be smaller but this is not the case. As has been mentioned previously, the total amount of matter in the cloud is always increasing or remains the same and the solution to CSDA is achieved numerically by effectively integrating the product of the density profile and some stopping funciton which is only a function of particle energy across a length. In effect, the amount of matter along a length determines how readily a particle is stopped and because this is never decreasing the minimum traversal energy is always increasing. The distribution of charge within the cloud is informed by the distribution of neutral particles through the density function but the minimum energy needed to traverse the cloud will be the same. The ablation rate can therefore only decrease given the current models but if material were to be lost from the cloud such that the cloud mass decreased then the

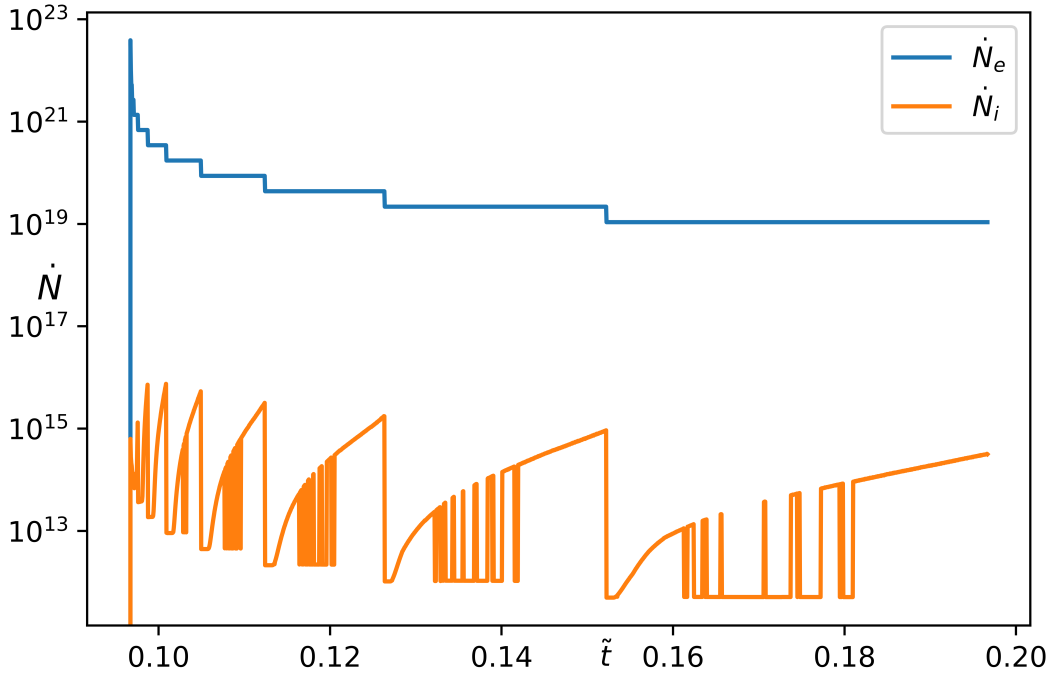

Figure 6.13: The ablation rate of electrons and ions for the "Diffusive ion" model over the simulation time compared.

ablation rate could increase again.

6.3.6 Projected Lifetimes

The projected lifetimes of the pellet in each model are given in table 6.2. These values were calculated assuming that the ablation rate at the end of the simulation was to continue for the rest of the pellet's life and based on the remaining molecules in the pellet it should be possible to arrive at an expected remaining lifetime. For a number of particles remaining in the pellet N_p and an ablation rate $\dot{N}$ this can be characterised as,

$$t_L = \frac{N_p}{\dot{N}}, \tag{6.2}$$

for a remaining lifetime t_L. It is expected that for a 1mm pellet in a 1keV plasma with a density of about $10^{19}\mathrm{m}^{-3}$ that the lifetime should be approximately 1ms. Clearly, from

Model	Projected Lifetime/ms
Neutral	2.1800×10
Charged Cloud	3.0342×10^5
Sheath	3.0433×10^5
Diffusive Ion	3.0433×10^5

Table 6.2: The projected remaining lifetime of the pellet at the end of the simulation for each model.

the table, the only model that produces an even remotely acceptable lifetime is the neutral model. The remaining models all propose a lifetime of the pellet that far outlasts any observed measurement. Of course, the neutral model completely neglects any presence of charged particles in the cloud to further slow charge and this result should be taken with some caution. The presence of charge in the cloud must be incorporated into any physical model of this system and the neutral model should act merely as a benchmark for assessing the impact of the potential relative to the neutral stopping. Clearly, it is not just substantial but the dominant stopping force in these simulations and in the form presented in this thesis, these models would preserve the pellet long after it is observed to have disappeared. It is therefore conclusive, that these models require additional phenomena beyond a sheath and ion diffusion to capture the essential physics at work in these systems.

6.3.7 Reproducing Hα Emission

The final objective of this thesis is to determine how accurately this model can repeat observations of various cloud emission profiles as observed in Cseh et al. (2017). In replicating the observed emission profiles, scaled to some arbitrary units, the cross section for dissociative excitation is needed at the truncation energy of the simulation for $e - H_2$ collisions. It is expected that the amount of emission should scale with the amount of excited atomic hydrogen in the cloud which, assuming it is only created by dissociative excitation, will scale with the interaction's cross-section at the truncation energy and the density of the reactants. Of course, it is possible that Lyman-β emission could occur as the excited electron falls to the $n = 1$ state. This would create a new loss mechanism for energy and therefore the intensity of Balmer-α emission would be weaker. However, it

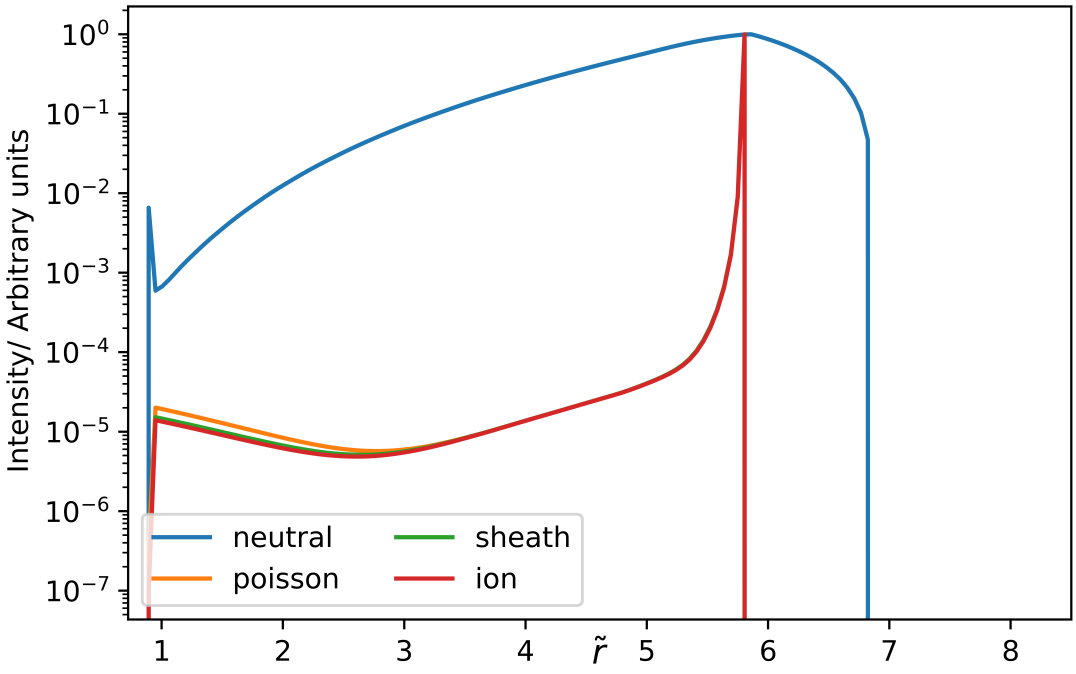

Figure 6.14: Hα emission at a cumulative $\Delta t = 0.04$ as calculated using equation 6.3. The intensity has been normalised relative to the peak of each line.

would be expected that the ratio of the density of states between $n = 2$ and $n = 1$ states after emission would be approximately constant across the cloud. This analysis is only interested in the shape of the emission profiles and the relative difference between models and therefore arbitrary units is perfectly acceptable and circumvents the issue presented by Lyman-β emission. The proportionality relation is therefore given below for an intensity, $L(r)$, the cross-section for the interaction evaluated at the truncation energy, σ_α, and the densities for electrons and neutrals given by$n_e(r)$ and $n_n(r)$ respectively.

$$L(r) \propto \sigma_\alpha n_e(r) n_n(r). \tag{6.3}$$

If arbitrary units are to be used along the intensity axis it is acceptable to equate each side of this expression. Looking at figure 6.14 it is clear that the peak of the emission occurs close to r_c and then decays towards 0 at r_p. It is important to note, however, that this is a purely 1D model and that in observations neutral material will exist above the

pellet, shielding the pellet along the line of sight perpendicular to the magnetic axis. This explains the weaker emission seen coincident with the pellet that is not reproduced in these simulations. Looking at the classifications of cloud in Cseh et al. (2017) there is no obvious comparison to be made. To be clear, none of the profiles confidently match any of the shapes presented in Cseh et al. (2017). However, a sharp peak is recovered in the profiles that consider the charging of the cloud but the peak is far too close to r_c. Supposing the cloud had a softer edge at r_c it may be possible to reproduce these emission profiles more accurately. Some mechanisms that would soften this feature would include unbounded diffusion which would allow r_c to spread farther out and rarify the gas or substantial ionisation at r_c from the background plasma which would sufficiently decrease the neutral density at r_c and decrease the likelihood of dissociative excitation.

6.3.8 Consequences for striations

The continued decrease in ablation from the more inclusive models as illustrated in figures 6.11 and 6.13 implies that the ablation rate will eventually tend to zero unless the system is somehow disrupted. If the striations are assumed to be caused by material emitting in Hα and departing from the pellet to expose it to the plasma then some kind of transport or loss mechanism is absent from this model. The cloud appears to be aligned with the magnetic field so it could be that enough charge has entered the cloud and enough H_2^- has formed and adhered to the magnetic field at their point of creation such that shielding of the pellet is vastly weaker and ablation commences with greater effect. This would then create a new and predominantly neutral cloud and the cycle would repeat. This rather simple proposal also ignores the differential spread of the cloud under minimal ablation that would be expected from the $\dot{r}$ calculations in section 5.1.8. This would further distort the r^{-2} neutral profile and redistribute the charge accordingly even though it should be expected that the amount of ablation would remain the same because the amount of matter along the length is the same. There is also the possiblity that the intense electric fields and potentials in the cloud would encourage the cloud to rarify further to minimise the potential difference in the cloud. It is important to note that these are continuous changes and the striations are discretely occuring (see Wurden et al. (1990)). It could therefore be supposed that the striations occur because of a breach of some limit. This supports the argument that extensive charge capture in the cloud could force the cloud to separate from the pellet and begin an enhanced period of ablation.

6.4 Conclusion

This chapter is the culmination of all the work building towards a simple solution to the pellet ablation problem. Four models were constructed of increasing complexity and a more accurate representation of the pellet-cloud system in an effort to determine the ablation rate. The results indicate that the Fully Neutral model most accurately captures the ablation rate that is observed in tokamaks implying that the consideration of charge creates prohibitively large potentials and effectively causes ablation to cease. Even with the generation of ions through electron ionisation processes and their subsequent accelleration through a sheath the ablation is not elevated to the observed values. The conclusion to be drawn here is one which suggests that further mechanisms should be incorporated into more complicated models as it is entirely incorrect to neglect charge deposition and the potential field it creates. Some such mechanisms include ablation due to ultraviolet photons released via a Lyman series emission or the consideration of the physical size of ions compared to electrons. Furthermore the possibility of electrons and ions recombining whilst undergoing accelleration in the sheath would create even larger structures to impact the pellet. The ballistics and molecular dynamics at work here may further close the gap on ablation that the Diffusive Ion model calculates.

Chapter 7

Conclusions

The ablation of cryogenic pellets is posed to be a significant process to achieving stable fusion and this thesis aims to address some of the remaining challenges. The quantity that determines the rate at which a plasma is refuelled, the ablation rate, is ultimately essential to maintaing a fusion burn without compromising the stability of a machine. Attempts were made prior to this thesis by way of Parks and Turnbull (1977) which has been widely accepted by the community but a simpler approach may be possible. This is the key aim of the thesis - can a simple "toy-model" effectively describe the ablation process of a pellet in fusion reactor? This was answered by comparing the ablation process to evaporation through the "D^2" model to describe the structure of the cloud during the pellet's lifetime and the energy loss of electrons as they traverse the cloud. This loss of energy is captured by the continuous slowing down approximation (CSDA) calculation and their stopped position and terminal energy at the cloud is recorded for stopped and traversed particles respectively. The density of the stopped particles is known by dividing the initial electron distribution into bins and then applying the successive-over-relaxation method to Poisson's equation to calculate the potential field from the stopped charge. This can then be added to a sheath solution to determine the cumulative effect of both. Once the energy flux at the pellet surface is determined, the instantaneous ablation rate can be calculated and thus the evolution of the pellet-cloud system understood. The diffusion of any produced ions was performed and their contribution to ablation carried out to supplement the dominant electron ablation. The cycle was then repeated for many iterations to determine the cummulative effect.

The evaporative model that was applied found that it could approximately meet the

observations of the cloud in various machines. Temporal dependance is hard to confidently determine agreement on but the approximate length scales and densities can be routinely recovered from the evaporative model. Densities of 10^{25} - $10^{23}\mathrm{m}^{-3}$ are typically observed in tokamaks and recovered from the model with notable spatial variation within the model. Additionally, the size of the cloud is reported as a few cm in many instances with the cloud in the evaporative model evolving up to $\sim 35r_0$ when the pellet is essentially fully ablated. This model assumes totally symmetric and spherical expansion with integral accounting of the magnetic funnelling that has been observed. However, for a 1mm pellet, this approximately matches the observations - depending on the time of observation and extent of magnetic elongation. The combination of the size of the pellet and the cloud and its temporal evolution with an assumption on the form of the density profile is shown in figure 4.6. The form for the density profile is taken to be approximately r^{-2} which is in line with the slowest decay asserted by Parks and Turnbull (1977).

The use of CSDA was argued in chapter 3 and the exact application explained in chapter 5. This method accounted for all the possible excitations and interactions at each energy with the cross-sections captured in the various terms captured in the stopping function, B. The CSDA is dependent on the particle energy and the target density for a given projectile which means that for any given density distribution, lower energy particles should stop first. The initial energy distribution of electrons is Maxwellian in nature and therefore, when divided into bins, the density profile should reflect the initial energy distribution. This is found for many configurations of the pellet and the cloud and represented in figure 5.5. As expected, a smaller pellet corresponds to a larger cloud with more mass and therefore requires more energy to traverse it and this is observed with the minimum traversal energy, ϑ, continually increasing over time. A potential field of known structure was applied to the cloud at a given time and the parameters defining the field were changed such as the depth of the potential and the width and position of the centre of any peaked fields. Variation of these parameters presented differing extremes of influence. Particularly for the case of a highly peaked potential it is found that the energy is lost abruptly and then returned to the particle meaning that the additional energy loss from CSDA only takes place over a tightly confined space. If the centre of a peaked profile is closer to the pellet, where the density is greatest, the additional losses due to CSDA are more severe than if the centre was closer to the plasma. Unsurprisingly, for a linear potential across the cloud from ϕ_CV to 0V where the magnitude of ϕ_C increases the amount of material stopped increases. Put another way, a particle of a given energy traverses a greater distance for a smaller $|\phi_C|$. All of these parameters not only affect the impacting energy of any particles but also the

resultant density profile of deposited electrons. The results for these experiments can be found in section 5.2

The culmination of these effects was explored in chapter 6 by considering temporal evolution in self-consistent way. The competition between various effects was accounted for by building up the simulations by considering a charge-neutral cloud, a cloud with the self-consistent electron potential, the consideration of a plasma sheath (which was described in section 1.3) was included by adding a sheath potential to the self-consistent field and finally all of these are included with ions. These ions have not travelled across the cloud but were produced via electron-neutrals collisions at their stopping point and moving by diffusion and gaining energy by falling through the sheath by a single mean-free path.

The ultimate conclusion to draw from the outputs of chapter 6 is that the model does not appear to work. The word "appear" is used carefully here for reasons that will be explained later. The more layers of complexity and realism added to the model the farther it strays from the observed results in terms of pellet lifetime and ablation rate. The ablation rate in all models was determined to be lower than the observations and the pellet lifetime projected to be much longer, by many orders of magnitude in the models with a charged cloud, than the observations show. This has been attributed to the prohibitively large potentials in the cloud during the simulation which were calculated using a successive-over-relaxation (SOR) method on Poisson's equation. This means that if the model is indeed incorrectly implemented here that the issue for this can only be due to a poor SOR method or an incorrect determination of the density. Given that the SOR was verified on analytical test cases it must be the density that is the source of these erroneous ablation rates. There must then be loss mechanisms for the charge that have not been considered here or some method of redistributing the material in the cloud in such a fashion that mitigates the influence of the charge. Diffusion out of the cloud and back into the plasma of the H_2^- ions is one option but there is also the effect of the magnetic elongation of the cloud which may rarify it.

The reproduction of Hα emission yields more realistic results. Images from Cseh et al. (2017) show a variety of cloud shapes that have been categorised. Ignoring the categorisation and any justifcation as to how those individual shapes were created, many of them have a single peak along one half of the cloud. Although it can not be confirmed from their results whether that peak is co-spatial with a peak in the electron density it does. Excluding the hard edges observed in the profiles produced in this thesis, the emission profiles loosely match some of those observed in the study by Cseh et al. (2017). A diffusive edge on the cloud may account for some smoothing at r_c but the emission does seem quite low closer to

r_p. This may be a consequence of the late starting time of the simulation which was chosen such that $r_c - r_p = s$ where s is the length of the sheath. The simulation has therefore not accounted for any ablation and charge depositiont hat would have occured when the cloud was smaller and shielding therefore was weaker. Ablation would have been greater and the amount of charge density within the cloud would have been lower and, consequently, the potential would be weaker. It is possible that starting the simulation at earlier points in the system's evolution would have produced a very different outlook on the growth of the system.

The possibilities for exploring striations within the confines of this model are also proposed. Testing this experimentally would demand some kind of loss mechanism for neutral and charged particles in the cloud. It has been suggested that the H_2^- particles could now be gyrating about the magnetic field lines and expose the pellet to strengthened ablation for a short period. The material that remains along a field line would then continue to produce Hα emission and produce the striations until it is fully dissociated and ionised and thermally equilibrates with the background plasma. The pellet would then continue along its trajectory and undergo periods of stronger and weaker ablation until it is fully ablated. This proposed mechanism, albeit rudimentary, would allow for an exploration of striation formation and would potentially reproduce more acceptable projected lifetimes and ablation rates for the pellet. The method used in this thesis would need to be adapted to account for clouds smaller than a sheath length which may prove to be crucial in studying striation formation.

At the onset, this thesis was endeavouring to simplify the ablation problem. This thesis has reinforced the idea that it is indeed a complicated problem and the evaporative-CSDA model is not comprehensive in understanding pellet ablation. The system was only one-dimensional and inherently absent of higher dimensional phenomena such as certain instabilities and the effect of a directed magnetic field is similarly avoided. A broader hydrodynamic treatment is ignored in this thesis but establishes the quantities necessary to explore such a problem - cloud and charge densities, pellet and cloud sizes and energy deposition per unit length are all known. However, a precise treatment of the energy loss per unit length is lost in the generalised form of CSDA. A more thorough exploration of this side of the problem would demand an extensive library of cross-sections for the major (but ideally all) possible collisions between electrons and neutrals. This would also allow for a rigorous understanding of the ratios of particle populations in various states throughout the cloud and a reliable measure of the Hα emission as a diagnostic.

Ultimately, any "toy-model" will compromise on certain details to preserve the simplicity

that is desired. These details are to be captured in further studies either by means of maintaining the simplicity and exploring the breadth of problems available or by aiming to justify the simpler model with more fundamental physics and developing the complexity. This thesis is a springboard for those studies but also meets observations in tokamaks substantiating the efficacy of applying a modified evaporative model. Hydrodynamic studies, more irigorous particle treatments or investigations into the importance of additional phenomena are all possible based on the foundational work presented here.

Bibliography

Adey, D., An, F. P., Balantekin, A. B., Band, H. R., Bishai, M., Blyth, S., Cao, D., Cao, G. F., Cao, J., Chang, J. F., Chang, Y., Chen, H. S., Chen, S. M., Chen, Y., Chen, Y. X., Cheng, J., Cheng, Z. K., Cherwinka, J. J., Chu, M. C., Chukanov, A., Cummings, J. P., Dash, N., Deng, F. S., Ding, Y. Y., Diwan, M. V., Dohnal, T., Dove, J., Dvořák, M., Dwyer, D. A., Gonchar, M., Gong, G. H., Gong, H., Gu, W. Q., Guo, J. Y., Guo, L., Guo, X. H., Guo, Y. H., Guo, Z., Hackenburg, R. W., Hans, S., He, M., Heeger, K. M., Heng, Y. K., Higuera, A., Hor, Y. K., Hsiung, Y. B., Hu, B. Z., Hu, J. R., Hu, T., Hu, Z. J., Huang, H. X., Huang, X. T., Huang, Y. B., Huber, P., Jaffe, D. E., Jen, K. L., Jetter, S., Ji, X. L., Ji, X. P., Johnson, R. A., Jones, D., Kang, L., Kettell, S. H., Koerner, L. W., Kohn, S., Kramer, M., Langford, T. J., Lebanowski, L., Lee, J., Lee, J. H., Lei, R. T., Leitner, R., Leung, J. K., Li, C., Li, F., Li, H. L., Li, Q. J., Li, S., Li, S. C., Li, S. J., Li, W. D., Li, X. N., Li, X. Q., Li, Y. F., Li, Z. B., Liang, H., Lin, C. J., Lin, G. L., Lin, S., Lin, S. K., Ling, J. J., Link, J. M., Littenberg, L., Littlejohn, B. R., Liu, J. C., Liu, J. L., Liu, Y., Liu, Y. H., Lu, C., Lu, H. Q., Lu, J. S., Luk, K. B., Ma, X. B., Ma, X. Y., Ma, Y. Q., Marshall, C., Caicedo, D. A., McDonald, K. T., McKeown, R. D., Mitchell, I., Lepin, L. M., Napolitano, J., Naumov, D., Naumova, E., Ochoa-Ricoux, J. P., Olshevskiy, A., Pan, H. R., Park, J., Patton, S., Pec, V., Peng, J. C., Pinsky, L., Pun, C. S., Qi, F. Z., Qi, M., Qian, X., Raper, N., Ren, J., Rosero, R., Roskovec, B., Ruan, X. C., Steiner, H., Sun, J. L., Treskov, K., Tse, W. H., Tull, C. E., Viren, B., Vorobel, V., Wang, C. H., Wang, J., Wang, M., Wang, N. Y., Wang, R. G., Wang, W., Wang, X., Wang, Y., Wang, Y. F., Wang, Z., Wang, Z. M., Wei, H. Y., Wei, L. H., Wen, L. J., Whisnant, K., White, C. G., Wong, H. L., Wong, S. C., Worcester, E., Wu, Q., Wu, W. J., Xia, D. M., Xing, Z. Z., Xu, J. L., Xue, T., Yang, C. G., Yang, L., Yang, M. S., Yang, Y. Z., Ye, M., Yeh, M., Young, B. L., Yu, H. Z., Yu, Z. Y., Yue, B. B., Zeng, S., Zeng, Y., Zhan, L., Zhang, C., Zhang, C. C., Zhang, F. Y., Zhang, H. H., Zhang, J. W., Zhang, Q. M., Zhang, R., Zhang, X. F., Zhang, X. T., Zhang,

Y. M., Zhang, Y. X., Zhang, Y. Y., Zhang, Z. J., Zhang, Z. P., Zhang, Z. Y., Zhao, J., Zhou, L., Zhuang, H. L., and Zou, J. H. (2019). A high precision calibration of the nonlinear energy response at Daya Bay. *Nuclear Instruments and Methods in Physics Research, Section A: Accelerators, Spectrometers, Detectors and Associated Equipment*, 940(June):230–242.

Aguilar, G., Majaron, B., Verkruysse, W., Zhou, Y., Nelson, J. S., and Lavernia, E. J. (2001). Theoretical and experimental analysis of droplet diameter, temperature, and avaporation rate evolution in cryogenic sprays. *International Journal of Heat and Mass Transfer*, 44(17):3201–3211.

Baldzuhn, J., Damm, H., Beidler, C. D., Mccarthy, K., and Panadero, N. (2019). Pellet fueling experiments in Wendelstein 7-X. *Plasma Physics and Controlled Fusion*, 61.

Baylor, L. R., Combs, S. K., Lyttle, M. S., Meitner, S. J., and Rasmussen, D. A. (2016). Pellet Injection Technology and its Application on ITER. 44(9):1–6.

Baylor, L. R., Schmidt, G. L., Houlberg, W. A., Milora, S. L., Gowers, C. W., Bailey, W. P., Gadeberg, M., Kupschus, P., Tagle, J. A., Owens, D. K., Mansfield, D. K., and Park, H. K. (1992). Pellet fuelling deposition measurements on Jet and TFTR. *Nuclear Fusion*, 32(12):2177–2187.

Behringer, K. H. and Büchl, K. (1989). Impurity transport studies in ASDEX by means of neon-seeded pellets. *Nuclear Fusion*, 29(3):415–422.

Berger, M. B., Coursey, J. S., and Zucker, M. A. (1999). ESTAR, PSTAR, and ASTAR: Computer Programs for Calculating Stopping-Power and Range Tables for Electrons, Protons, and Helium Ions (version 1.21). Technical report, NIST.

Biagi. www.lxcat.net.

Boyd, T. and Sanderson, J. (2003). *The Physics of Plasmas*. Cambridge University Press, 1st edition.

Cazabat, A. M. and Guéna, G. (2010). Evaporation of macroscopic sessile droplets. *Soft Matter*, 6(12):2591–2612.

Cesar, D. B., Musumeci, P., and Alesini, D. (2015). Ultrafast gating of a mid-infrared laser pulse by a sub-pC relativistic electron beam. *Journal of Applied Physics*, 118(23).

Combs, S. K. (1993). Pellet injection. *Review of Scientific Instruments*, 64:1679 – 1698.

Combs, S. K., Baylor, L. R., Meitner, S. J., Caughman, J. B. O., Rasmussen, D. A., and Maruyama, S. (2012). Overview of recent developments in pellet injection for ITER. *Fusion Engineering and Design*, 87(5-6):634–640.

Commaux, N., Baylor, L. R., Jernigan, T. C., Hollmann, E. M., Parks, P. B., Humphreys, D. A., Wesley, J. C., and Yu, J. H. (2010). Demonstration of rapid shutdown using large shattered deuterium pellet injection in DIII-D. *Nuclear Fusion*, 50(11).

Cseh, G., Kocsis, G., Lang, P. T., Plöckl, B., Szepesi, T., and Veres, G. (2017). Pellet cloud characterisation, scaling and estimation of the material- and temperature distribution inside the cloud. *Nuclear Fusion*, 57(1).

Deutsch, C. (2019). Correlated ion stopping in dense plasmas. *Matter and Radiation at Extremes*, 4(3).

Dunne, M., Kocsis, G., Suttrop, W., Wolfrum, E., Garzotti, L., Fischer, L., Kirk, A., Cseh, G., Szepesi, T., Lang, P., Scannell, R., Plőckl, B., Cavedon, M., Thornton, A., Guimarais, L., Viezzer, E., Tardini, G., Valovič, M., and Mlynek, A. (2016). Pellet refuelling of particle loss due to ELM mitigation with RMPs in the ASDEX Upgrade tokamak at low collisionality. *Nuclear Fusion*, 56(6):066009.

Evans, T. E., Fenstermacher, M. E., Moyer, R. A., Osborne, T. H., Watkins, J. G., Gohil, P., Joseph, I., Schaffer, M. J., Baylor, L. R., Bécoulet, M., Boedo, J. A., Burrell, K. H., Degrassie, J. S., Finken, K. H., Jernigan, T., Jakubowski, M. W., Lasnier, C. J., Lehnen, M., Leonard, A. W., Lonnroth, J., Nardon, E., Parail, V., Schmitz, O., Unterberg, B., and West, W. P. (2008). RMP ELM suppression in DIII-D plasmas with ITER similar shapes and collisionalities. *Nuclear Fusion*, 48(2).

Foster, C. A., Colchin, R. J., Milora, S. L., Kim, K., and Turnbull, R. J. (1977). Solid hydrogen pellet injection into the ormak tokamak. *Nuclear Fusion*, 17(5):1067–1075.

Gál, K., Belonohy, É., Kocsis, G., Lang, P. T., and Veres, G. (2008). Role of shielding in modelling cryogenic deuterium pellet ablation. *Nuclear Fusion*, 48(8).

Garzotti, L., Baylor, L., Ochl, F. K., Pégourié, B., Valovič, M., Axon, K. B., Dowling, J., Gurl, C., Maddison, G. P., Nehme, H., O'Gorman, T., Patel, A., Price, M., Scannell, R.,

and Walsh, M. (2010). Observation and analysis of pellet material δb drift on MAST. *Nuclear Fusion*, 50(10).

Garzotti, L., Belo, P., Corrigan, G., Köchl, F., Lönnroth, J., Parail, V., Pereverzev, G., Saarelma, S., Tardini, G., Valovič, M., Voitsekhovitch, I., and Wiesen, S. (2012). Simulations of density profiles, pellet fuelling and density control in ITER. *Nuclear Fusion*, 52(1).

Garzotti, L., Pégourié, B., Géraud, A., Frigione, D., and Baylor, L. R. (1997). Neutral gas and plasma shielding scaling law for pellet ablation in maxwellian plasmas. *Nuclear Fusion*, 37(8):1167–1175.

Geraud, A., Dentan, M., Whitehead, A., Butcher, P., Communal, D., Faisse, F., Gedney, J., Gros, G., Guillaume, D., Hackett, L., Hennion, V., Homfray, D., Lucock, R., McKivitt, J., Sibbald, M., Portafaix, C., Perin, J. P., Reade, M., Sands, D., Saille, A., Symonds, I., M.Watson, Worth, L., and Vinyar, I. (2007). The JET high frequency pellet injector project. *Fusion Engineering and Design*, 82(15-24):2183–2188.

Godyak, V. A. and Sternberg, N. (1990). Smooth Plasma-Sheath Transition in a Hydrodynamic Model. *IEEE Transactions on Plasma Science*, 18(1):159–168.

Gouge, M. J., St. Onge, K. D., Milora, S. L., Fisher, P. W., and Combs, S. K. (1992). Pellet fueling system for ITER. *Fusion Engineering and Design*, 19(1):53–72.

Greenwald, M. (2002). Density limits in toroidal plasmas. *Plasma Physics and Controlled Fusion*, 44(8).

Greenwald, M., Gwinn, D., Milora, S., Parker, J., Parker, R., Wolfe, S., Besen, M., Camacho, F., Fairfax, S., Fiore, C., Foord, M., Gandy, R., Gomez, C., Granetz, R., Labombard, B., Lipschultz, B., Lloyd, B., Marmar, E., McCool, S., Pappas, D., Petrasso, R., Pribyl, P., Rice, J., Schuresko, D., Takase, Y., Terry, J., and Watterson, R. (1984). Energy confinement of high-density pellet-fueled plasmas in the alcator C tokamak. *Physical Review Letters*, 53(4):352–355.

Grimes, D. R., Warren, D. R., and Partridge, M. (2017). An approximate analytical solution of the Bethe equation for charged particles in the radiotherapeutic energy range. *Scientific Reports*, 7(1):1–12.

Gümü, H. and Kabadayi, Ö. (2010). Practical calculations of stopping powers for intermediate energy electrons in some elemental solids. *Vacuum*, 85(2):245–252.

Gurnett, D. A. and Bhattacharjee, A. (2005). *Introduction to Plasma Physics with Space and Laboratory Applications*. Cambridge University Press, 1st edition.

Han, D., Siebers, J. V., and Williamson, J. F. (2016). A linear, separable two-parameter model for dual energy CT imaging of proton stopping power computation. *Medical Physics*, 43(1):600–612.

Harvey, R. W., Chan, V. S., Chiu, S. C., Evans, T. E., Rosenbluth, M. N., and Whyte, D. G. (2000). Runaway electron production in DIII-D killer pellet experiments, calculated with the CQL3D/KPRAD model. *Physics of Plasmas*, 7(11):4590–4599.

Houlberg, W. A. and Attenberger, S. E. (1988). Neutral and plasma shielding model for pellet ablation. *Nuclear Fusion*, 28(4):595–610.

Igitkhanov, Y., Bazylev, B., and Landman, I. (2011). Calculation of runaway electrons stopping power in ITER. *Journal of Nuclear Materials*, 415(1 SUPPL):S845–S848.

IST-Lisbon. www.lxcat.net.

Kazkaz, K., Foxe, M., Bernstein, A., Hagmann, C., Jovanovic, I., Sorensen, P., Stoeffl, W. S., and Winant, C. D. (2010). Operation of a 1-liter-volume gaseous argon proportional scintillation counter. *Nuclear Instruments and Methods in Physics Research, Section A: Accelerators, Spectrometers, Detectors and Associated Equipment*, 621(1-3):267–277.

Keilhacker, M., Gibson, A., Gormezano, C., Lomas, P. J., Thomas, P. R., Watkins, M. L., Andrew, P., Balet, B., Borba, D., Challis, C. D., Coffey, I., Cottrell, G. A., De Esch, H. P., Deliyanakis, N., Fasoli, A., Gowers, C. W., Guo, H. Y., Huysmans, G. T., Jones, T. T., Kerner, W., König, R. W., Loughlin, M. J., Maas, A., Marcus, F. B., Nave, M. F., Rimini, F. G., Sadler, G. J., Sharapov, S. E., Sips, G., Smeulders, P., Söldner, F. X., Taroni, A., Tubbing, B. J., Von Hellermann, M. G., and Ward, D. J. (1999). High fusion performance from deuterium-tritium plasmas in JET. *Nuclear Fusion*, 39(2):209–234.

Krasheninnikov, S. I., Smirnov, R. D., and Rudakov, D. L. (2011). Dust in magnetic fusion devices. *Plasma Physics and Controlled Fusion*, 53(8).

Kumar, E. R., Danani, C., Sandeep, I., Chakrapani, C., Pragash, N. R., Chaudhari, V., Rotti, C., Raole, P. M., Alphonsa, J., and Deshpande, S. P. (2008). Preliminary design

of Indian Test Blanket Module for ITER. *Fusion Engineering and Design*, 83(7-9):1169–1172.

Lang, P. T., Conway, G. D., Eich, T., Fattorini, L., Gruber, O., Günter, S., Horton, L. D., Kalvin, S., Kallenbach, A., Kaufmann, M., Kocsis, G., Lorenz, A., Manso, M. E., Maraschek, M., Mertens, V., Neuhauser, J., Nunes, I., Schneider, W., Suttrop, W., and Urano, H. (2004). ELM pace making and mitigation by pellet injection in ASDEX upgrade. *Nuclear Fusion*, 44(5):665–677.

Lengyel, L. L., Büchl, K., Pautasso, G., Ledl, L., Ushakov, A. A., Kalvin, S., and Veres, G. (1999). Modelling of impurity pellet ablation in ASDEX Upgrade (neon) and Wendelstein W7-AS (carbon) by means of a radiative ('killer') pellet code. *Nuclear Fusion*, 39(6):791–812.

Lengyel, L. L. and Spathis, P. N. (1994). A self-consistent MHD ablation model: Pellet penetration depth prediction for a reactor-temperature plasma. *Nuclear Fusion*, 34(5):675–685.

Lengyel, L. L., Zavala, G. G., Kardaun, O. J., and Lalousis, P. (1991). Evolution of pellet clouds and cloud structures in magnetically confined plasmas. *Nuclear Fusion*, 31(6):1107–1121.

Lieberman, M. A. and Lichtenberg, A. J. (2005). *Principles of Plasma Discharges and Materials Processing*. Wiley, 2nd edition.

Livadiotis, G., Desai, M. I., and Wilson, L. B. (2018). Generation of Kappa Distributions in Solar Wind at 1 au. *The Astrophysical Journal*, 853(2):142.

Lloyd, B., Akers, R., Alladio, F., Andrew, Y., Appel, L., and Applegate, D. (2007). Overview of results from MAST. *Nuclear Fusion*, (47):658 – 667.

Loarte, A., Huijsmans, G., Futatani, S., Baylor, L. R., Evans, T. E., Orlov, D. M., Schmitz, O., Becoulet, M., Cahyna, P., Gribov, Y., Kavin, A., Sashala Naik, A., Campbell, D. J., Casper, T., Daly, E., Frerichs, H., Kischner, A., Laengner, R., Lisgo, S., Pitts, R. A., Saibene, G., and Wingen, A. (2014). Progress on the application of ELM control schemes to ITER scenarios from the non-active phase to DT operation. *Nuclear Fusion*, 54(3).

Lorenzini, R., Garzotti, L., Pégourié, B., Innocente, P., and Martini, S. (2002). Analysis and modelling of plasma response to pellet injection in RFX. *Plasma Physics and Controlled Fusion*, 44(2):233–252.

Martin, B. (2009). *Nuclear and Particle Physics: An Introduction*. John Wiley & Sons, 2nd edition.

Matsuyama, A., Pégourié, B., Sakamoto, R., Mishra, J. S., Motojima, G., and Yamada, H. (2012). Over-ablation and deflection of hydrogen pellets injected into neutral beam injection heated plasmas in the Large Helical Device. *Plasma Physics and Controlled Fusion*, 54(3).

Milora, S. L. and Foster, C. A. (1978). A revised neutral gas shielding model for pellet-plasma interactions. *IEEE Transactions on Plasma Science*, 6(4):578–592.

Milora, S. L., Houlberg, W. A., Lengyel, L. L., and Mertens, V. (1995). Pellet fuelling. *Nuclear Fusion*, 35(6):657–754.

Morozov, D. K., Gervids, V. I., Senichenkov, I. Y., Veselova, I. Y., Rozhansky, V. A., and Schneider, R. (2004). Ionization-recombination processes and ablation cloud structure for a carbon pellet. *Nuclear Fusion*, 44(2):252–259.

Morse, E. (2019). *Nuclear Fusion*, volume 3.

Müller, H. W., Dux, R., Kaufmann, M., Lang, P. T., Lorenz, A., Maraschek, M., Mertens, V., Neuhauser, J., and ASDEX Upgrade Team (2002). High β plasmoid formation , drift and striations during pellet ablation in. *Nuclear Fusion*, 42(3).

Nguyen-Truong, H. T. (2015). Modified Bethe formula for low-energy electron stopping power without fitting parameters. *Ultramicroscopy*, 149:26–33.

Panadero, N., McCarthy, K. J., Koechl, F., Baldzuhn, J., Velasco, J. L., Combs, S. K., De La Cal, E., García, R., Hernández Sánchez, J., Silvagni, D., and Turkin, Y. (2018). Experimental studies and simulations of hydrogen pellet ablation in the stellarator TJ-II. *Nuclear Fusion*, 58(2).

Parks, P. B. (1992). Electric field and current distribution near the ablation cloud of a pellet injected into a tokamak. *Nuclear Fusion*, 32(12):2137–2145.

Parks, P. B. and Turnbull, R. J. (1977). A model for the ablation rate of a solid hydrogen pellet in a plasma. *Nuclear Fusion*, 17(3):539–556.

Parks, P. B. and Turnbull, R. J. (1978). Effect of transonic flow in the ablation cloud on the lifetime of a solid hydrogen pellet in a plasma. *Physics of Fluids*, 21(10):1735–1741.

Pégourié, B. (2007). Review: Pellet injection experiments and modelling. *Plasma Physics and Controlled Fusion*, 49(8).

Pégourié, B., Waller, V., Dumont, R. J., Eriksson, L. G., Garzotti, L., Géraud, A., and Imbeaux, F. (2005). Modelling of pellet ablation in additionally heated plasmas. *Plasma Physics and Controlled Fusion*, 47(1):17–35.

Phelps. www.lxcat.net.

Qi, Y., Shojaee, S. A., Harriman, T. A., Wang, Y. Q., Mehner, A., and Lucca, D. A. (2019). Effects of nuclear and electronic stopping powers on the conversion of hybrid silicate thin films. *Nuclear Instruments and Methods in Physics Research, Section B: Beam Interactions with Materials and Atoms*, 444(February):103–106.

Rebut, P. H., Bickerton, R. J., and Keen Jet, B. E. (1985). Magnetic confinement 1. Tokamaks the joint european torus: Installation, first results and prospects. *Nuclear Fusion*, 25(9):1011.

Riemann, K. U. (1991). The Bohm criterion and sheath formation 1,. *Journal of Physics D: Applied Physics*, 24:493–518.

Rozhansky, V., Senichenkov, I., Veselova, I., and Schneider, R. (2004). Mass deposition after pellet injection into a tokamak. *Plasma Physics and Controlled Fusion*, 46(4):575–591.

Rozhansky, V., Veselova, I., and Voskoboynikov, S. (1995). Evolution and stratification of a plasma cloud surrounding a pellet. *Plasma Physics and Controlled Fusion*, 37(4):399–414.

Samulyak, R., Lu, T., and Parks, P. (2007). A magnetohydrodynamic simulation of pellet ablation in the electrostatic approximation. *Nuclear Fusion*, 47(2):103–118.

Seltzer, S. M. and Berger, M. J. (1982). Evaluation of the collision stopping power of elements and compounds for electrons and positrons. *The International Journal of Applied Radiation and Isotopes*, 33(11):1189–1218.

Seltzer, S. M. and Berger, M. J. (1984). Improved procedure for calculating the collision stopping power of elements and compounds for electrons and positrons. *The International Journal Of Applied Radiation And Isotopes*, 35(7):665–676.

Senichenkov, I. Y., Veselova, I. Y., Rozhansky, V. A., and Schneider, R. (2006). Modelling of the pellet cloud evolution and mass deposition with an account of grad-b induced drift. *Nuclear Fusion*, 46(8):788–796.

Sigmund, P. (2006). *Particle Penetration and Radiation Effects - General Aspects and Stopping of Swift Point Charges*. Springer-Verlag Berlin Heidelberg.

Skovorodin, D. I., Pshenov, A. A., Arakcheev, A. S., Eksaeva, E. A., Marenkov, E. D., and Krasheninnikov, S. I. (2016). Vapor shielding models and the energy absorbed by divertor targets during transient events. *Physics of Plasmas*, 23(2).

Sonato, P., Agostinetti, P., Anaclerio, G., Antoni, V., Barana, O., Bigi, M., Boldrin, M., Cavenago, M., Dal Bello, S., Palma, M. D., Daniele, A., D'Arienzo, M., De Lorenzi, A., Ferro, A., Fiorentin, A., Gaio, E., Gazza, E., Grando, L., Fantini, F., Fellin, F., Luchetta, A., Manduchi, G., Milani, F., Marcuzzi, D., Novello, L., Pasqualotto, R., Pavei, M., Pengo, R., Peruzzo, S., Pesce, A., Pilan, N., Piovan, R., Pomaro, N., Recchia, M., Rigato, W., Rizzolo, A., Serianni, G., Spolaore, M., Spolaore, P., Sandri, S., Taliercio, C., Toigo, V., Valisa, M., Veltri, P., Zaccaria, P., Zamengo, A., and Zanotto, L. (2009). The ITER full size plasma source device design. *Fusion Engineering and Design*, 84(2-6):269–274.

Sternheimer, R. M. and Peierls, R. M. (1971). General Expression for the Density Effect for the Ionization Loss of Charged Particles. *Physical Review B*, 3(11).

Tolstikhina, I., Imai, M., Winckler, N., and Shevelko, V. (2018). *Basic Atomic Interactions of Accelerated Heavy Ions in Matter*. Publishing, Springer International.

Triniti. www.lxcat.net.

Tvalashvili, G., Garzotti, L., Sips, G., Maddaluno, G., Viola, B., Artaserse, G., Alper, B., Giovannozzi, E., Bennett, P., Kocsis, G., Mooney, R., Wilkes, D., Lennholm, M., Rack, M., Eich, T., Frigione, D., and Lang, P. (2015). Divertor load footprint of ELMs in pellet triggering and pacing experiments at JET. *Journal of Nuclear Materials*, 463:714–717.

Vincenzi, P., Koechl, F., Garzotti, L., King, D. B., Tindale, E., Bolzonella, T., Lang, P. T., Pégourié, B., Romanelli, M., and Wenninger, R. (2015). Fuelling and density control for DEMO. *Nuclear Fusion*, 55(11).

W.a. Houlberg, S.e. Attenberger, L.r. Baylor, M. Gadeberg, T.c. Jernigan, P. Kupschus, S.l. Milora, G.l. Schmidt, D.w. Swain, and M.l. Watkins (1992). Pellet penetration experiments on JET. *Nuclear Fusion*, 32(11):1951–1965.

Wagner, F., Becker, G., Behringer, K., Campbell, D., Eberhagen, A., Engelhardt, W., and Fussmann, G. (1982). Regime of Improved Confinement and High Beta in Neutral-

Beam-Heated Divertor DIscharges of the ASDEX Tokamak. *Physical Review Letters*, (NovEMBER):1408–1412.

Wohlfahrt, P., Möhler, C., Richter, C., and Greilich, S. (2018). Evaluation of Stopping-Power Prediction by Dual- and Single-Energy Computed Tomography in an Anthropomorphic Ground-Truth Phantom. *International Journal of Radiation Oncology Biology Physics*, 100(1):244–253.

Wurden, G. A., Büchl, K., Hofmann, J., Lang, R., Loch, R., Rudyj, A., and Sandmann, W. (1990). Pellet imaging techniques in the ASDEX tokamak. *Review of Scientific Instruments*, 61(11):3604–3608.

Yoshino, R., Kondoh, T., Neyatani, Y., Itami, K., Kawano, Y., and Isei, N. (1997). Fast plasma shutdown by killer pellet injection in JT-60U with reduced heat flux on the divertor plate and avoiding runaway electron generation. *Plasma Physics and Controlled Fusion*, 39(2):313–332.

Yu, J. H., Rudakov, D. L., Pigarov, A. Y., Smirnov, R. D., Brooks, N. H., Muller, S. H., and West, W. P. (2009). Fast camera imaging of dust in the DIII-D tokamak. *Journal of Nuclear Materials*, 390-391(1):216–219.

Yu, Y., Li, Q., Zhou, C. Q., Zhou, P., and Yan, H. J. (2017). Investigation of droplet evaporation on heterogeneous surfaces using a three-dimensional thermal multiphase lattice Boltzmann model. *Applied Thermal Engineering*, 127:1346–1354.

Zhakhovsky, V. V., Kryukov, A. P., Levashov, V. Y., Shishkova, I. N., and Anisimov, S. I. (2018). Mass and heat transfer between evaporation and condensation surfaces: Atomistic simulation and solution of Boltzmann kinetic equation. *Proceedings of the National Academy of Sciences*, 116(37):201714503.

Zieb, K., Hughes, H. G., James, M. R., and Xu, X. G. (2018). Review of heavy charged particle transport in MCNP6.2. *Nuclear Instruments and Methods in Physics Research, Section A: Accelerators, Spectrometers, Detectors and Associated Equipment*, 886(May 2017):77–87.